Space Radiation Effects in Conductive Bridging Random Access Memory

by

Jennifer Lynn Taggart

A Dissertation Presented in Partial Fulfillment
of the Requirements for the Degree
Doctor of Philosophy

Approved November 2018 by the
Graduate Supervisory Committee:

Hugh Barnaby, Chair
Michael Kozicki
Keith Holbert
Shimeng Yu

ARIZONA STATE UNIVERSITY

December 2018

ABSTRACT

This work investigates the effects of ionizing radiation and displacement damage on the retention of state, DC programming, and neuromorphic pulsed programming of Ag-$Ge_{30}Se_{70}$ conductive bridging random access memory (CBRAM) devices. The results show that CBRAM devices are susceptible to both environments. An observable degradation in electrical response due to total ionizing dose (TID) is shown during neuromorphic pulsed programming at TID below 1 Mrad using ^{60}Co. DC cycling in a 14 MeV neutron environment showed a collapse of the high resistance state (HRS) and low resistance state (LRS) programming window after a fluence of 4.9×10^{12} n/cm^2, demonstrating the CBRAM can fail in a displacement damage environment. Heavy ion exposure during retention testing and DC cycling, showed that failures to programming occurred at approximately the same threshold, indicating that the failure mechanism for the two types of tests may be the same. The dose received due to ionizing electronic interactions and non-ionizing kinetic interactions, was calculated for each ion species at the fluence of failure. TID values appear to be the most correlated, indicating that TID effects may be the dominate failure mechanism in a combined environment, though it is currently unclear as to how the displacement damage also contributes to the response. An analysis of material effects due to TID has indicated that radiation damage can limit the migration of Ag^+ ions. The reduction in ion current density can explain several of the effects observed in CBRAM while in the LRS.

Dedicated to my Husband Bill

ACKNOWLEDGEMENTS

I would like to thank my research advisor and committee members for taking the time and effort to evaluate this work. I would also like to acknowledge the scientists and staff at the Sandia National Laboratories Ion Beam Lab, for helping to operate, setup, and perform my heavy ion experiments. Michael McLain, Robin Jacobs-Gedrim and the staff at Sandia's Gamma Irradiation Facility also helped me to perform the high dose rate ^{60}Co exposures. Lastly, I'd like to acknowledge the staff at Cobham Rad Solutions in Colorado Springs, for helping me to perform 14 MeV neutron exposures.

TABLE OF CONTENTS

CHAPTER Page

LIST OF TABLES

LIST OF FIGURES

Figure Page

Figure Page

Figure Page

Figure Page

Figure Page

Figure Page

Chapter 1

INTRODUCTION

1.1 The Space Radiation Environment

Humans have long held a fascination with the night sky and its *Heavenly Bodies* though not until recently have we had the opportunity and means to launch into space to discover what is really out there. The first satellite, known as Sputnik, was launched by the Russians on October 4, 1957 [2]. The satellite orbited the Earth every 96.2 minutes and transmitted radio signals for three weeks until its battery failed. The success of Sputnik put pressure on the United States to step up their space program and on January 31, 1958, the U.S. launched Explorer I. Explorer I was equipped with a Geiger counter for the purpose of measuring cosmic rays [3],[4]. What scientists found instead were regions around the Earth with high fluxes of trapped energetic particles; an inner region of protons and an outer region of electrons [4]. These radiation regions of Earth's magnetosphere were named the Van Allen belts after James Van Allen who designed the radiation sensors and interpreted the data from the satellite. Following the discovery from Explorer I, subsequent Explorer and Pioneer missions included equipment for mapping the radiation environment surrounding Earth [4]. Venturing beyond Earth, the Pioneer V probe was placed in solar orbit between Earth and Venus in 1960, where it discovered the interplanetary magnetic field (IMF) generated by the Sun [5] and Pioneer X in 1973, was the first spacecraft to travels beyond the asteroid belt and measure Jupiter's intense magnetosphere [6]. These early space missions mapped and helped develop an understanding of the natural radiation environment that surrounds not only the Earth, but many of the planets in our solar system.

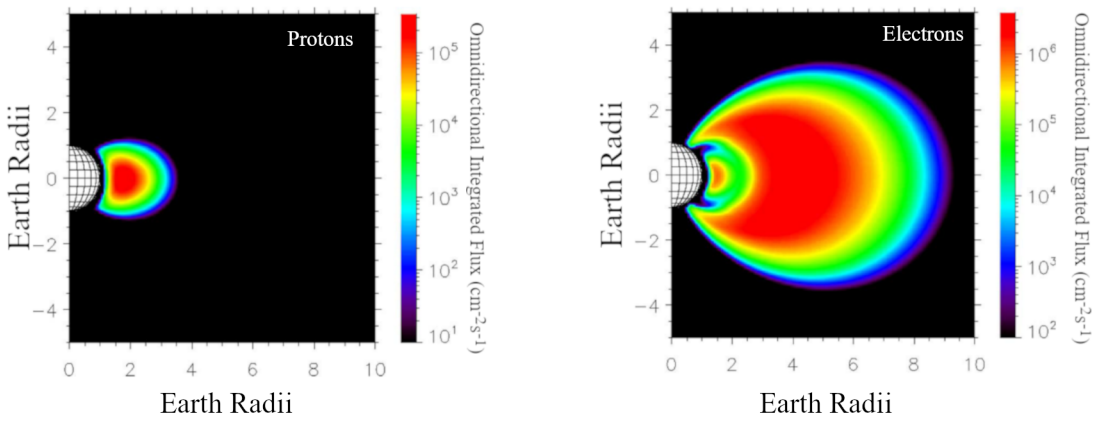

(a) (b)

Figure 1.1: Omni-directional flux of trapped (a) protons > 10 MeV and (b) electrons > 1 MeV versus distance from Earth [7].

Knowing the flux and energies of ionized particles at different distances from Earth has allowed engineers to design radiation hardened electronics that can survive within Earth's magnetosphere for years on end. Radiation hardening is a vital engineering consideration that has allowed for the success of long term NASA, military, and commercial space missions.

Many of our modern conveniences are made possible by communication satellites that orbit Earth and relay data down to our smartphones, GPS receivers, and satellite TV boxes. Inside these satellites are electronics that must survive high levels of ionizing radiation trapped in Earth's magnetosphere. Within the Van Allen Belts, the main particles of concern are high energy electrons and protons. The energy and location of the trapped charge are shown in Fig. 1.1. These charged particles can contribute to total ionizing dose (TID) effects, enhanced low dose rate sensitivity (ELDRS), and or single event effects (SEE). Heavier ions from coronal mass ejections (CME) that pass near Earth, can become trapped in the magnetosphere and cause displacement damage (DD) in electronics in addition to TID effects. Low energy

protons can also cause DD depending on its interaction cross section with the material it passes through. For the following work presented in this dissertation, only TID and DD effects are considered.

1.1.1 Total Ionizing Dose

When an energetic charged particle or high energy photon passes through a material it can cause a generation of carriers [8]. Charged particles will cause direct ionization, meaning the particle interacts directly with the orbital electrons of the atoms in the material through the Coulomb force. As a heavy ion passes through the material it will lose a fraction of its energy as it interacts with the surrounding electrons. This energy loss is known as linear energy transfer (LET). Once the ion loses enough energy, such that it is unable to excite the surrounding bound electrons, it will continue to lose energy through nuclear collisions, referred to as non-ionizing energy loss (NIEL) [9]. High energy electrons transfer their energy to the surrounding material in a similar manner as ions. High energy electrons can also be deflected by a charged particle in the material, resulting in the lose of kinetic energy and the generation Bremsstrahlung X-rays. The generated X-rays can be absorbed by bound electrons, resulting in the generation of additional free electrons.

High energy protons and electrons are not easy to produce on Earth and require expensive accelerators only available at a limited number of locations around the world. To test components on Earth, high energy photons sources such as X-ray generators and Cobalt-60 (γ-rays) are used. The natural space environment does not have a significant flux of high energy photons but photons can also cause ionization and are a good analog for TID testing. Photons cause indirect ionization by one of three mechanisms: photoelectric effect, Compton scattering, or pair production [10]. In indirect ionization, as opposed to direct, the photon must first excite a single

electron. The kinetic energy absorbed by that electron will allow it to move, causing additional direct ionizations.

The quantity of energy absorbed by a material through electronic interactions is known as ionizing dose. Over its lifetime in space, a material will experience many interactions with ionized particles for a cumulative dose typically referred to as total ionizing dose. The unit used for a dose of absorbed energy is the rad, which is the amount of energy absorbed per mass where 1 rad = 100 erg/g. Since different materials each have different mass and density, the rad is a unit that is specific to the material receiving the dose (i.e. rad(Si)).

1.1.2 Displacement Damage

In addition to ionizing effects, materials can experience displacement damage when a high energy ion passes through it [11]. An incident ion has a chance of colliding with the nucleus of an atom in the material causing the atom to recoil, often called a primary knock-on (PKO). If the energy transfered to the atom is high enough, it can become displaced from its lattice site creating a vacancy. The displaced atom and its vacancy site are known as a Frenkel pair [11]. Depending on the kinetic interaction of the collision, the incident ion can continue to travel through the material causing additional ionization and displacement damage. If the ion loses all of its energy in the collision, it can take the place of the displaced atom in the lattice, referred to as a replacement collision [11]. If the displaced atom has sufficient energy it can also cause a cascade of damage events through the material.

1.1.3 Onwards to Jupiter

Satellites in orbit around Earth exist in a high energy radiation environment. To prevent the performance of the electronic components from degrading, the hardware

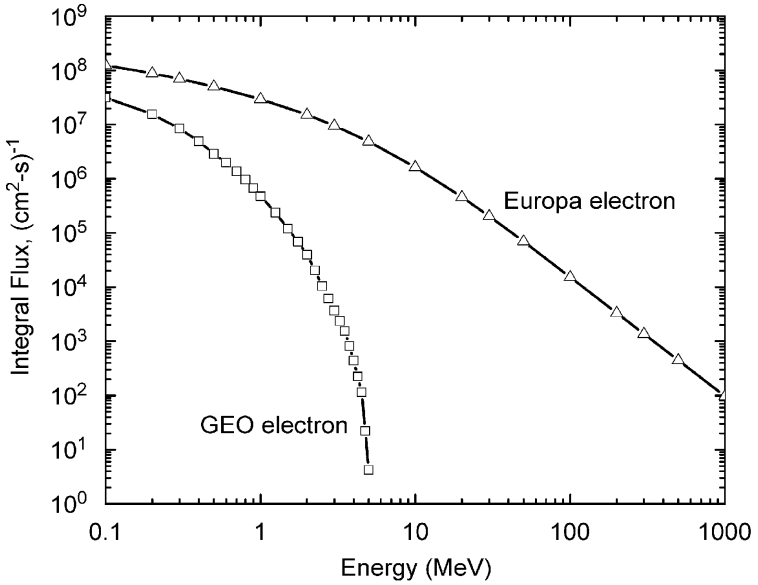

Figure 1.2: Comparison of high energy electrons in Earth orbit and around Jupiter near Europa. Reprinted from [12] with permission from Elsevier.

is selected or designed to withstand its intended environment. Typically parts are selected that can withstand several hundred krad(Si) of ionizing radiation over several years, if not decades. Space vehicles that travel to other planets are treated no different. The vehicle is designed to survive for the entirety of its mission. With the increasing interest in Jupiter, first due to the pictures sent back by Voyager and now by the photos from Juno, more missions will be sent to the gas giant and its curious moons. The radiation environment is much harsher than Earth, with Jupiter's large magnetic field trapping higher energy particles than found in Earth's magnetosphere [12]. Jupiter's magnetosphere is also ten times stronger than that of the Earth's. The plot in Fig. 1.2 shows the comparison between the two environments. With future missions directed toward Jupiter's moons, electronics will now need to withstand a TID of 1 Mrad or more [12], [13]. The following work presents a non-volatile, resistive memory technology able to survive and operate in a high energy particle environment far beyond 1 Mrad.

With the impending physical limitations of Si CMOS technology, there has been

a drive to develop better performance memories out of alternative materials and architectures [14]. Research into alternative technologies eventually led to the development of resistive memory devices. Several types of ReRAM currently exist, namely phase-change memory (PCM), metal-oxide memory, and conductive bridging memory [15]. Radiation testing has revealed that many of these ReRAM technologies are TID hard, with tolerance beyond that of current commercial memory used in space applications [16], [17]. These ReRAM technologies offer a promising solution to survivability in Jupiter's harsh radiation environment This discourse will examine Conductive bridging random access memory (CBRAM) in ^{60}Co γ-ray, heavy-ion and neutron environments to evaluate its potential survival and behavior in a Jovian environment.

1.2 CBRAM Resistive Memory

CBRAM is a non-volatile memory developed at Arizona State University. A CBRAM cell is a two terminal metal-electrolyte-metal device [15], [18]. The bottom cathode contact, as shown in Fig. 1.3, is an inert metal such as nickel (Ni) or tungsten (W). The solid-electrolyte layer is a metal doped chalcogenide glass that facilitates fast ion migration through the glass [19]. Two types of chalcogenide devices are examined in the following studies, Ag-$Ge_{30}Se_{70}$ and Cu-SiO_x. The top anode layer is an active metal that is easily oxidized. Typically, the active metal chosen is the same used to dope the electrolyte.

CBRAM is a type of electrochemical memory and relies on oxidation-reduction (REDOX) reactions to form and dissolve a conductive metal filament [20], [21], [22]. When a voltage is applied to the anode contact while the cathode is grounded, the metal (M) in the anode becomes oxidized and drifts along the applied electric field through the electrolyte. The oxidation reaction is listed in equation 1.1 and is shown

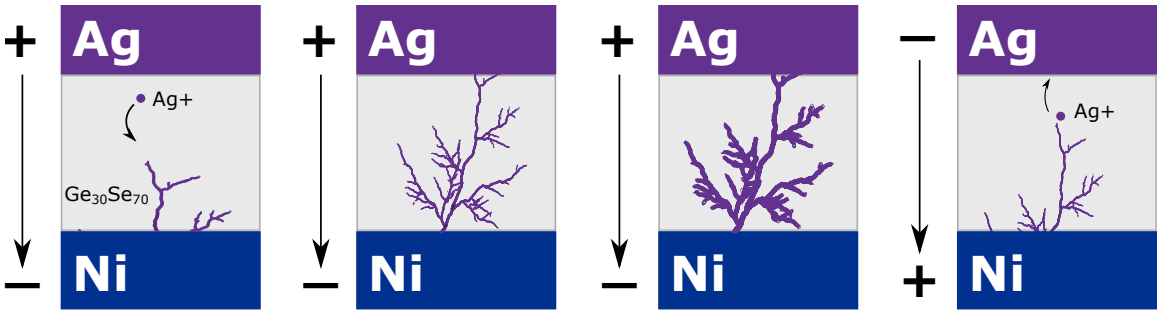

Figure 1.3: Filament formation and dissolution in a CBRAM cell. Applying a positive bias transports oxidized cations through the electrolyte to form a filament. Reversing the bias (right) reverses the REDOX reaction to dissolve the filament.

in the left most digram of Fig. 1.3. Once the metal ion reaches the cathode, the cation gains an electron, reducing the metal. The reduction reaction is shown in equation 1.2 where z is the oxidation state of the metal. While the bias is applied, the cations continue to migrate through the electrolyte toward the forming conductive filament. The filament forms from the cathode contact to the anode, as shown in the second diagram of Fig 1.3. Once the filament reaches the anode, the resistance between the two terminals greatly reduces, resulting in a low resistance state (LRS). Reversing the bias reverses the REDOX reaction, dissolving the conductive filament and directing the migration of metal ions back to the anode; as shown in the right most diagram of Fig. 1.3. With an absence of a conductive filament, the device is in a high resistance state (HRS).

$$M \rightarrow M^{z+} + ze^{-} \tag{1.1}$$

$$M^{z+} + ze^{-} \rightarrow M \tag{1.2}$$

Solid electrolytes facilitate the transport of ions by offering sites for the cations to hop between [22], [23]. In the presence of an applied electric field, the barrier between each site is lowered in the direction of the field, allowing cations to hop to the next

site in a coordinated fashion [24]. For a fixed temperature, the ionic drift velocity is exponentially dependent on the field between the anode and the cathode (including the reduced metal forming the filament). As the filament begins to grow, the field between the contacts increases, increasing the velocity of ion migration and filament formation. For a device with a 65 nm chalcogenide layer, initial filament formation may take several hundred nanoseconds to complete but subsequent programming and adjustment of the LRS can be performed in several nanoseconds [22],[25]. The rapid adjustment ability of CBRAM is an important quality for neuromorphic programming, which is discussed in more detail in Chapter 3.2.2.

1.3 Summary

This work will examine the response of CBRAM to high doses of ionizing radiation as well as to heavy ion irradiation. Chapter 2 will provide the method used to fabricate CBRAM as well as details on the film thicknesses and device geometry. Memory devices can be evaluated in a variety of ways. To measure the electrical properties of a single cell, current-voltage measurements are performed. Once programmed to a state, retention testing is used to measure how long that state can be maintained. To program a memory cell in a more conventional way, pulsed programming is used. Chapter 3 provides the procedures for evaluating the electrical characteristics of CBRAM including programming and state sampling. Chapter 4 presents the effects of ionizing and heavy-ion irradiation on the retention of state of CBRAM devices. In the presented experiments, the CBRAM was tested up to 24 Mrad($Ag_5Ge_3Se_7$) using ^{60}Co and up to ~60 Mrad($Ag_5Ge_3Se_7$) using multiple heavy ion sources. The calculated electrical and nuclear energy losses for each ion was used to distinguish which type of radiation environment CBRAM is most responsive to. Chapter 5 shows the effect of 14 MeV mono-energetic neutrons and 100 keV Li-ions

during DC programming. With increasing particle fluence, the programming window was shown to collapse due to displacement damage effects. In Chapter 6, the neuromorphic pulsed programming of Ag-$Ge_{30}Se_{70}$ and Cu-SiO_2 devices were tested in a ^{60}Co γ-ray environment. The CBRAM was shown to be susceptible to TID while being pulsed programmed *in situ*. Chapter 7 offers an explanation and discussion of the material changes occurring during irradiation. The work presented in this dissertation is summarized in the Conclusion.

Chapter 2

DEVICE FABRICATION

2.1 Fabrication

CBRAM devices evaluated in the following experiments were fabricated at Arizona State University in the NanoFab class 100 cleanroom facility operated by the Center for Solid State Electronics Research (CSSER). The full fabrication process is highlighted in Fig. 2.1–2.11.

The devices begin with a four inch diameter, 525 μm thick Si p-type wafer placed inside an Oxford Plasma Enhanced Chemical Vapor Deposition (PECVD) machine. A 100 nm layer of SiO_2 was deposited to provide isolation between the Si substrate and the device structures (Fig. 2.1). The oxide was deposited at 350°C with 20 W power for 1 minute and 24 seconds.

The nickel cathode layer was created by evaporating 65 nm of Ni onto the wafer using a Lesker PVD electron-beam (e-beam) evaporator. The chamber was pumped down to 3×10^{-6} torr prior to deposition. The Ni was deposited at a deposition rate of 0.8 Å/s to a total thickness of 65 nm, as depicted in Fig. 2.2. To pattern the Ni contact bar, hexamethyldisilazane (HMDS) was first spun onto the Ni surface at 3500

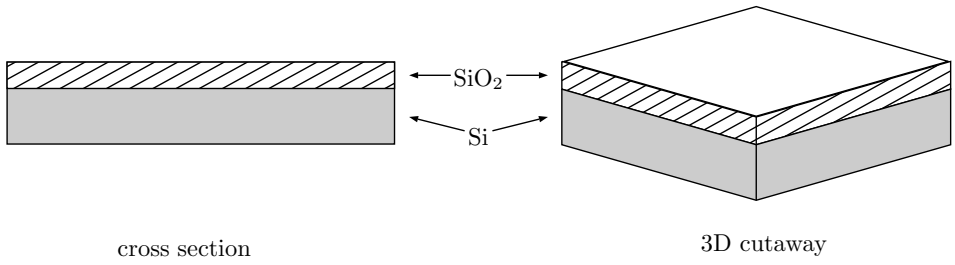

Figure 2.1: 100 nm SiO_2 deposited using PECVD.

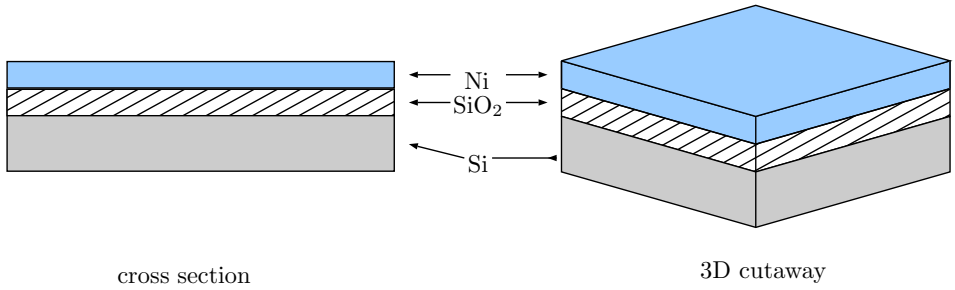

Figure 2.2: Deposition of 65 nm Ni.

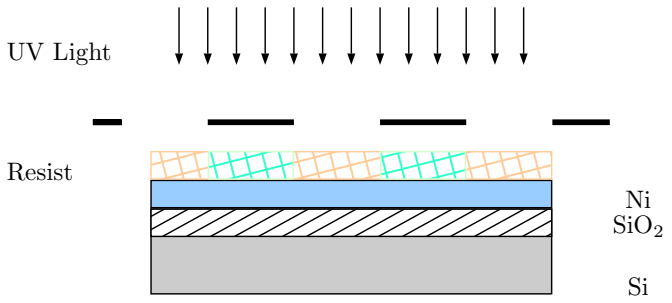

Figure 2.3: First lithography mask exposure to create cathode bar.

RPM for 30 seconds to promote resist adhesion. A 1 μm layer of AZ3312 photoresist was spun onto the treated nickel surface at 3500 RPM for 30 seconds. The wafer was then soft baked at 100°C for 60 seconds. Photo lithography was performed using an EVG 620 set to 45 mJ/cm^2 UV exposure. Mask #1 was used to create the Ni cathode bar positive image in the resist (Fig. 2.3). After exposure, the resist was developed for 90 seconds using AZ 300 MIF developer. The resist was then hard baked for three minutes at 110°C. The exposed Ni features were etched away after 4.5 minutes, using Nickel Etchant TFB (Nitric Acid). A representation of the etched feature is shown in the right hand side of Fig. 2.4. The resist etch mask was removed by soaking the wafer in acetone followed by a rinsing of isopropyl alcohol (IPA).

Several steps were used to form the active layer of the CBRAM arrays. Another

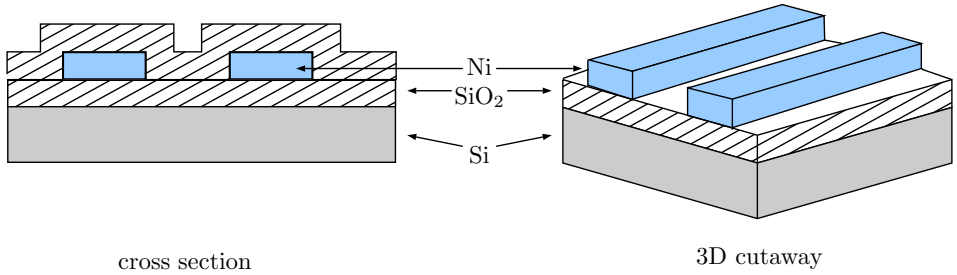

Figure 2.4: Ni layer wet etched to create cathode bar followed by PECVD deposition of SiO_2.

layer of 100 nm PECVD SiO_2 was deposited using the same recipe as the isolation layer. A double layer resist recipe was used to pattern the SiO_2 layer. HMDS was spun on at 4000 RPM for 30 s followed by AZ4330 resist at 4000 RPM for 30 s then soft baked at 100°C for 30 s. A second layer of AZ4330 was spun on and soft baked for a total resist thickness of 7 μm. Mask #2 was used to pattern the device region for etching (Fig. 2.5). The resist was exposed to 700 mJ/cm^2 and developed in AZ 300 MIF for 2.5 minutes. The features shown in Fig. 2.6 were etched through the SiO_2 layer using anisotropic reactive ion etch (RIE) for 3 min 20 s. The resist for the etch mask was removed with acetone and residual photoresist was ashed away after 10 min of O_2 plasma etch. Another double layer resist was used for the lift-off layer. Instead of two layers of AZ4330, after the application of HMDS, OCG825 resist was spun on at 4000RPM for 30 seconds and baked at 150°C for 1 min followed by a layer of AZ3312 spun on at 4000RPM and baked for 1 min at 95°C. The chalcogenide lift-off feature mask #3 was used to pattern the resist with UV exposure to 45 mJ/cm^2. This lithography step is depicted in Fig. 2.7. The resist was developed for 70 s using AZ 300 MIF. The wafer was placed into a Cressington 308R thermal evaporator where,

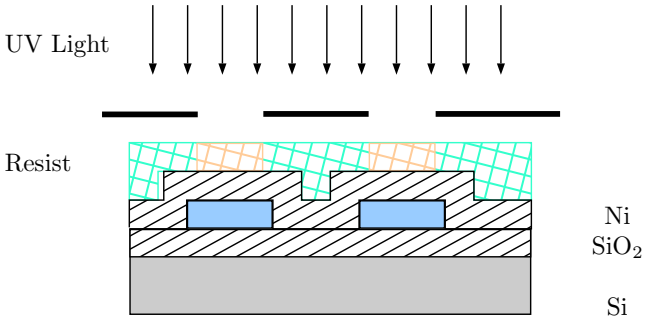

Figure 2.5: Second lithography mask to etch via through SiO_2.

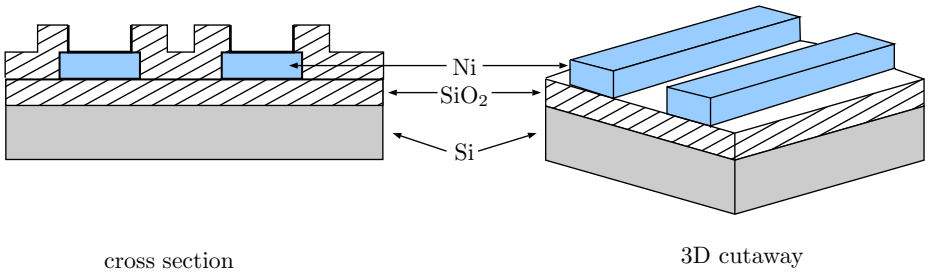

Figure 2.6: Vias dry etched through SiO_2 to Ni layer using RIE.

as shown in Fig. 2.8, 60 nm of $Ge_{30}Se_{70}$ was thermally evaporated followed by 30 nm Ag at a deposition rate of 1Å/s. As shown in Fig. 2.9, the $Ge_{30}Se_{70}$ layer was photo-doped with the Ag by exposing the device side (top) of the wafer to UV light for 27 min to a dose of 5.3 J/cm^2 [26]. The photo-doping process drives the Ag into the chalcogenide layer to a saturation of 33 .at% concentration [27], [28]. The expected Ag concentration profile is analyzed in [29]. After the photo-doping process, the wafer was placed back into the Cressington evaporator where 35 nm of additional Ag was deposited to form the top active metal anode. The resist was thermally shocked using 150°C before placing in acetone. The thermal shock helps to break up the deposited film, allowing a clean lift-off with sharp features. Fig. 2.10 shows the device structure after the resist is removed.

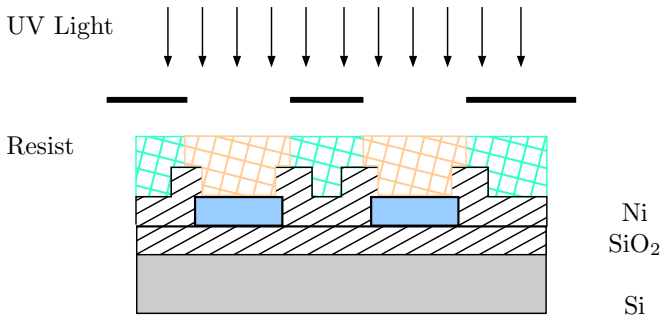

Figure 2.7: Third lithography mask for device layer lift-off.

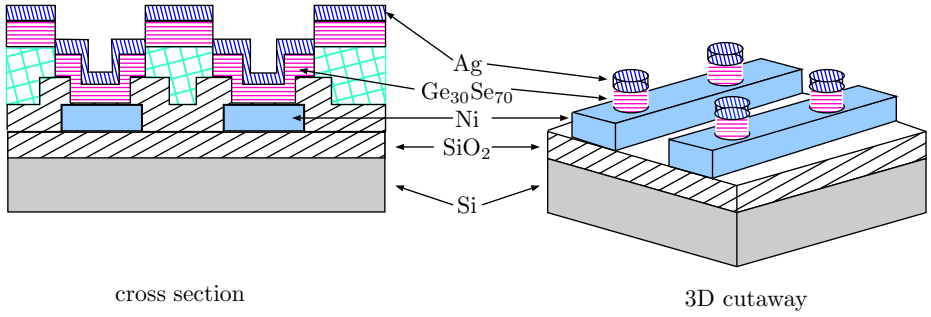

Figure 2.8: $Ge_{30}Se_{70}$ is deposited followed by Ag.

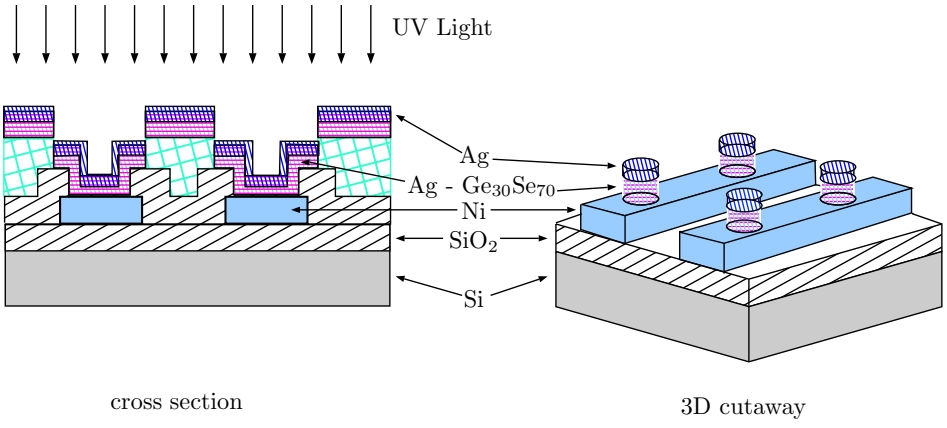

Figure 2.9: $Ge_{30}Se_{70}$ is photo-doped with Ag by exposing to UV light.

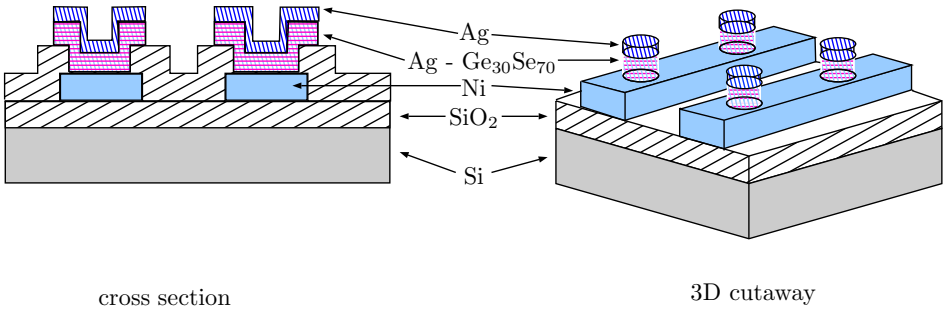

Figure 2.10: Additional Ag is deposited then the wafer is soaked in acetone to remove the resist and lift-off the excess material.

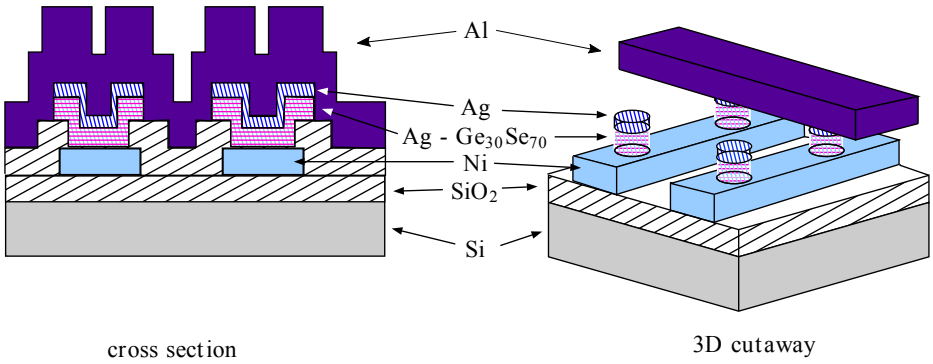

Figure 2.11: Al is deposited and lifted off to create top anode crossbar.

The final steps create the Al crossbar contacts across the anode of the devices. The double layer lift-off resist recipe was used for the Al features. Crossbar mask #4 was used to pattern the Al contacts, using the EVG for a UV exposure to 45 mJ/cm^2. The wafer was placed in the Lesker PVD sputtering machine and 350 nm of Al was deposited at 1.5 Å/s at a chamber pressure of 4.1 mtorr. The resist was again thermally shocked to allow for easy lift-off and placed in acetone. To finish the devices, the wafer was annealed at 120°C for 20 minutes. Fig. 2.11 depicts the complete layer stack of the CBRAM. A picture of the finished crossbar structure is shown in Fig. 2.12.

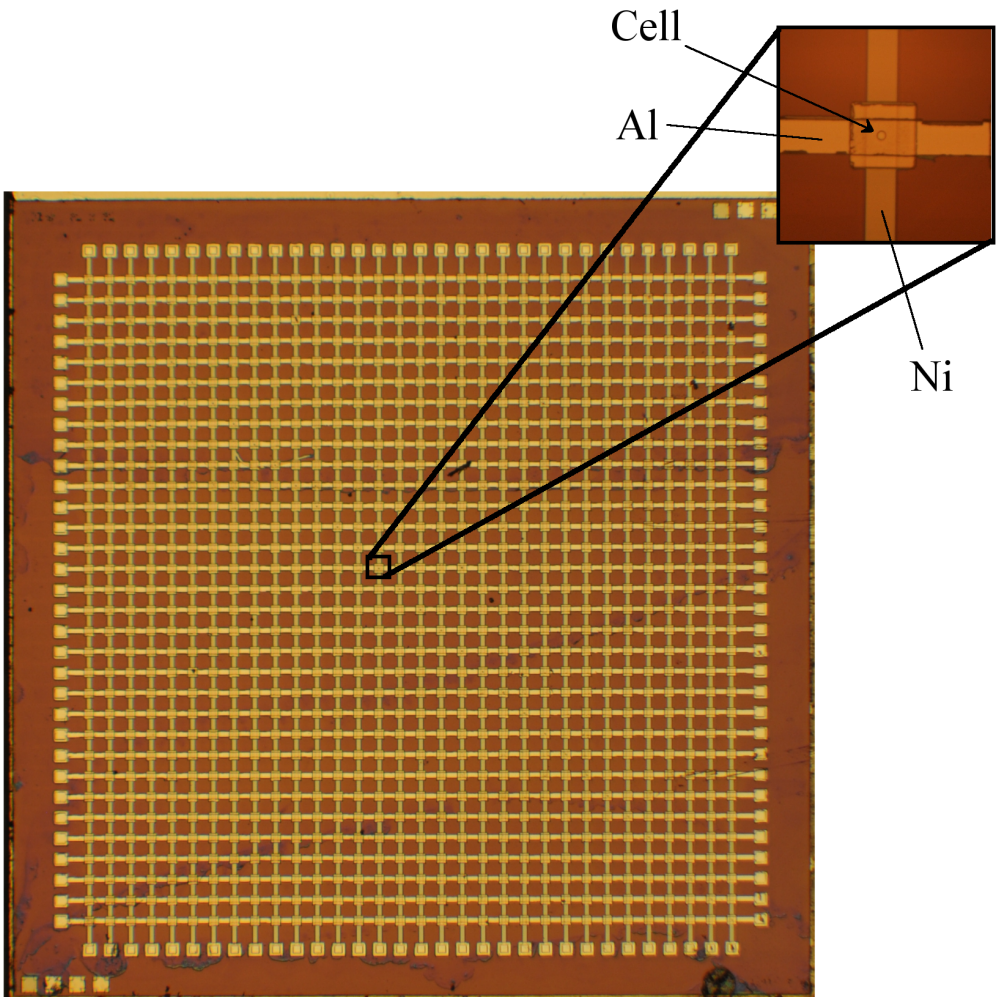

Figure 2.12: Fabricated crossbar tile. Zoomed image highlights the device contacts and active device region.

Chapter 3

DEVICE CHARACTERIZATION TECHNIQUES AND PROCEDURES

3.1 DC Testing

DC analysis is a useful technique used for extracting intrinsic electrical characteristics of semiconductor devices. A familiar example would be a transistor where the threshold voltage, triode/saturation regions, output resistance, and channel length modulation can all be extracted by performing DC sweeps. DC sweeps are performed in the lab using a source measurement unit (SMU) on a semiconductor device parameter analyzer such as the tried-and-true Agilent 4155B/4156C, or the newer Agilent B1500A. The standard test signal is a linear staircase sweep with uniform step size from a defined starting voltage V_{start} to a final stopping voltage V_{stop}. A depiction of a positive and negative staircase sweep with uniform step is shown in Fig. 3.1. A sweep that increments to the stopping voltage then decrements to the initial starting voltage is known as a double sweep.

A CBRAM element is a two terminal device. During a DC test, a bias is applied to the anode while the cathode contact is grounded. DC testing is performed on CBRAM cells to extract the intrinsic programming threshold, erase threshold, and high resistance state (HRS). The low resistance state (LRS) is dependent on the compliance current set and as such, is a user controlled parameter. The full DC analysis of CBRAM consists of two double sweeps; one positive to program the device and one negative to erase it. Depending on the material system of the device under test, the sweep range will vary. Typically the programming sweep range starts at 0 V and ends at a voltage beyond the observed programming voltage. For Ag-$Ge_{30}Se_{70}$

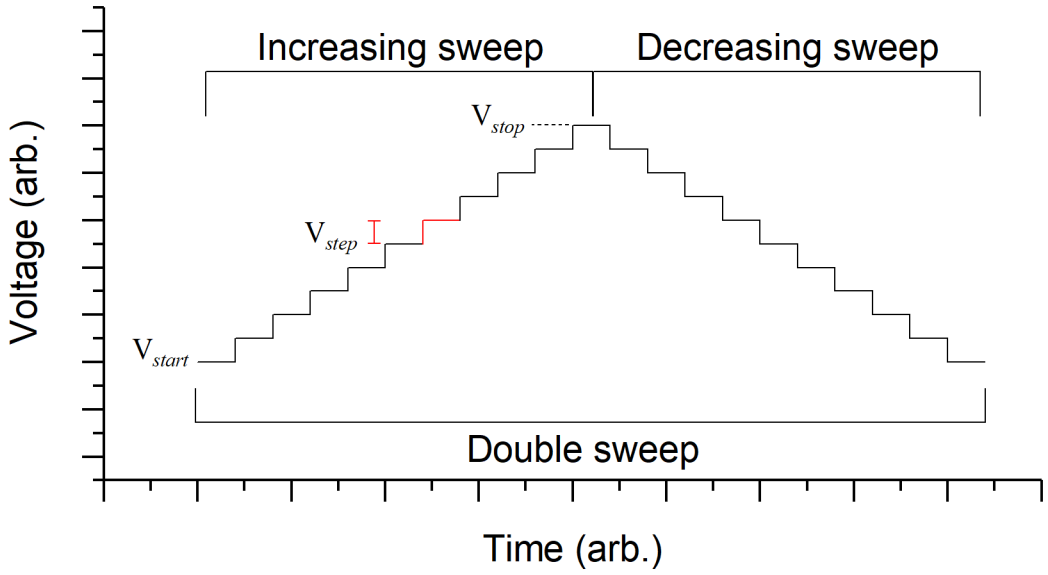

Figure 3.1: DC staircase sweep with uniform voltage steps. Sweeps can be performed in an increasing or decreasing manner.

devices, the upper range is typically 0.5 V. The erase sweep range is selected in a similar manner with -0.8 V used for the sweep range. The voltage step chosen needs to be small enough resolve a smooth curve with good data resolution. The best rule-of-thumb is to maintain 50 or more steps across the range of the sweep. A simple formula for the voltage step V_{step} in terms of the sweep voltage start and stop is shown in eqn. (3.1) below.

$$V_{step} \leq \frac{V_{stop} - V_{start}}{50} \tag{3.1}$$

The parameters used for performing programming and erase DC sweeps are shown in Table 3.1, though depending on the behavior of an individual device, the testing parameters may be adjusted.

A typical current-voltage (I-V) hysteresis curve for Ag-$Ge_{30}Se_{70}$ is shown in Fig. 3.2, with the red curve showing the response to the positive programming voltage sweep and the black curve depicting the response to a negative erase sweep. The

Table 3.1: DC Sweep Parameters for Ag-$Ge_{30}Se_{70}$ and Cu-SiO_2 CBRAM

Parameter	Ag-$Ge_{30}Se_{70}$		Cu-SiO_2	
	Programming	Erase	Programming	Erase
V_{start}	0 V	0 V	0 V	0 V
V_{stop}	0.5 V	-0.8 V	1.5 V	-0.9 V
V_{step}	10 mV	-10 mV	20 mV	20 mV
$I_{compliance}$	1 μA	10 mA	500 nA	10 mA

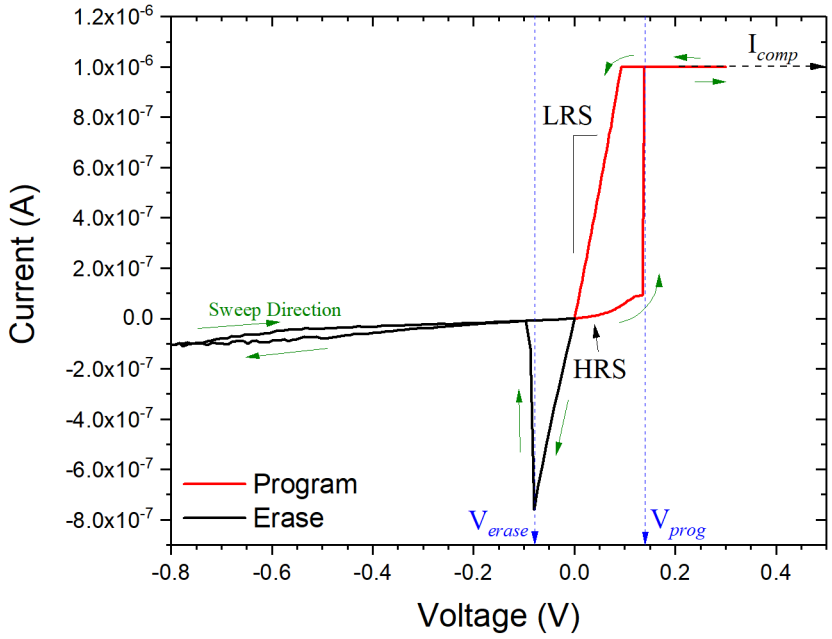

Figure 3.2: DC I-V curve for an Ag-$Ge_{30}Se_{70}$ device. Key parameters are highlighted by the arrows.

programming threshold (V_{prog}) is observed as an abrupt increase in current from the HRS to the LRS. The LRS is set by the compliance current (1 μA) and is extracted from the Ohmic response around 0 V. The erase threshold (V_{erase}) occurs when the current decreases back to the HRS during the erase sweep.

Read Biasing and Retention Testing

An essential characteristic of non-volatile memory is its ability to hold a programmed state for an extended period of time. To measure the retention of state, the CBRAM devices are programmed to a state of choice and a read bias is periodically applied to measure the state at that moment. For the tests presented Chapter 4, a small DC voltage is applied across the terminals while the current is measured. The read bias is selected to be significantly smaller than the programming threshold. Current Ag-$Ge_{30}Se_{70}$ CBRAM has a programming threshold in the order of 150 mV so the read bias is typically selected to be 30 mV to 50 mV with the larger read voltage used in setups with higher noise floors. Depending on the time-frame of testing, the read voltage may be applied continuously (such as in real-time *in situ* testing) or periodically over a long period of time (state endurance evaluation).

Retention testing is carried out using Sampling Mode on a parameter analyzer. For long-term testing, a 30 mV bias is applied to the anode for approximately 15 ms while the current is sampled multiple times. Between reads, both the anode and cathode are held at ground. Retention endurance tests may span over days or even weeks with reads taken every hour or more depending on the time resolution needed for the characterization. For short term retention testing the read bias may be applied over several minutes. The most convenient method for continuous biasing is to use Sampling Mode with the current sampling interval set at 1 s or longer. The Sampling Mode parameters used for performing continuous and periodic testing are summarized in Table 3.2.

Table 3.2: DC Sampling Parameters for Retention Testing of CBRAM

Parameter	Continuous Bias	Periodic Sample
V_{sample}	30 mV	30 mV
$t_{interval}$	1 s	5 ms
$N_{samples}$	$t_{total}/t_{interval}$	5
$f_{measure}$	continuous	1 hr^{-1}

3.2 Pulsed Testing

The state of a CBRAM device is manipulated by the application of an electric field—whether it be by applying an incrementally increasing voltage until the device changes state or by applying a voltage beyond the programming threshold for a fraction of a second. As mentioned in Chapter 1, the programming of a CBRAM cell is rate limited by the hoping of metal ions through the chalcogenide glass. The resistive state of a device can therefore be controlled by applying a particular voltage for a specific amount of time [22]. The larger the applied voltage, the faster the device will program. For a device with a 90 nm chalcogenide layer, a bridging filament will fully form within tens of nanoseconds [23]. Two types of pulse programming can be performed on CBRAM devices: traditional binary state programming and incremental neuromorphic programming.

3.2.1 Binary Cycling

To obtain the pulse widths necessary for properly tuning the resistive state, an Arbitrary Waveform Generator such as an Agilent 81160A, is used for applying the programming signals. A rise/fall time ($t_{rise/fall}$) between 50 ns to 100 ns is typically used, with the longer ramp time used in setups with significant inductance (ringing)

Table 3.3: Pulse Parameters for Binary State Cycling

Parameter	Set (LRS)	Erase (HRS)
V_{pp}	0.8 V	-0.8 V
t_{pulse}	10 μs	10 ms
$t_{rise/fall}$	100 ns	100 ns
V_{read}	30 mV	30 mV

issues. Since either the pulse amplitude or width can be adjusted to control the programmed states, for simplicity, the voltage is selected to be fixed. The same amplitude is used for both setting and erasing the filament, with the pulse polarity inverted for erasing. Table 3.3 shows the pulse parameters used for binary state cycling. The pulse width (t_{pulse}) for erasing the filament is wider than the set time to ensure that the filament is substantially dissolved.

After a pulse is applied, it is necessary to measure the resulting resistive state. In the setup used to test the device state in Chapter 6, a DC read bias was applied using an SMU. Instruments like the Agilent B1500 can contain high speed pulse generator units (PGU), SMUs, and pulse measurement units (PMU). Tests performed at Sandia National Laboratories used the B1500. In the setup at ASU, an Agilent 4156C SMU and Agilent 81160A pulse generator were used with a LabVIEW controlled Agilent E5250A switch matrix to switch between sources. An example programming signal for pulsed cycling is shown in Fig. 3.3.

3.2.2 Neuromorphic Programming

The conductive filament growth of CBRAM devices can be modulated, allowing for precise control of the resistive state. The large spread in allowed resistance states makes the CBRAM ideal for incremental neuromorphic programming which requires a multilevel programming capability. To perform incremental pulsed programming,

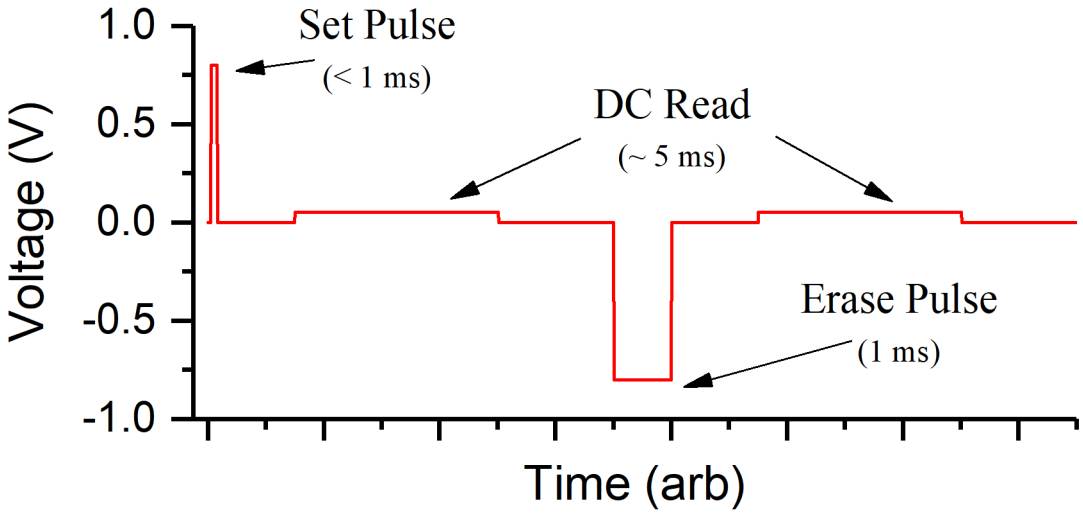

Figure 3.3: Set, read, erase, read signal used for performing binary pulsed cycling programming.

the device is first set to a mid-range LRS using either a DC sweep or pulsed programming. For example, if the desired LRS range is from 3 kΩ to 300 kΩ, an initial LRS of 100 kΩ may be used. Higher power pulses are needed to make the initial transition from an HRS to an LRS. Ideally, identical pulses are preferred for performing neuromorphic programming, so it is necessary to remain in the LRS region during operation. Neuromorphic programming varies from binary cycling, in that the same pulse will be applied multiple times before reversing the polarity of the pulse. Lower power pulses are used for multilevel programming to allow for smaller transitions of states. A typical set of programming parameters are listed in Table 3.4. The action of *Potentiation* and *Depression* are used to describe the incremental increase in conductance and incremental decrease in conductance respectively [30],[31]. To perform potentiation, a small positive pulse is applied to the device anode followed by a read bias to measure the resulting state. The positive pulse followed by the read bias is applied several times to incrementally increase the conductance state. Depression is performed in a similar manner, but with a negative programming pulse. An example

Table 3.4: Pulse Parameters for Neuromorphic Programming

Parameter	Potentiation	Depression
V_{pp}	0.8 V	-0.8 V
t_{pulse}	100 ns	10 μs
$t_{rise/fall}$	50 ns	50 ns
V_{read}	30 mV	30 mV

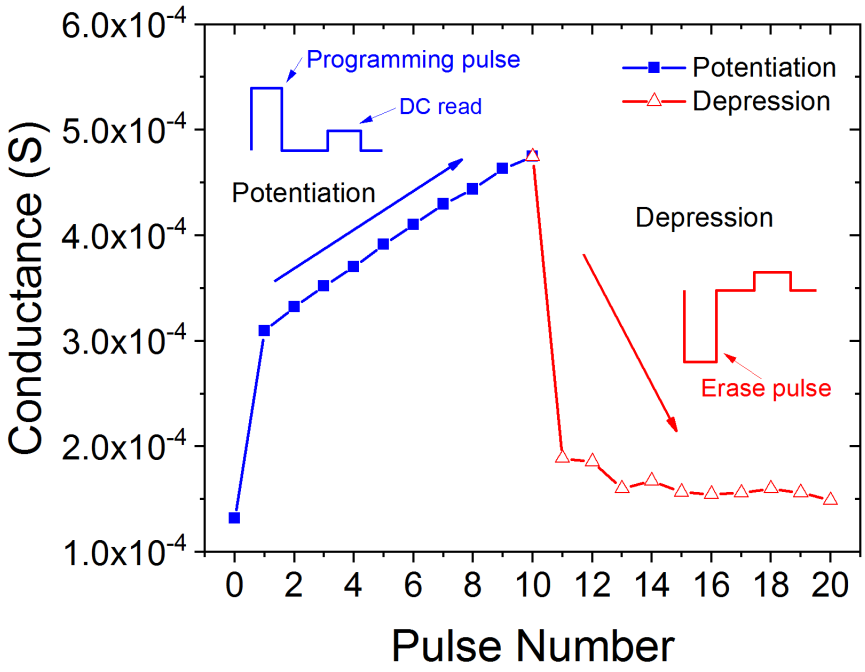

Figure 3.4: Incremental pulsed programming for neuromorphic applications. Positive pulses result in an incremental increase in conductance while negative pulses cause an incremental decrease.

of neurmorphic programming of a CBRAM device is shown in Fig. 3.4. The black curve shows the near linear trend of conductance increase with uniform pulses applied. The red curve shows the exponential like reduction of the conductance during depression for uniform pulses. Ideally, programming parameters should be selected such that a linear change in conductance is exhibited for each applied pulse.

Chapter 4

EFFECTS OF RADIATION ON STATE RETENTION

4.1 Introduction

Non-volatile memory is typically used to store data for extended periods of time so it is necessary to examine how the retention of state can be affected in a radiation environment for use in space-based applications. CBRAM has been shown to be total ionizing dose (TID) tolerant up to 10 Mrad($Ge_{30}Se_{70}$) for Ag-$Ge_{30}Se_{70}$ devices [32], [33] and 7.1 Mrad(SiO_2) for Cu-SiO_2 devices [34]. The previous studies did not examine the TID or displacement damage (DD) threshold required to cause a deviation from the programmed resistive state. This Chapter will investigate the effects of a combined TID and DD environment generated by heavy ion bombardment as well as examine the behavior of programmed CBRAM states in a TID environment.

Three ion environments were explored, each with a different linear energy transfer (LET) and non-ionizing energy loss (NIEL). In the following tests, the CBRAM devices were exposed to 100 keV Li, 200 keV Si, or 1 MeV Ta ions while measuring the retention of state of the programmed CBRAM devices. A set of 200 keV Si-ion exposure results were first presented in [35] and investigated how the resistive state changed during an ion beam raster scan across an individual memory cell. Further testing with Li, Ta, and Si ions was performed to determine the dose threshold at which a CBRAM device fails to retain its state. To investigate the TID environment, a ^{60}Co γ-ray exposure was performed up to 27 Mrad($Ge_{30}Se_{70}$).

4.2 Heavy Ion Bombardment

4.2.1 Experiment Setup

Heavy ion irradiations were performed at the Ion Beam Laboratory (IBL) at Sandia National Laboratories. Exposures using 100 keV Li^{+} and 200 keV Si^{2+} ions were performed using the NanoImplanter (NI) raster scanning focused ion beam. The method of using the NI to perform displacement damage studies in resistive memory was previously demonstrated on TaO_x devices by Hughart *et al.* in [36–38]. A Tandem accelerator was used to accelerate Ta-ions at 1 MeV down a beam line where the beam was focused to several millimeters. Studying multiple ion types with different electronic energy loss and nuclear energy loss through the device, allows for a comparison of effects due to either TID or DD.

100-keV Li-ion Bombardment

For the Li-ion exposure, CBRAM crossbars with 5 μm diameter devices along the diagonal of the array were used. A bare CBRAM die was placed on a stage inside the vacuum chamber of the NI and probed to obtain an electrical connection. The functionality of each device was verified using a DC I-V sweep with an Agilent B1500 parameter analyzer. Each device was set with a 10 mV double staircase sweep from 0 V to 0.5 V to 0V and erased with a sweep from 0 V to -0.8 V to 0 V. Three devices were erased into an HRS and three were programmed to an LRS by setting a 10 μA compliance current. A small (sub-programming threshold) DC I-V read sweep from 0 V to 30 mV was used to sample the resistive state of the device before irradiation. Each device was exposed and tested individually. The 40 nm diameter Li beam was raster scanned in 40 nm steps over a 25 μm $\times$ 25 μm area over a device to a fluence of 10^{11} ions/cm^2. The device remained probed during irradiation with no bias applied.

After irradiation, the 30 mV read sweep was applied to measure the state of the device. Exposures were continued in 10^{11} ions/cm^2 fluence steps to 10^{12} ions/cm^2 where the fluence was increased to 10^{12} ions/cm^2 steps and at 10^{13} ions/cm^2 the step was increased to 10^{13} ions/cm^2. A read sweep was performed on the device after each fluence step. Each device was irradiated up to a total fluence of 5×10^{13} ions/cm^2 or until the device shorted.

200-keV Si-ion Bombardment

The Si-ion exposures were performed in the same manner as the Li-ion testing except that the devices used had the Al contact offset from the device area, similar to the device shown in Fig. 4.1. The devices used were from the same wafer as the crossbar devices but located on a separate die. Si-ion bombardment was performed on two devices programed to an HRS and four devices set to an LRS, set using a 25 μA compliance current. Prior to exposure, each device was DC swept to verify the functionality of the device. Each device was tested individually. The beam used during Si testing had a 30 nm beam diameter and was raster scanned in 20 nm steps across the device area. A 40 μm $\times$ 40 μm scan window was used to ensure that the beam hit the device area. The devices were irradiated in 2×10^{11} ions/cm^2 fluence steps until the device was observed to fail.

1-MeV Ta-ion Bombardment

Three devices were irradiated with Tandem accelerated 1 MeV Ta ions. The devices tested were those described in [33] with the Al contact offset from the area of the CBRAM cell; as depicted in the inset of Fig. 4.1. The devices were wire bonded in a 24 pin DIP and placed on a circuit board inside the beam line with BNC accessible connections to an Agilent 4155 parameter analyzer. Two of the devices were DC

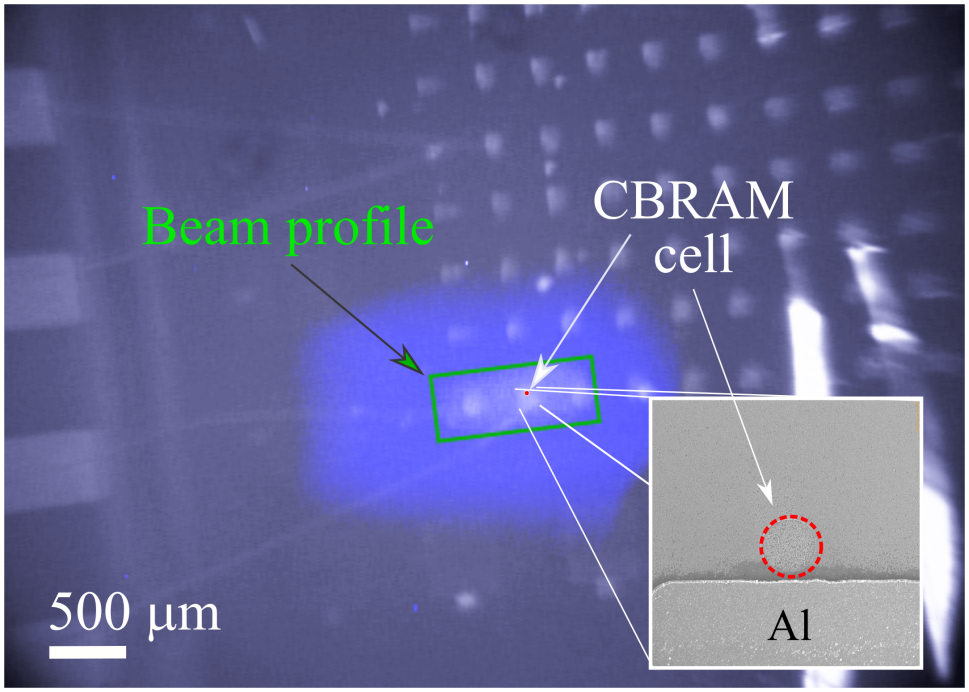

Figure 4.1: Ta-ion beam profile on an exposed CBRAM device. The green square marks the profile of the Ta beam and the red circled region marks the location of a tested device. The bottom right inset shows the device in higher detail and highlights the offset Al contact.

cycled and erased into an HRS while the third device was cycled and programmed into an LRS with a 10 μA compliance current. The Ta ion beam was approximately 500 μm $\times$ 1000 μm and fully covered the device area, as shown in the beam profile overlay in Fig. 4.1. During each exposure, a 50 mV read bias was applied to the anode contact with the cathode grounded.

The beam parameters used for each ion type are shown in Table 4.1

4.2.2 SRIM Calculations

Prior to ion beam testing, Stopping and Range of Ions in Materials (SRIM) calculations were performed to determine the ion energy needed such that the ion would stop in the Ni layer or beyond [39]. The total average energy loss of each tested ion, as it passes through a CBRAM device, is shown in Fig. 4.2. The device depth in Fig.

Table 4.1: Beam Parameters for Heavy Ion Retention Testing

Ion	Li	Si	Ta
Energy	100 keV	200 keV	1 MeV
Charge State	1	2	1
Initial Dwell Time	5.6 μs	0.17 μs	100 μs
Beam Current	36.0 fA	1.49 pA	89.8 fA
Scan Window	25 $\times$ 25 μm	40 $\times$ 40 μm	fixed beam
Beam Step	40 nm	20 nm	0 nm
Beam Diameter	40 nm	35 nm	500 μm $\times$ 1000 μm
Initial Fluence Step	10^{11} ions/cm^2	2×10^{11} ions/cm^2	1.8×10^8 ions/cm^2
Approx. Dose Rate Per Dwell	4.18×10^{10} rad/s	1.04×10^{13} rad/s	3.39×10^7 rad/s

4.2 is in reference to the top of the Ag anode layer. The crossbar device used during Li-ion testing contained 350 nm of Al so its thickness is represented as a negative depth above the Ag interface. The material compositions and properties used for SRIM analysis is listed in Table 4.2. The LET and NIEL of each ion as it passed through the $Ag_{33}(Ge_{30}Se_{70})_{67}$ chalcogenide layer is shown in Fig. 4.3. The results were used to estimate the TID (rad($Ag_5Ge_3Se_7$)) deposited and the non-ionizing dose in the switching layer of the CBRAM devices. The LET and NIEL values generated from SRIM were converted to TID and a displacement damage dose (DDD) using the following equations,

$$TID = LET \cdot \Phi \cdot K \tag{4.1}$$

$$DDD = NIEL \cdot \Phi \cdot K \tag{4.2}$$

where $K = 1.6 \times 10^{-8}$ rad·g·MeV^{-1} and Φ is the fluence in ions/cm^2. Fig. 4.3 indicates that the deposited dose in the switching layer should be relatively uniform

Table 4.2: Physical Properties and Compositions for SRIM Analysis of CBRAM

Composition	Density (g/cm^3)	Thickness (nm)
Al	2.70	350
Ag	10.47	35
$Ag_5Ge_3Se_7$	6.30	70
Ni	8.89	65
SiO_2	2.32	100

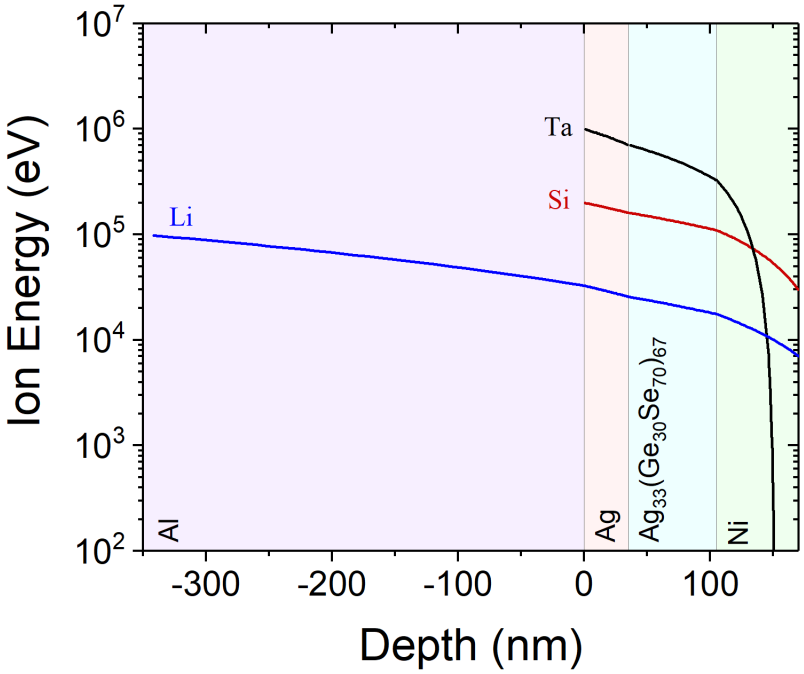

Figure 4.2: SRIM calculated ion energy of Li, Si and Ta ions as they pass through the CBRAM device.

throughout.

Transport of Ions in Matter (TRIM) is the Monte Carlo extension of SRIM and was used to determine the distribution of ion stopping ranges throughout the material stack. TRIM simulations were performed using 20000 ions with detailed calculations and full damage cascade. TRIM assumes a temperature of 0 K so annealing effects at room temperature (298 K) are not taken into consideration. The ion implantation

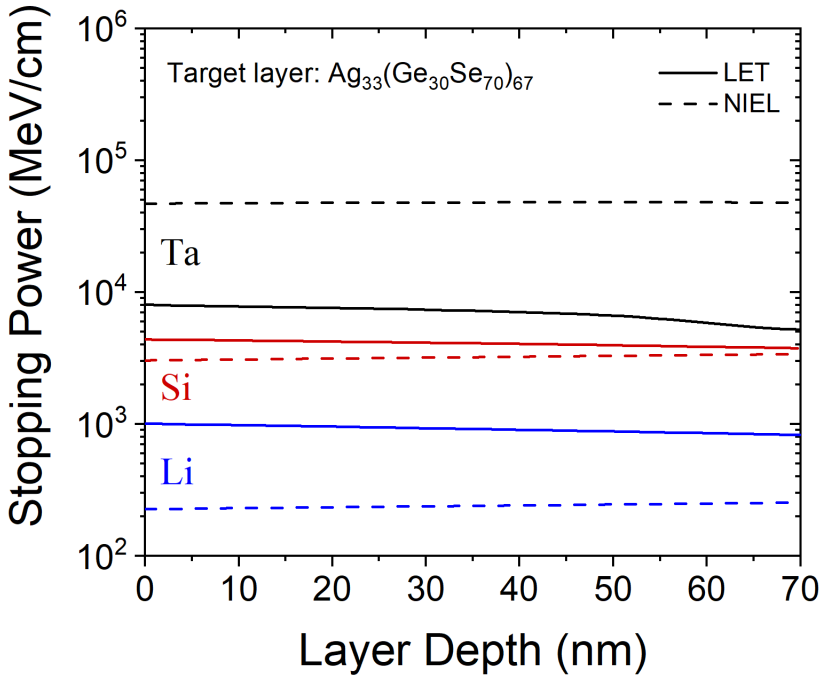

Figure 4.3: LET and NIEL of a Li-ion, Si-ion and Ta-ion as they pass through the chalcogenide switching layer.

distribution of each ion is shown in Fig. 4.4. The ion counts are binned with 25 Å wide bins and normalized to the maximum Ta-ion count. Fig. 4.4 shows that 1 MeV Ta-ions and 200 keV Si-ions have similar implantation profiles with the majority of ions implanting in the Ni layer as expected from SRIM results. The 100 keV Li-ions mostly implant in the Ni layer but the implant profile in the chalcogenide layer is more evenly distributed than for the Si and Ta ions. The Li bombardment also implants more ions into the Ag layer than either the Si or Ta ions.

The distribution of vacancies caused by displacement damage was also calculated from TRIM and is shown in Fig. 4.5. The displacements are a result of NIEL where the energy transfered scattered an atom from its original location. The total displacements are the sum of both vacancies and replacement collisions though the vacancies constitute more than 95% of the total displacements. Of the total vacancies,

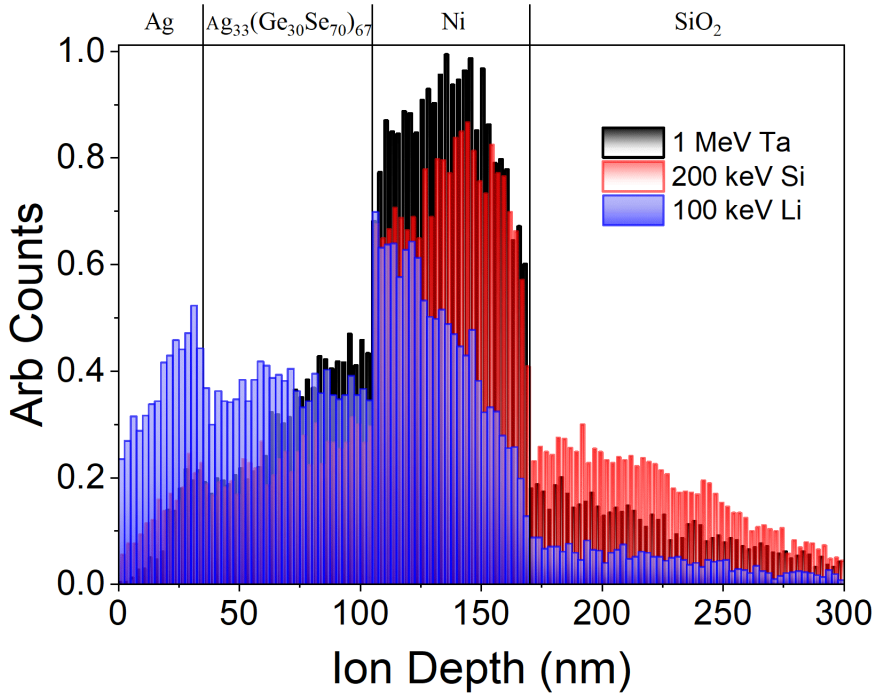

Figure 4.4: Heavy ion stopping ranges in the CBRAM stack calculated using TRIM.

for all three ions, displacement of Se atoms makes up for approximately 41% of the vacancies while Ag and Ge each make up ≈29%.

4.2.3 Observed Effects

100-keV Li-ion Bombardment

For the Li ion exposure, three devices were initially set to an HRS while three others were set to an LRS. The resistance state of the six devices versus the accumulative Li-ion fluence is shown in Fig. 4.6. The TID calculated using SRIM is marked on the top x-axis. Devices programmed to an HRS are plotted with dotted lines while the devices set to an LRS are solid lines. Of the devices programmed to an LRS only device 3 shorted after a fluence of 3×10^{13} ions/cm^2. Devices 1 and 2 failed to retain their initial state after a fluence of 10^{13} ions/cm^2 but they did not short. For the three devices programmed to an HRS devices 5 and 6 were shorted to an LRS.

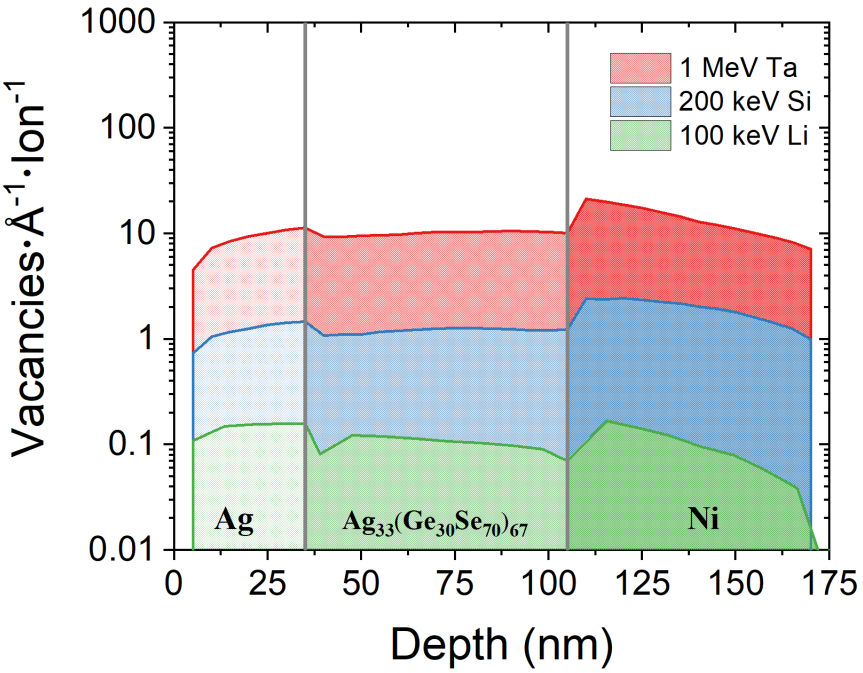

Figure 4.5: Vacancies produced by heavy ion bombardment in the Ag / Ag-GeSe / Ni layers for Li, Si, and Ta ions.

Device 5 shorted at a fluence of 2×10^{13} ions/cm^2. Device 6 decreased in resistance after a fluence of 3×10^{12} ions/cm^2 and shorted after 3×10^{12} ions/cm^2. Device 4 did not transition to an LRS but decreased slightly in resistance after a fluence of 10^{13} ions/cm^2.

200-keV Si-ion Bombardment

The results of the 200-keV Si ion exposure is shown in Fig. 4.7. All six devices tested showed a decrease in resistance at fluences above 10^{12} ions/cm^2. HRS device 1 decreased in resistance at 2×10^{12} ions/cm^2 and LRS devices 3 and 4 decreased at 10^{12} ions/cm^2 and 3.4×10^{12} ions/cm^2 respectively. HRS device 2 and LRS devices 5 and 6 did not decrease until and 2×10^{13} ions/cm^2. Unlike the state transition of device 1, once the resistive state of device 2 began to decrease, the change was

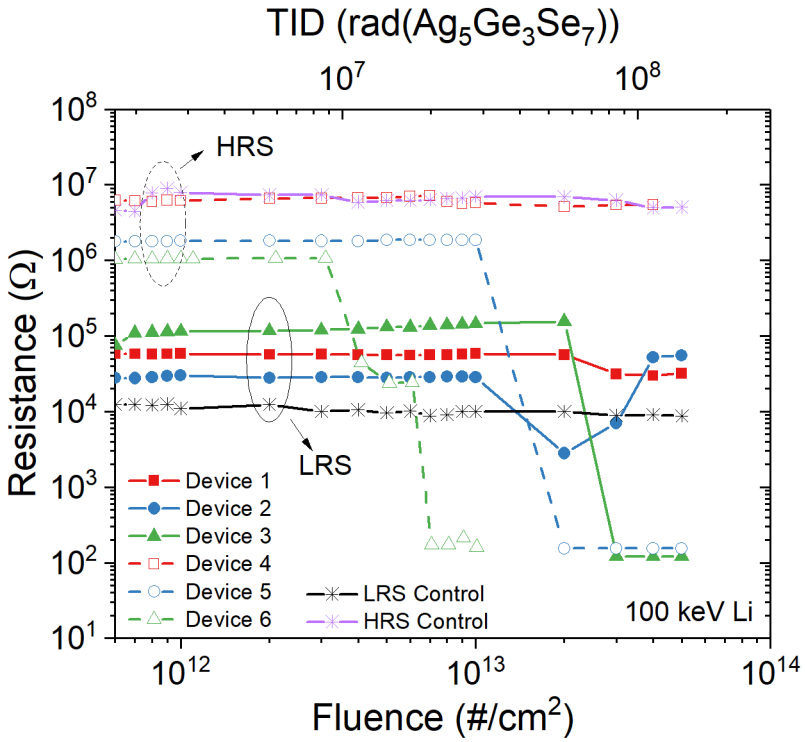

Figure 4.6: Resistive state of CBRAM devices exposed to 100 keV Li-ions.

gradual with increasing fluence.

1-MeV Ta-ion Bombardment

The post resistance state after each pulse versus accumulative fluence is plotted in Fig. 4.8 for the 1 MeV Ta-ion exposure. Devices 1 and 2 were set to an HRS prior to exposure and device 3 was set to the LRS. Both devices in the HRS transitioned to a lower resistance after a fluence of 10^{12} ions/cm^2 and 3×10^{12} ions/cm^2 for devices 2 and 1, respectively. The device in an LRS was only tested up to 6×10^{11} ions/cm^2 with no significant change in resistance observed.

Fig. 4.9 was constructed to assess if TID or DDD played the greater role in the state failure during retention testing. Using the point at which the resistance reduced by more than a half decade, the TID and DDD were calculated at the fluence step prior to failure. At failure, the 1-MeV Ta ions are shown to produce six times the DDD

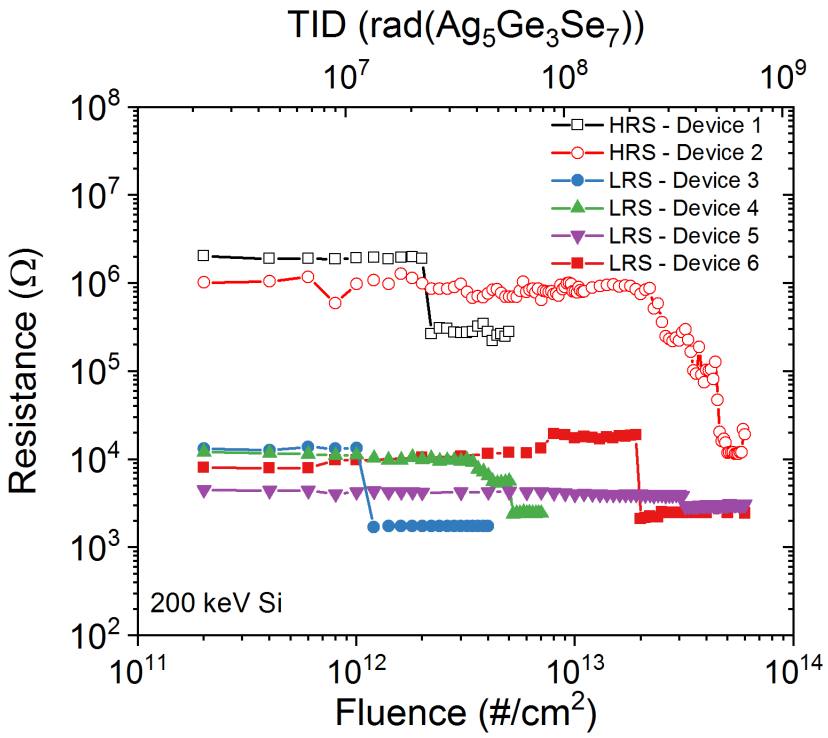

Figure 4.7: Resistive state of CBRAM devices exposed to 200 keV Si-ions.

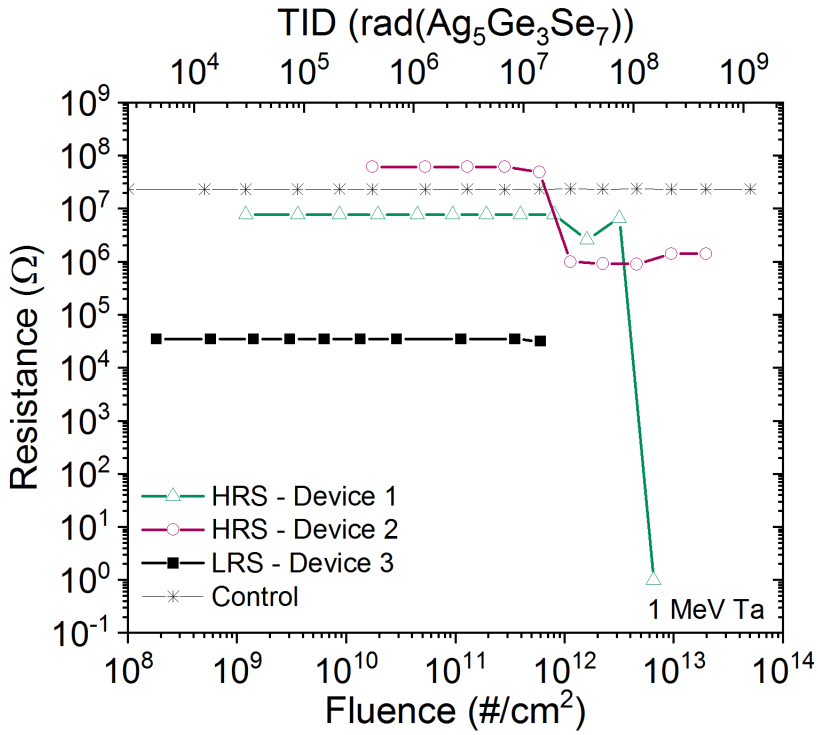

Figure 4.8: Resistive state of CBRAM devices exposed to 1 MeV Ta-ions.

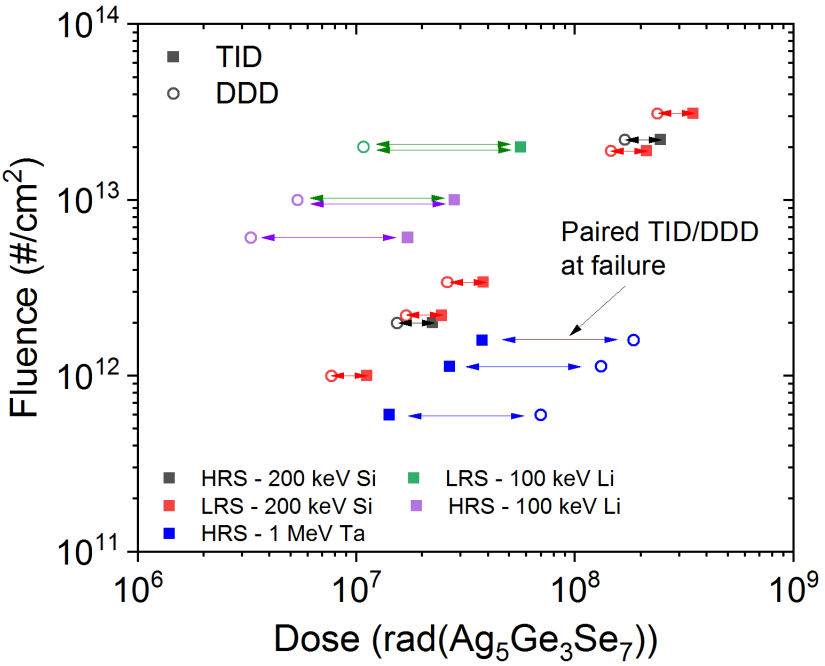

Figure 4.9: Displacement damage dose and TID of each device at retention failure due to irradiation. TID values at failure appear to be more highly correlated than DDD for Li, Si, and Ta-ion bombardment.

as 200-keV Si and 10 times the DDD as the 100-keV Li ions though most devices experienced resistance decreases within the same magnitude of TID. This strongly suggests that the observed changes were a result of TID. Based on the results of the heavy ion exposures, the mean TID threshold for resistance change was found to be 30.1 Mrad($Ag_5Ge_3Se_7$), excluding the three extreme doses (>100 Mrad) values encountered during Si-ion testing.

4.3 200-keV Si-ions Transient Testing

During the heavy ion retention testing, the resistive state of the CBRAM cell is measured following the exposure to the ion beam. To better explore the behavior of a CBRAM cell during a heavy ion beam scan, transient *in situ* measurements were performed. The purpose of this test was to determine if the observed resistance

changes due to heavy ion bombardment were gradual (uniform) across the device area or if changes were sudden and dominant to particular areas of the device. The NI beam can be focused to tens of nanometers in diameter and is useful for pinpointing sensitive areas of the device [36].

4.3.1 Experiment Setup

The devices used for Si-ion transient testing were from the same wafer as the devices used for Ta-ion testing. A bare die was loaded into the NI and the chamber was pumped down to $< 10^{-7}$ torr. The anode and cathode contacts of a single cell were probed. An electron beam was scanned across the device to verify its position and to align the beam over the device area. Prior to exposure the device was DC cycled as described in Chapter 3, to obtain the I-V characteristics and to verify device functionality. Each device was erased into the HRS prior to heavy ion exposure. The circuit used for monitoring the device *in situ* is shown in Fig. 4.10. During the ion beam scan the anode was biased with a 30 mV read voltage to monitor the change in resistance state. The cathode was connected to an amplifier to increase the signal into the analog-digital converter (ADC). After exposure, the device was DC cycled to determine the functionality of the device. During the ion beam scan, the resistance state of the CBRAM device was monitored live time during the entirety of each scan. To ensure a resistance state change, the fluence of each scan was 4.2×10^{13} ions/cm^2 or above. The beam parameters used for each device tested is shown in Table 4.3.

4.3.2 Observed Effect

All three devices were observed to decrease in resistance during the 200 keV Si exposures. The beam parameters set for each test are listed in Table 4.3 All three devices examined were 10 μm in diameter and were erased to the HRS prior to

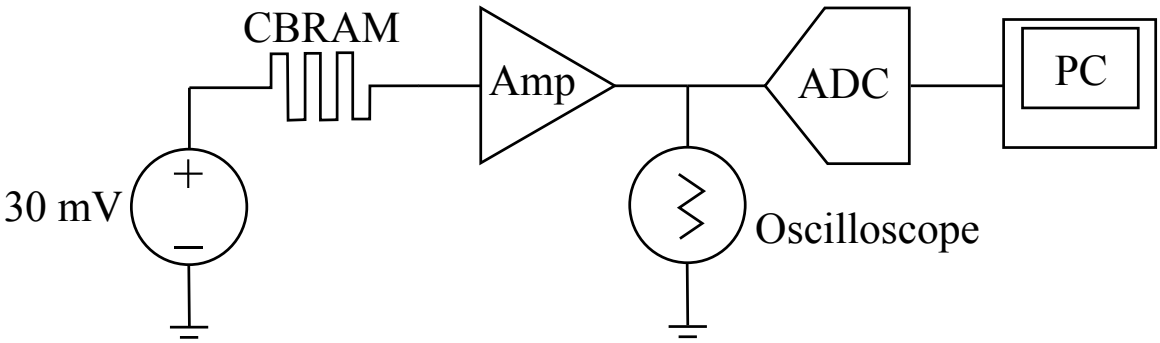

Figure 4.10: Circuit used to bias and monitor the CBRAM device during Si-ion exposure. Changes in resistance were monitored real time using an oscilloscope while dwell number and time was logged to the computer.

Table 4.3: Test Parameters for 200 keV Si^{2+} *in situ* Ion Beam Scans

Parameter	Device 1	Device 2	Device 3
Cell Diameter	10 μm	10 μm	10 μm
Dwell Time (t_{dwell})	200 μs	50 μs	50 μs
Ions/Dwell (N_{ions})	1997.3	514.9	514.9
Beam Current (I_{beam})	3.2 pA	3.3 pA	3.3 pA
Scan Window	10 $\times$ 10 μm	10 $\times$ 10 μm	15 $\times$ 15 μm
Points per Scan	286 $\times$ 286	286 $\times$ 286	429 $\times$ 429
Beam Step	35 nm	35 nm	35 nm
Beam Width	41 nm	35 nm	35 nm
Total Time per Scan	17.0 s	5.6 s	10.5 s
Fluence per Dwell	1.19×10^{14}	4.2×10^{13}	4.2×10^{13}
	ions/cm^2	ions/cm^{2}2	ions/cm^2
Avg. Fluence per	1.63×10^{14}	4.2×10^{13}	4.2×10^{13}
Scan	ions/cm^2	ions/cm^2	ions/cm^2

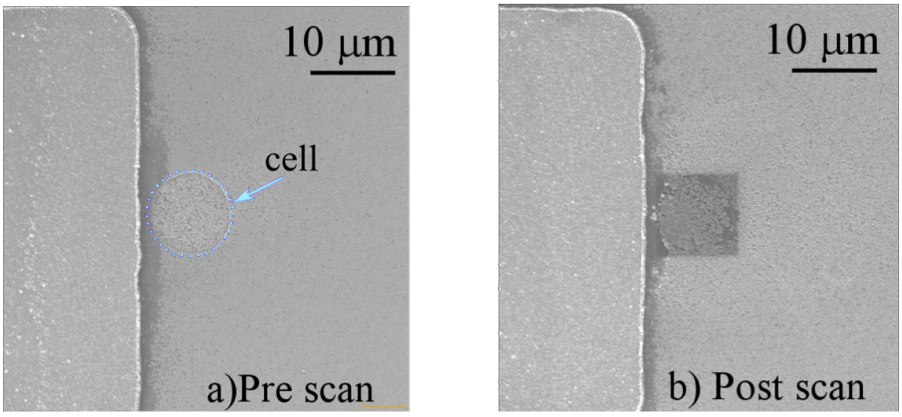

Figure 4.11: SEM micrographs of 10 μm devices (a) prior to ion scan and (b) after exposure to 200 keV Si^{2+} ion scans. A darkening caused by surface etching is observed after exposure. The offset Al contact is shown to the left of the cell in each image.

exposure. The N_{ions} ions per dwell, as listed in Table 4.3, were calculated from the specified dwell time t_{dwell}, the current I_{beam} of the ion beam, and the charge of the Si ion qz_{Si} using the following relationship,

$$N_{ions} = \frac{I_{beam} t_{dwell}}{qz_{Si}}. \tag{4.3}$$

The scan window is user defined and was kept at the limit of the device size, as evident in Fig. 4.11 by the darkening around the device. For device 3, the scan window was increased slightly to determine if a response could be observed when the beam was not directly on the device. No resistance drop was observed when the beam scanned outside of the device. The beam width varied between device tests, resulting in a 41 nm width for device 1 instead of the approximate 35 nm $\times$ 35 nm beam obtained for devices 2 and 3. Each device was scanned multiple times to observe cumulative damage effects.

As apparent in Fig. 4.12–4.14, the resistance state of each device starts at a high resistance state and is then observed to decrease in resistance during the scan. Once one scan is completed, another scan is started immediately afterward. Sudden

drops in resistance were observed to occur at approximately the same location on the device each scan. Each raster scan was performed identically, allowing equivalent time points to be associated with a position on the device. Changes occurring within the same time frame suggest that the devices may have areas that are more sensitive to displacement damage effects than others. The scans were halted once the resistance state of the device began to saturate, shown prominently in Fig. 4.12 and to a lesser extent in Fig. 4.13 and Fig. 4.14. During preliminary testing, it was observed that the CBRAM cells could be erased to near the original HRS after exposure to one or two scans. However, after several scans, once the resistance state began to saturate, the devices could no longer be fully erased. The devices became locked into a low resistance state. The devices featured in Fig. 4.12–4.14 were not erased between scans. The fluence was selected such that the resistance state decreased during each beam scan. The initial resistance state along with the final resistance state of each scan was extracted and plotted in Fig. 4.15 versus ion fluence. The final resistive state of each scan was shown to decrease gradually, similar to the response seen of the HRS devices in 4.7.

Though the transition between resistive states looks abrupt in Fig. 4.12–4.14, when zoomed into the first transition time-frame, the resistance decrease is shown to take place over several hundred microseconds. For device 1, the dwell time of the beam was 200 μs. Fig. 4.16 shows that the resistance decrease happens over 400 ms starting at approximately 2.4 seconds into each scan. The time frame of the drop corresponds to a 10 μm $\times$ 245 nm section of the device, as calculated using t_{dwell}, Points per Scan, and Beam Step listed in Table 4.3. The consistency of the resistance drop suggests that this region may contain a residual filament or a material defect that allows this region to be more sensitive to heavy ions. The mean projected lateral scatter of the Si-ion within the chalcogenide layer is 66.6 $\pm$ 49.5 nm. Given the

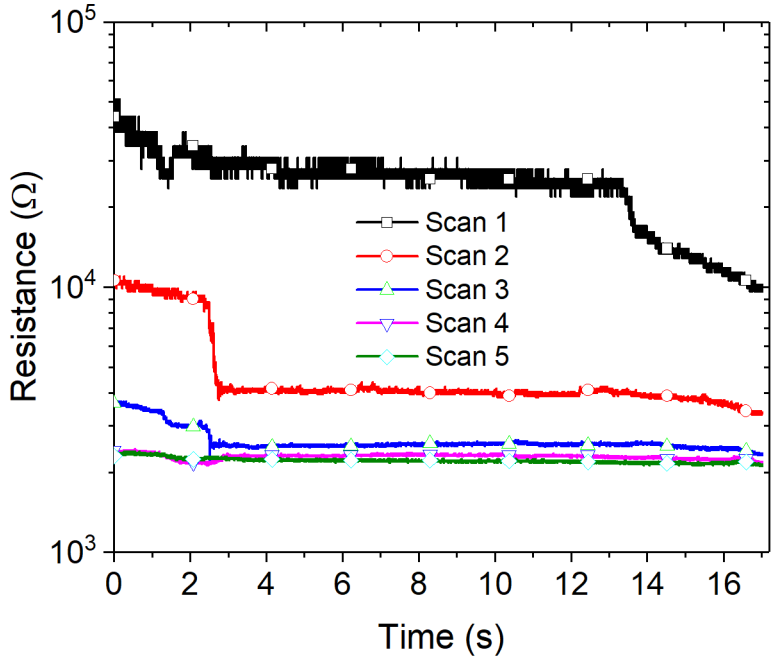

Figure 4.12: The resistance state of device 1 is observed to decrease each scan, eventually saturating at an LRS. The resistance is shown to decrease abruptly at approximately the same time each scan.

continuous response over the entire 10 μm distance across the device, the observed behavior may have a time component to it in addition to a positional dependence.

Fig. 4.17 shows the highlighted respond of device 2. Like in Fig. 4.16, Fig. 4.17 shows that device 2 also had changes in resistive state at correlated points during each ion beam scan. For device 2, the highlighted region shows that state changes did not always result in a decrease in resistive state. All scans, except for scan one, showed a decrease in resistance followed by a recovery back to the state prior to the decrease. Device 2 had a second correlated response at 3.6 s into each scan, where the resistive state consistently decreased each scan. Assuming that the two types of responses are the result of the same mechanism, the heavy ions could either be causing a generation and separation of carriers or creating vacancies that results in the migration of Ag^+. In one case, the Ag-ions begin to move (generating a current) but fail to reduce on

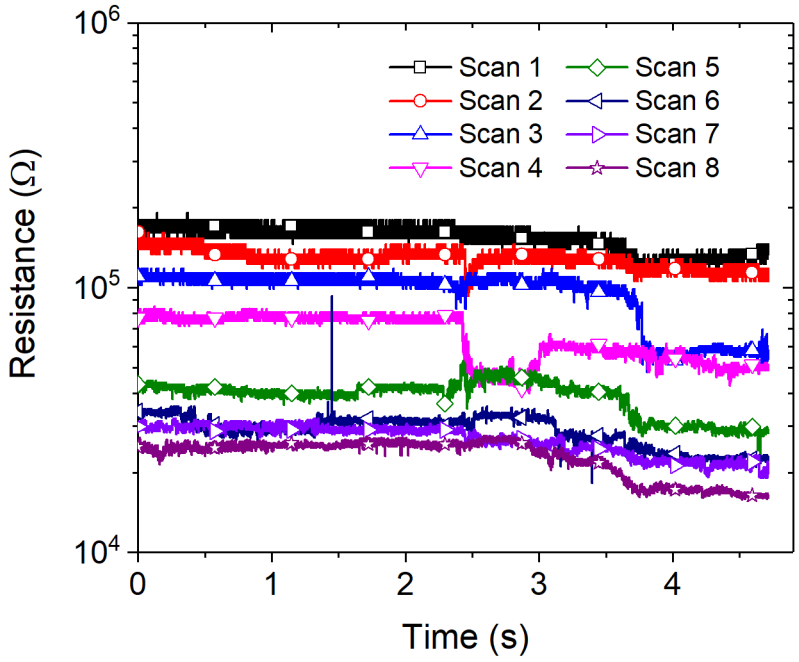

Figure 4.13: The resistance state of device 2 during each 200 keV Si-ion beam scan.

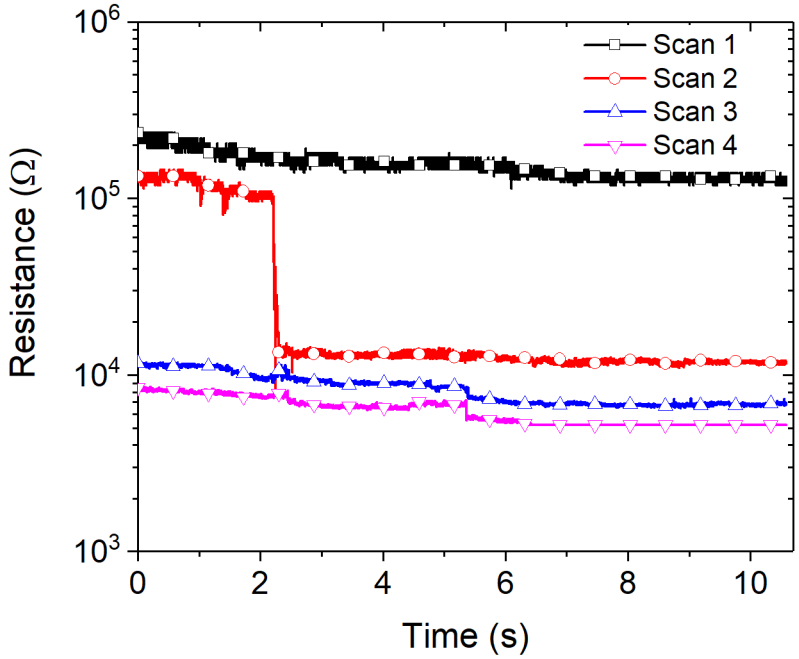

Figure 4.14: The resistance state of device 3 during each 200 keV Si-ion beam scan. The resistance is shown to decrease abruptly at approximately the same time each scan.

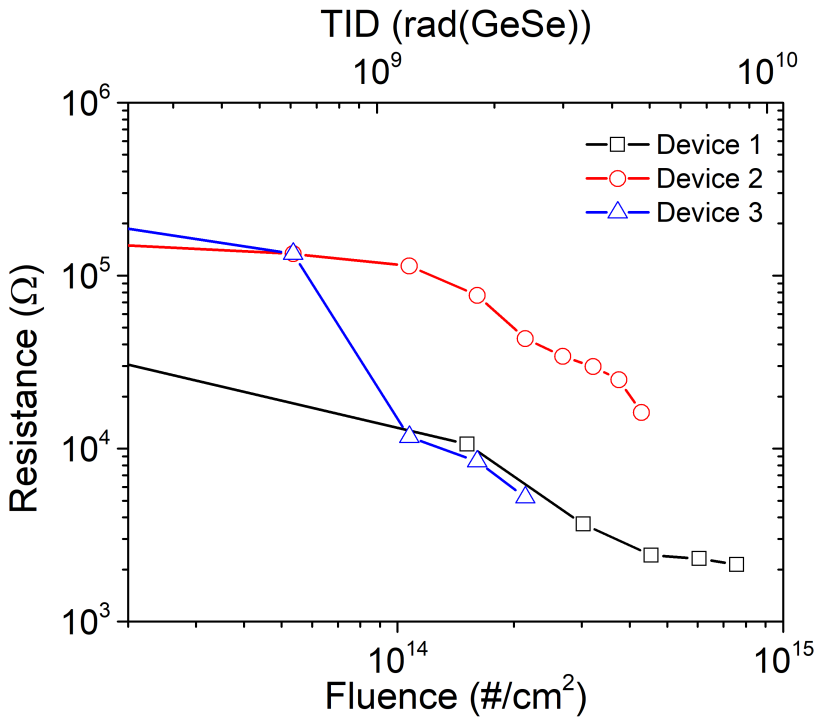

Figure 4.15: Final resistive state of CBRAM devices after each ion beam scan.

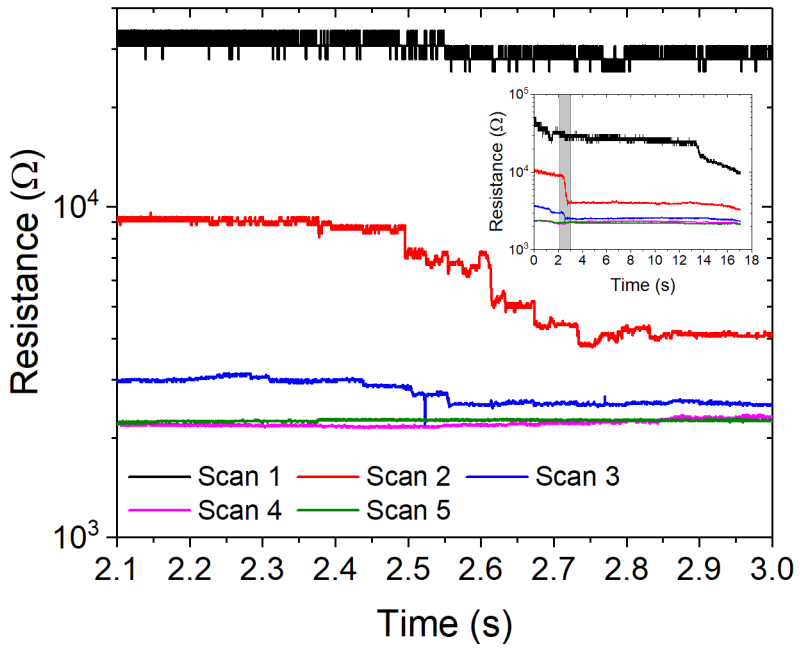

Figure 4.16: Device 1 resistance change over time for the region highlighted by the inset graph.

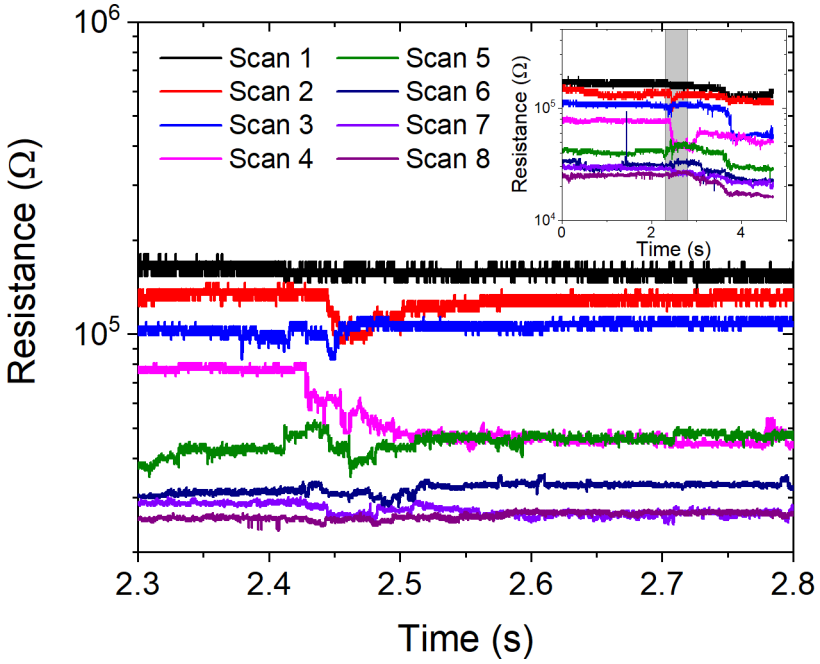

Figure 4.17: Device 2 resistance change over time for the region highlighted by the inset graph.

the filament and in the other cause, the Ag reduces on the existing filament structure, reducing the overall resistance.

From the SRIM results shown in Fig. 4.5, calculations estimate a total of 2640 vacancies/ion throughout the full device with 1164 vacancies/ion in the electrolyte layer. The number of vacancies generated per dwell in the electrolyte is therefore in the order of 2×10^6 (1.4×10^{17} vacancies/cm^2) for device 1 and 6×10^5 (4.9×10^{16} vacancies/cm^2) for devices 2 and 3. The actual amount of damage is much lower than the calculated, as the calculation does not take into consideration annealing at room temperature.

4.4 Total Ionizing Dose

4.4.1 Experiment Setup

TID experiments were performed at Sandia National Laboratories at the Gamma Irradiation Facility (GIF). The GIF has several dry-cell concrete rooms each with a ^{60}Co source array and a variety of dose rates. The cells are several square meters, allowing for the exposure rate to be controlled by varying the distance from the source.

The devices used for ^{60}Co irradiation were the crossbar structures described in Chapter 2. Three chips were packaged using 40 pin CDIP packages. Each chip contains 32 devices with 20 devices accessible. The devices were DC cycled five times in the manner described in Chapter 3 using an Agilent B1500 parameter analyzer to verify device functionality. The package for irradiation was placed onto a test board that allowed each pin to be accessed with a ribbon cable connection. Two thermoluminescent dosimeters (CaF_2 TLD) were placed on either side of the device package, as shown in Fig. 4.18 and one the back of the test board behind the device area. The device package on the test board was placed against a heat sync inside a polypropylene box. A thermocouple was attached to the heat sync to monitor the device temperature during irradiation. Building air supply was blown through the box to regulate the device temperature. The packaged devices were accessible using ribbon cables. The plastic box was placed inside a Pb-Al box to shield the devices from scattered low energy electrons. The enclosure was suspended between two stands and oriented such that the back-side of the board faced the pool containing the ^{60}Co source. The stands were placed as close to the source as possible to achieve a high dose rate. The dose rate inside the enclosure was measured at 475 rad(Si)/s or 415 rad($Ag_5Ge_3Se_7$)/s. A picture of the text fixture is shown in Fig. 4.19.

Two separate irradiations were performed. One package was irradiated to 22.8

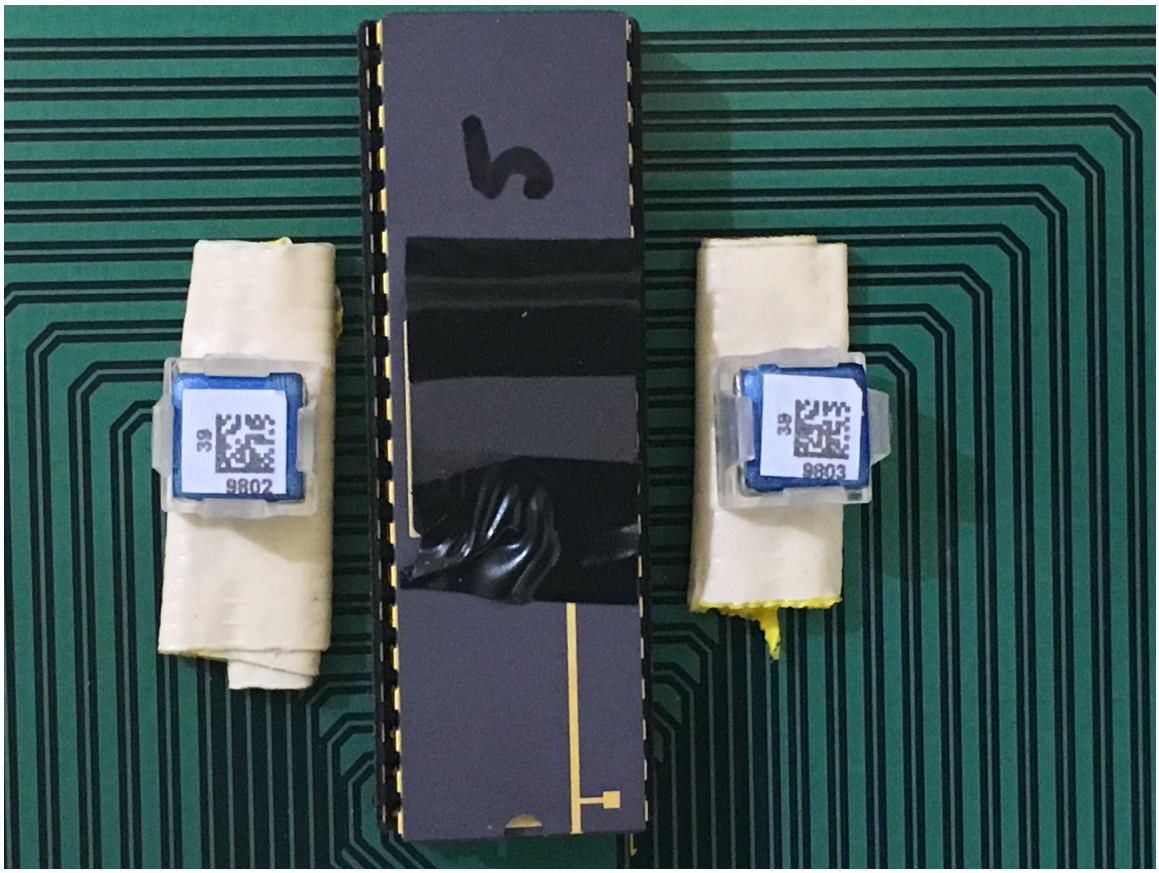

Figure 4.18: 40 pin CDIP containing wire-bonded CBRAM tile. A TLD was placed on each side of the package and one behind the device area on the backside of the board (not shown).

Mrad($Ag_5Ge_3Se_7$) and the second was irradiated to 23.9 Mrad($Ag_5Ge_3Se_7$). The first package had two devices erased to an HRS and two devices set to an LRS using a 25μA current compliance. The second package had three devices set to an HRS and five set to the LRS. One package was used as a control outside of the radiation chamber and tested at room temperature. Three control devices were used, one in the HRS and two set to the LRS.

The configuration used to monitor both the irradiated devices and control devices is shown in Fig. 4.20. The devices inside the irradiation chamber were individually accessed using two 60 ft ribbon cables connected to a printed circuit board (PCB) that converted the ribbon cable connections to BNC coaxial connections. Coaxial cables

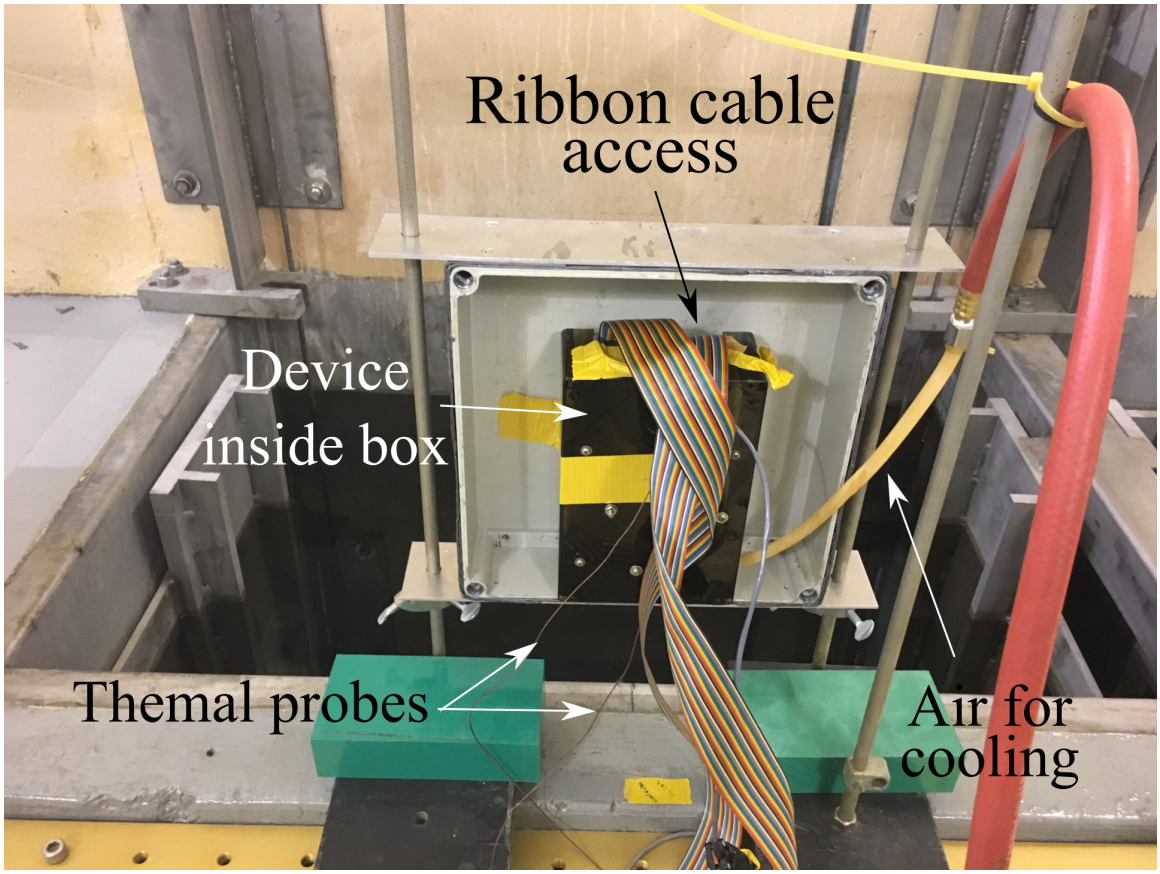

Figure 4.19: Assembly used to test CBRAM during ^{60}Co irradiation. The PCB containing the device package was placed against a heat sync inside a plastic box. A thermocouple was attached to the heat sync to monitor the device temperature during irradiation. Building air supply was blown through the box to regulate temperature. Packaged devices were accessible using ribbon cables. The plastic box was placed inside a Pb-Al box (box cover not shown).

were connected from the PCB to individual inputs of a Yokogawa DL850 oscilloscope. During testing, a 50 mV read bias was applied to the circuit in Fig. 4.20. During irradiation, the resistance state of the irradiated and control devices were monitored continuously for the duration of the test.

4.4.2 Observed Effects

Ion irradiations result in a combined environment characterized by both ionizing and nonionizing energy loss. Separating effects due purely to TID versus displacement

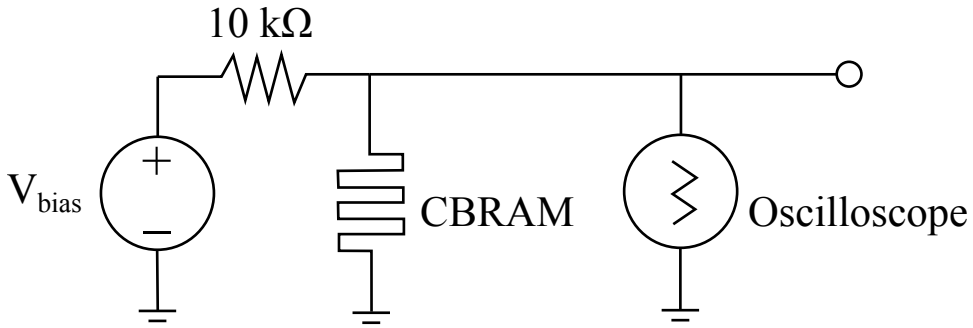

Figure 4.20: Circuit configuration used to actively monitor CBRAM devices during ^{60}Co irradiation.

damage is a tricky process unless the mechanism responsible for the observed failures is known. To examine the potential for TID effects, γ-ray testing using ^{60}Co was performed up to 23.9 Mrad($Ge_{30}Se_{70}$). Fig. 4.21 shows the *in situ* response of the seven devices programmed to an LRS and the 5 devices programmed to HRS. Throughout the 16-hour exposure, several devices did drift from their initial resistance state, but all devices maintained their relative binary state (no switch from HRS or LRS or vice versa). One HRS device, shown as the red curve, did drift toward the LRS state, but did not experience a sudden transition, such as those observed during ion testing. This HRS device also started in a lower than typical HRS state, most likely due to a partially formed filament. The control devices are shown to be very stable and experienced very little drift during the duration of the test.

The second irradiated package had ten devices that were DC cycled pre and post irradiation. Of those ten, eight of them were used for retention testing and the remain two were bias but not monitored due to limitations on the number of oscilloscope inputs. The HRS and LRS distribution of the DC sweeps pre and post irradiation is shown in Fig. 4.22. Each device was cycled 5 times pre and post irradiation for a total of 50 points to construct the cumulative distribution function (CDF). Fig. 4.22 shows that post the 24 Mrad($Ge_{30}Se_{70}$) irradiation, the HRS distribution decreases and overlaps with the LRS distribution. The LRS distribution is also observed to

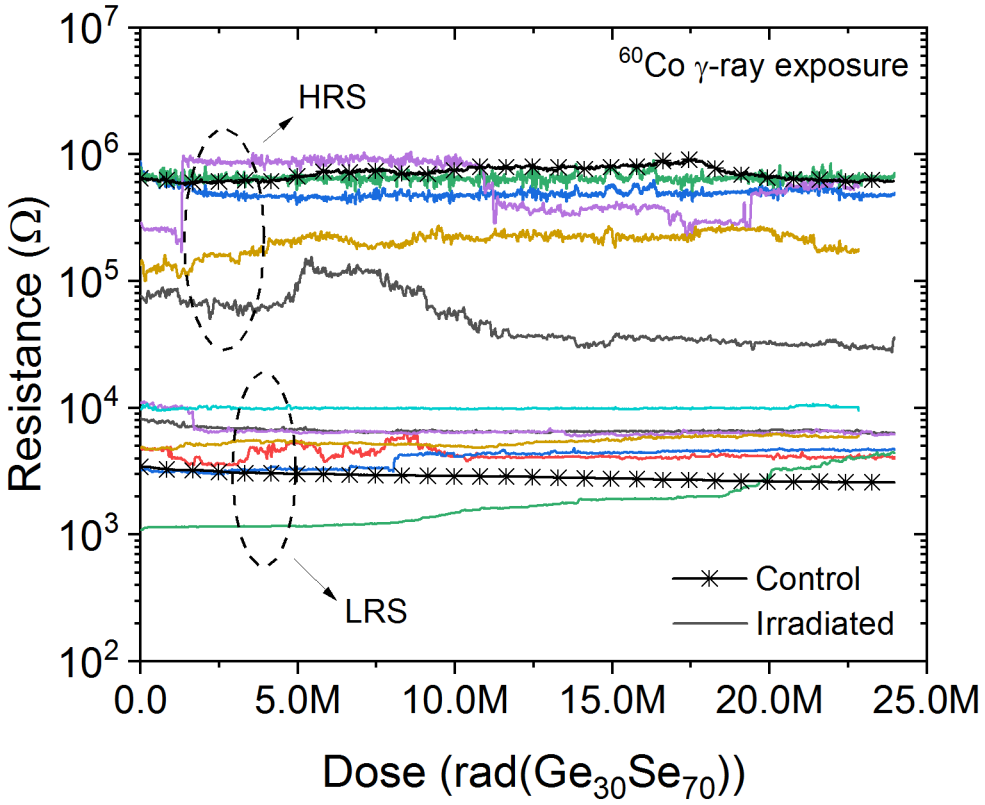

Figure 4.21: Retention of programmed resistances up to a TID of 23.9 Mrad ($Ge_{30}Se_{70}$).

broaden slightly and had one device with an LRS state that overlapped with the HRS distribution.

The CDF plot is useful for evaluating the population of CBRAM devices assuming that each device is equivalent in behavior. However, since the association of HRS to LRS of individual devices is lost in a CDF distribution, it is necessary to examine each device's behavior using the box plot shown in Fig. 4.23. Fig. 4.23 shows the distribution of the HRS/LRS programming window ratio for the ten devices tested during the 23.9 Mrad exposure. The box region marks the 25 percentile to 75 percentile of the distribution while the whiskers are used to mark the minimum and maximum of the distribution. Six of the ten devices are shown to have a tighter distribution of

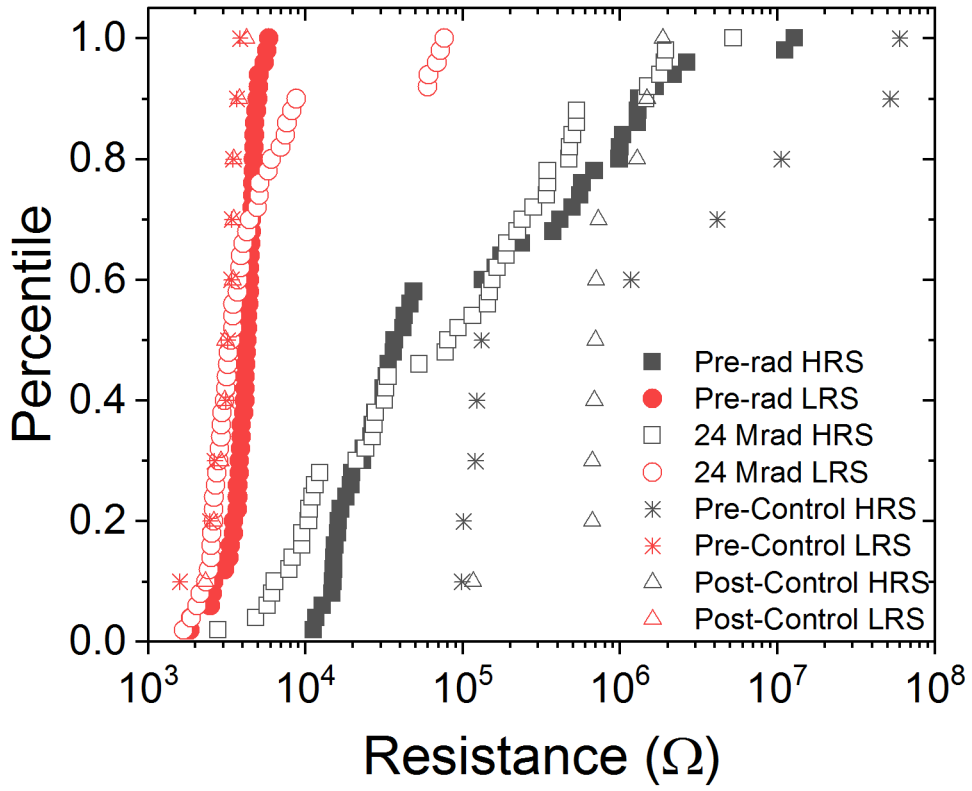

Figure 4.22: Cumulative distribution of LRS and HRS pre and post ^{60}Co irradiation.

HRS/LRS values following irradiation as compared to their pre-radiation distribution. Devices 4 and 10 are shown to I-V sweeps where the programming window had collapsed (HRS/LRS = 1).

Though some drift in DC characteristics is noted post irradiation, there is no clear evidence, given the behavior of the control devices, that these effects are a result of TID. Testing beyond 23.9 Mrad($Ge_{30}Se_{70}$) was not possible due to time constraints. Though the predicted TID threshold is 30.1 Mrad, three of the devices bombarded with ions experienced failure below 20 Mrad, as depicted in Fig. 4.9. Given that no devices irradiated with ^{60}Co failed during retention testing, either TID is not the sole contributer to changes seen during heavy ion testing or further TID testing beyond 30 Mrad is necessary to require a drastic state failure.

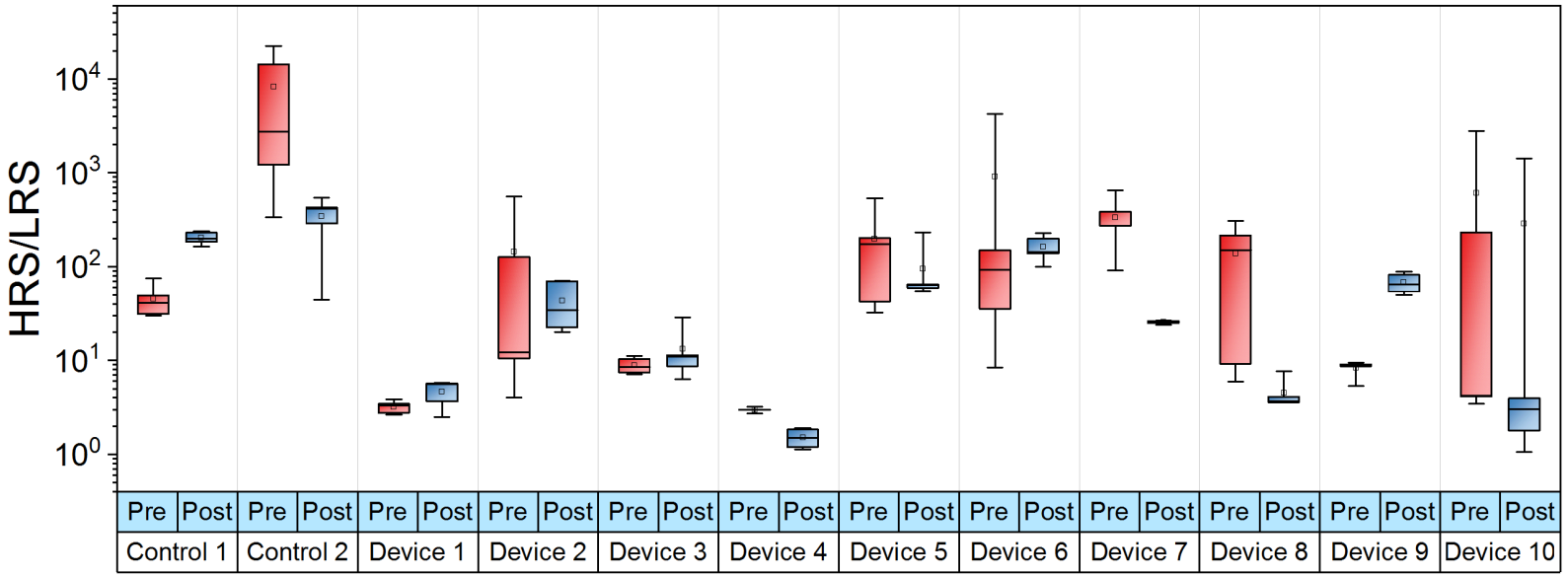

Figure 4.23: HRS/LRS ratio distributions of CBRAM pre and post irradiation. Red boxes represent the 25-75 percentile distribution of HRS/LRS prior to irradiation while the blue boxes represent the HRS/LRS after a TID of 24 Mrad($Ge_{30}Se_{70}$). Open square marks the mean of the distribution and the whiskers mark the lowest and highest values.

Chapter 5

EFFECTS OF RADIATION ON DC CYCLING

5.1 Introduction

In most applications, solid-state memory is programmed using a pulse instead of a gradual DC sweep. DC testing is performed as a tool for evaluating how the individual device parameters evolve, such as the HRS, LRS, and programming threshold. DC programming involves growing and dissolving a filament within a longer timeframe than performing pulsed programming since the applied electric field is gradually stepped over time. The relatively gradual programming provides ample time for cation resupply to occur in the electrolyte around the growing filament [23]. As such, DC testing on irradiated devices is useful for determining how radiation affect the electrolyte layer and its ability to facilitate the transport of Ag^+ to the region of the developing filament. Prior works have evaluated the behavior of the cycled HRS and LRS distributions after several TID steps. Selenide based CBRAM was found to be ^{60}Co ionizing radiation tolerant up to 10 Mrad($Ge_{30}Se_{70}$), with no significant changes to the LRS or HRS during DC cycling [32]. Another test evaluated the LRS and HRS response to 100 keV electrons up to a dose of 12 Mrad($Ag_5Ge_3Se_7$) with no obvious effects due to TID [40]. That same study also presented the response to 9.48×10^{12} p/cm^2 50 MeV protons (1.1 Mrad($Ag_5Ge_3Se_7$)). No significant change in LRS or HRS distributions were observed for front-side irradiation, though a decrease in the HRS distribution was measured after backside (through Si wafer) irradiation [40]. With the current evidence that Ag-$Ge_{30}Se_{70}$ CBRAM is TID hard, it was decided to evaluate the DC response to displacement damage effects.

In the following experiments, CBRAM devices were exposed to 14 MeV neutron while measuring the DC characteristics at several fluence steps. The following tests show a reduction of the HRS/LRS window with increasing fluence. This neutron work was first presented in [35], [41]. The following work also presents heavy ion tests that were also performed using 200 keV Si-ions. In these tests, the HRS/LRS windows was also shown to collapse after a significant fluence of ions.

5.2 14 MeV Neutron Exposure

5.2.1 Experiment Setup

Neutron irradiations were performed at Cobham RAD Solutions in Colorado Springs, CO using a 14.1 MeV deuterium-tritium reaction neutron generator. Two die, each containing 32 individually accessible CBRAM cells, were mounted and wire bonded into ceramic dual in-line packages (CDIP). A total of five cells were available for *in situ* testing on one die and three cells were available on a second die. The second package was used for the control. Control devices were not exposed to neutrons and were tested in a room temperature laboratory environment. Ceramic lids were taped across each package opening to protect the CBRAM from ambient light exposure [26]. Prior to irradiation, a niobium foil was taped across the lid of the package. An Aloka dosimeter mounted inside the radiation chamber was used for active dosimetry. The test board was mounted to a tripod and placed against the end of the neutron generator beam plate to ensure that the CBRAM received the highest possible neutron flux, as shown in Fig. 5.1. The CBRAM cells were accessible via ribbon cables that ran from the test board inside the chamber to a switch board outside of the chamber. The switch board allowed each CBRAM cell to be individually accessed and tested using an Agilent 4156A parameter analyzer.

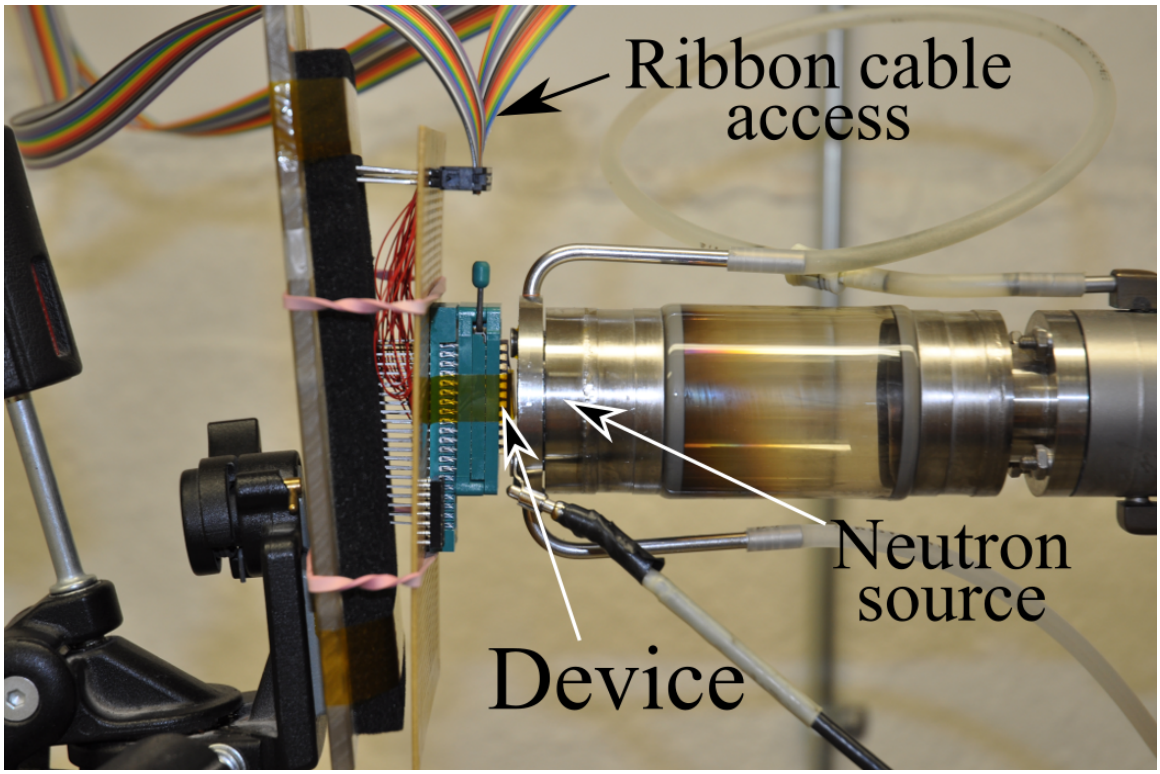

Figure 5.1: Packaged device placed against neutron generator plate for maximum neutron flux. CBRAM was accessible via ribbon cable during exposure.

Prior to irradiation, each device was cycled five times using a DC staircase sweep to verify their functionality. The devices were swept in the manner described in Chapter 3. A programming compliance current of 100 μA was used for all eight devices. The I-V curve shown in Fig. 5.2 is characteristic of the CBRAM cells tested. The devices were erased and left in a high resistance state during exposure.

The devices were irradiated with a mean 14 MeV neutron flux of 2.18×10^{9} n/cm^2·s. During irradiation the anode and cathode terminals were biased to ground. The devices were periodically cycled by DC sweeping each device five times in the manner previously stated. The HRS and LRS of each device was extracted from the I-V curve at the 30 mV voltage point. The read voltage was selected such that it was conservatively smaller than the programming threshold of 100 mV. The CBRAM was exposed to a total 14 MeV neutron fluence of 3.19×10^{13} n/cm^2 (5.65×10^{13} n/cm^2 1

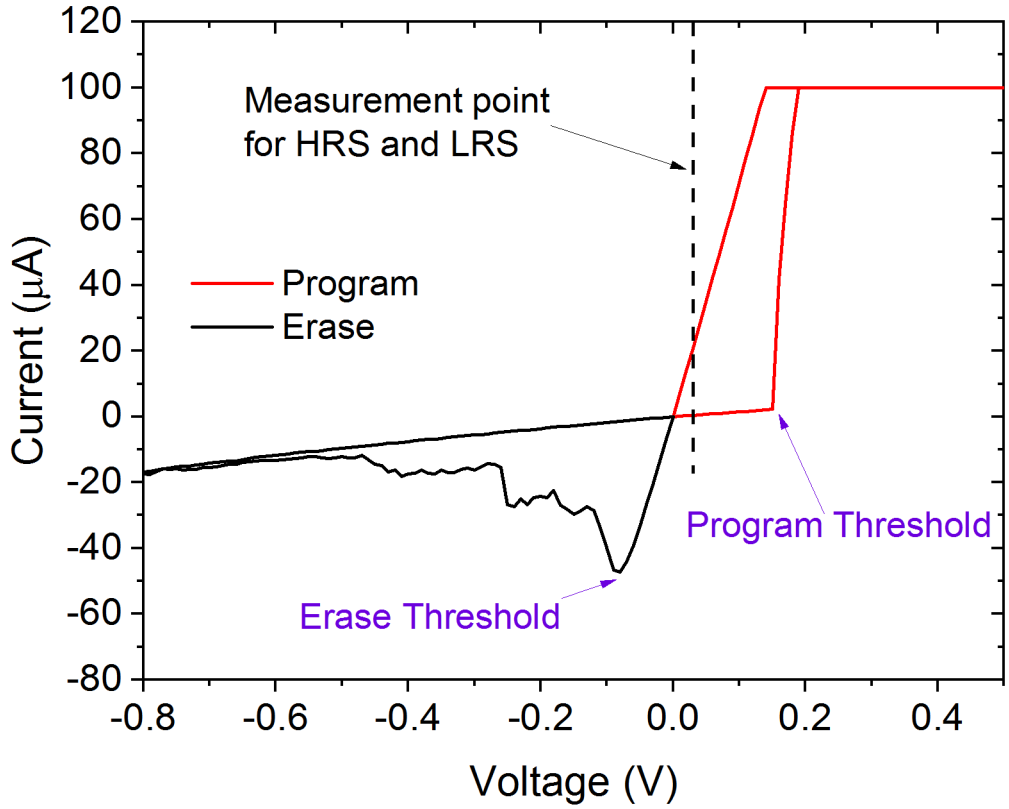

Figure 5.2: I-V curve of a CBRAM cell with a 100 μA programming compliance. The window between the HRS and LRS (low current and high current) is the triangular like opening in the programming curve. State sampling is typically taken as the 30 mV point.

MeV Si equivalent).

The control devices were tested with the same procedure and in equivalent time steps as the exposed devices. Packaged control devices were tested in an Agilent 16442B Test Fixture to access the package pins.

5.2.2 Observed Effects

The resistance states depicted in Fig. 5.3 through Fig. 5.5 were measured by DC cycling each device five times at each fluence step. The resistive states were sampled from the I-V curve at 30 mV, as marked in Fig. 5.2. The following data shows that

the programming window of each CBRAM cell collapses due to neutron exposure. When a device fails, it becomes trapped either in an HRS or an LRS and is unable to be programmed or erased respectively. Fig. 5.3 shows how the HRS/LRS window was observed to decrease, with the HRS eventually becoming indistinguishable from the LRS. Fig. 5.4 shows a case where the HRS/LRS window collapsed to a higher resistance state. The HRS/LRS programming window of devices 4 and 5 in Fig. 5.5 are shown to fluctuate before collapsing at fluences above 2×10^{13} n/cm^2. The control devices in Fig. 5.3 through Fig. 5.5, show how the CBRAM devices are expected to maintain a window between the LRS and HRS under nominal conditions. The behavior of the control devices highlight the unexpected collapse of the window between the LRS and HRS of the irradiated devices. The first notable convergence occurred after a fluence of 4.90×10^{12} n/cm^2 and was first measured at 1.47×10^{13} n/cm^2. Three of the five devices programmed with 100 μA maintained a separation between LRS and HRS up to a fluence of 2.93×10^{13} n/cm^2 before collapsing. All devices exhibited a steady decrease in the HRS/LRS window beyond a fluence of 1.47×10^{13} n/cm^2.

The box plots in Fig. 5.6 show the distribution of the HRS/LRS ratio with each fluence step. Each box contains the distribution of the five DC sweeps for all five devices, resulting in 25 data points per box. The mean HRS/LRS is 15, prior to irradiation. As the neutron fluence increased, the mean HRS/LRS ratio decreased until it collapsed to 1 (no programming window). Variation in device performance increased after a fluence of 4.90×10^{12} n/cm^2 resulting in a wide spread of HRS/LRS window values. All irradiated devices experienced a full convergence of the HRS/LRS window by the conclusion of the 3.19×10^{13} n/cm^2 exposure. The TID receive during testing was 35.1 krad($Ag_5Ge_3Se_7$). Given that no effects due to TID have been observed below 10 Mrad($Ag_5Ge_3Se_7$), the effects observed during neutron irradiation

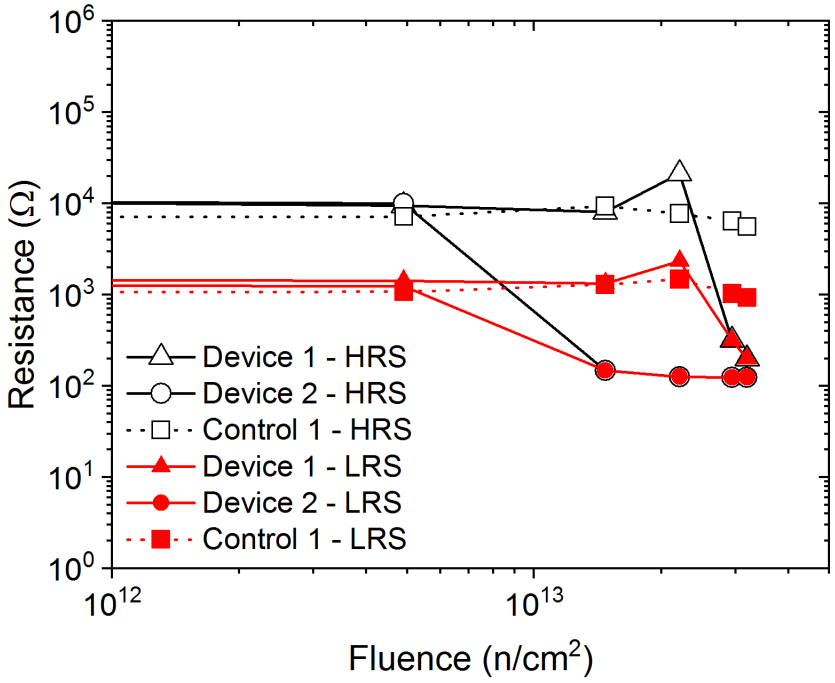

Figure 5.3: Mean HRS and LRS versus neutron fluence for CBRAM devices 1 and 2.

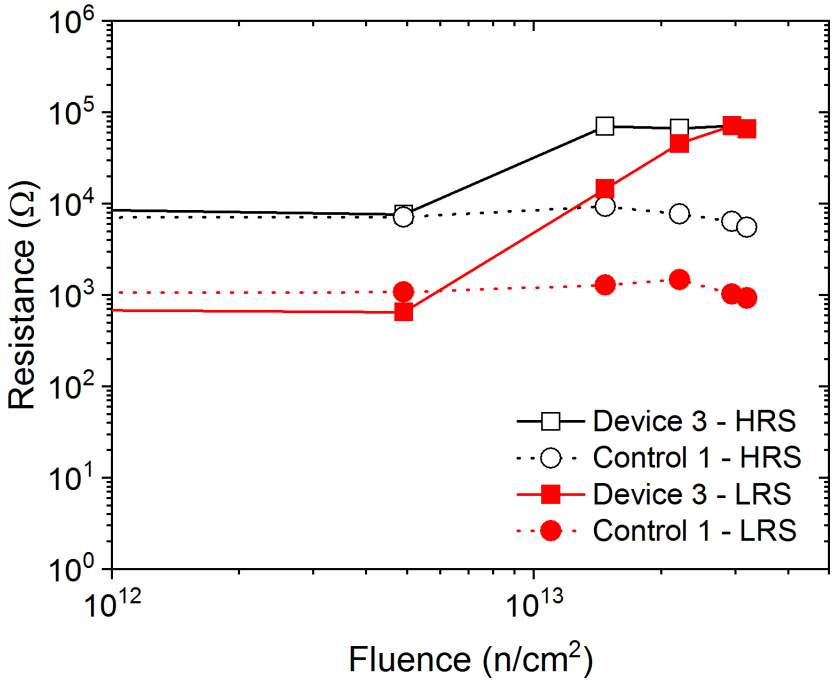

Figure 5.4: Mean HRS and LRS for CBRAM device 3 versus neutron fluence.

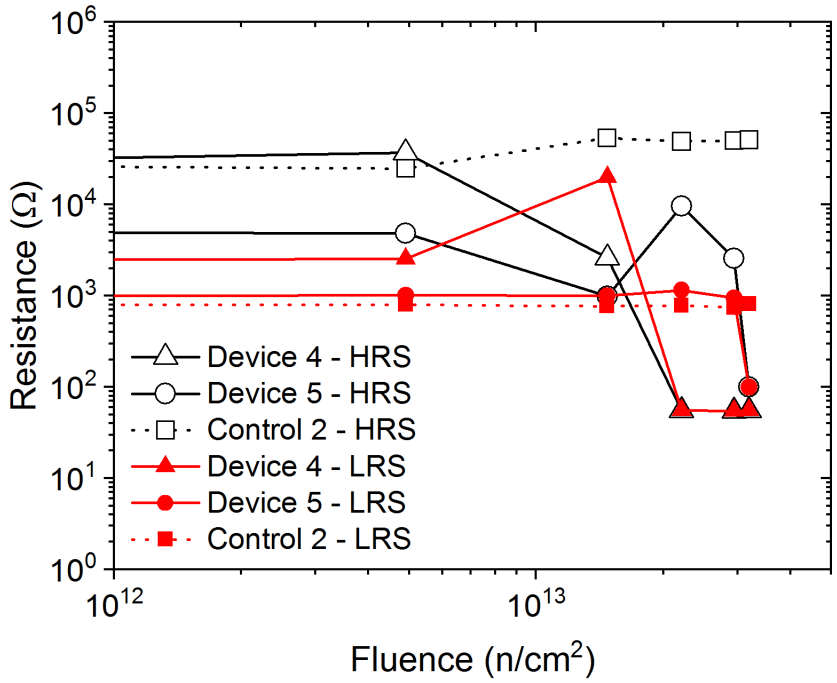

Figure 5.5: Mean HRS and LRS versus neutron fluence for CBRAM devices 4 and 5, that became unstable before collapsing.

are most likely due to displacement damage [32], [33]. An erase sweep from 0 V to -3 V was applied to each device in an attempt to recover their original HRS. The device states remained fixed, i.e., not switchable after performing the erase sweep, with no observable difference between the LRS and HRS. For the devices that failed to the HRS, no programming threshold was observed during DC cycling, meaning that no evidence of filament growth was observed.

The cumulative distribution of the HRS and LRS are depicted in Fig. 5.7 and Fig. 5.8 respectively. These data show a clear trend in the decrease of both the HRS and LRS with increasing neutron fluence. The initial LRS starts off around 1.7 kΩ. Even after the first fluence step of 4.9×10^{12} n/cm^2, the HRS distribution is shown to drift into the LRS region. The LRS distribution also experiences as decrease in the majority of the measured resistive states, with the full LRS region spanning from

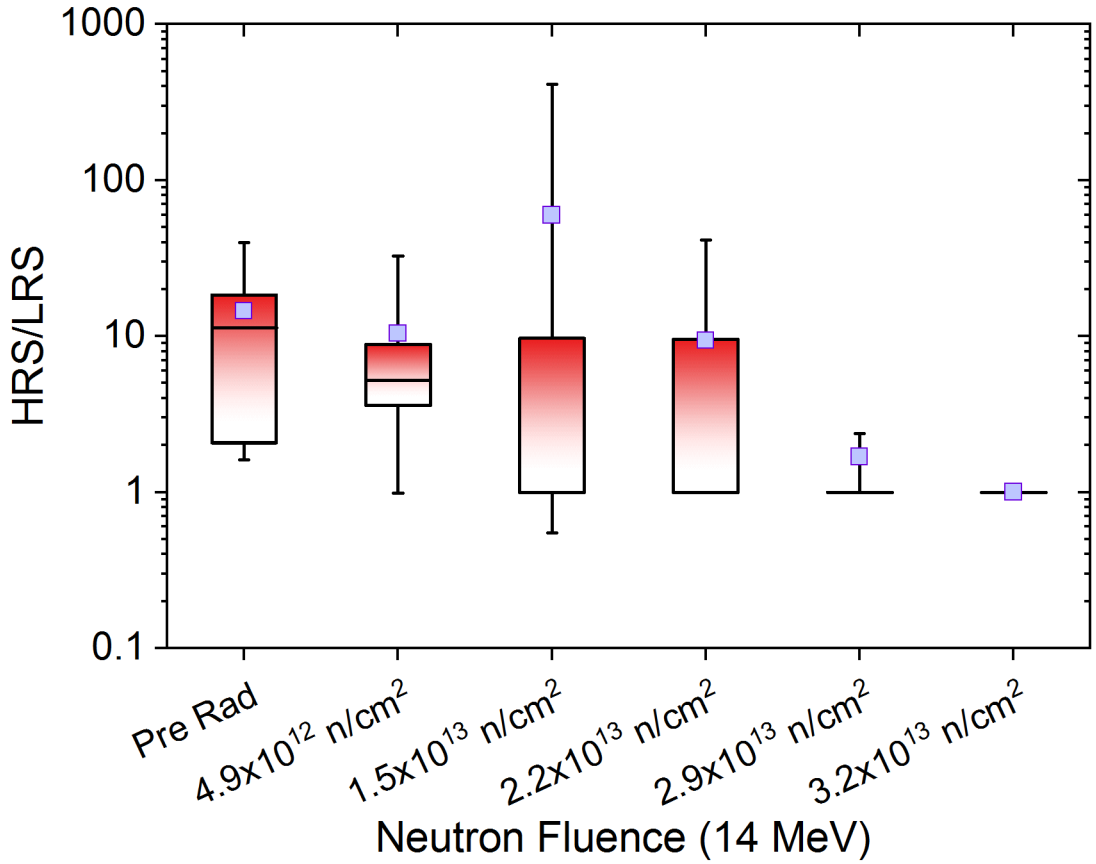

Figure 5.6: Box plot showing the HRS/LRS window collapsing at high neutron fluence. Bottom and top edge of each box represents the 25th and 75th percentile distributions respectively, box whiskers span the 5th to 95th percentile, and the small blue squares mark the mean of the distributions.

tens of Ohm to 100 kΩ.

The devices exposed to 14 MeV mono-energetic neutrons exhibited a measurable effect due to displacement damage after approximately 10^{13} n/cm^2 with complete failure occurring at 3.19×10^{13} n/cm^2. This result is slightly surprising given that no correlation to displacement damage was distinguishable during retention testing, as discussed in Chapter 4. This suggests that for the materials used in CBRAM, ionizing radiation may partially counteract the effects of displacement damage. This would be consistent with the results reported in previous TID studies on similar devices,

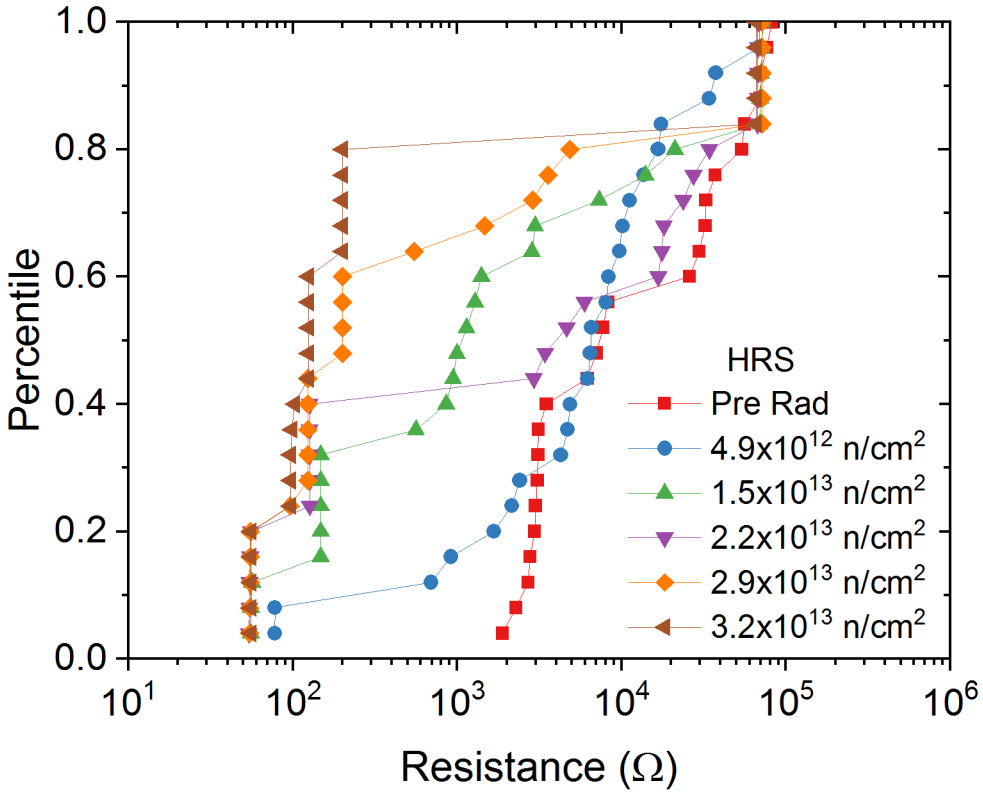

Figure 5.7: Cumulative distribution of the high resistance states of the five devices programmed with 100 μA compliance current.

which have shown that CBRAM performance can be improved in an ionizing radiation environment [32].

The collapse of the HRS/LRS window may be due to structural changes that are occurring in the glass layer. Electrochemical metallization memories rely on the porosity of the chalcogenide glass layer to allow hoping of the active metal ions through the glass via the coordinated motion of ions [15], [42]. Photo-doping the chalcogenide glass with an active metal such as Ag, creates a solid electrolyte that helps to facilitate the movement of the metal ions and provides stability to a formed conductive filament [27], [42]. It has been observed that the Ag photo-doped into the GeSe glass does not homogeneously distribute throughout the material. The Ag is observed to

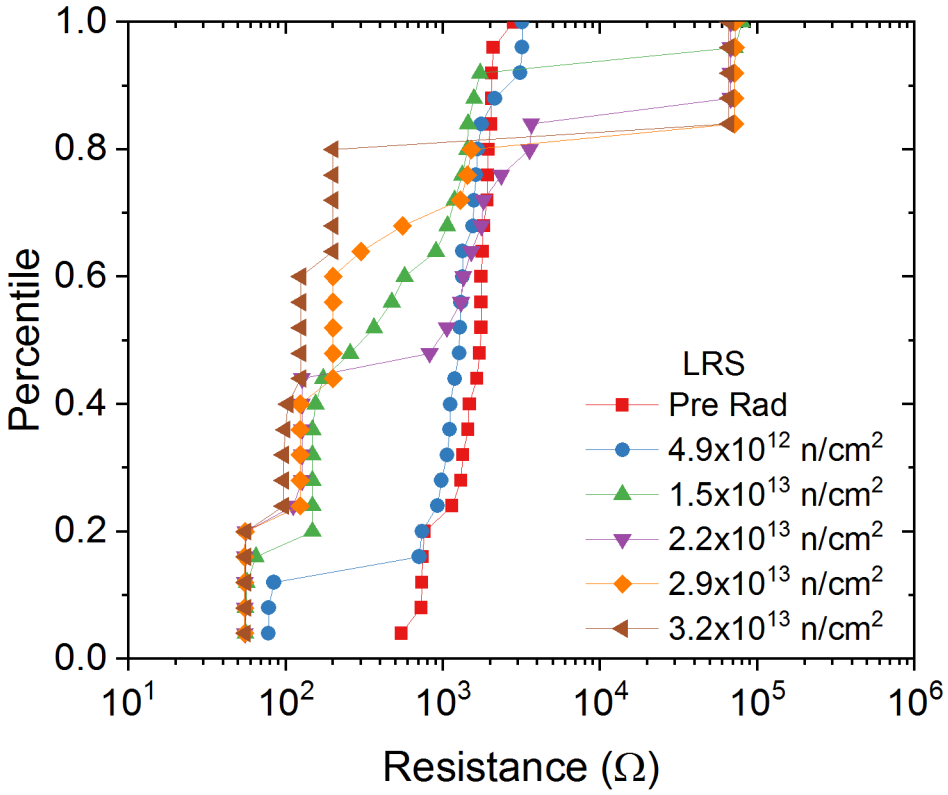

Figure 5.8: Cumulative distribution of the low resistance states of the five devices programmed with 100 μA compliance current.

nucleate in Ag rich regions, creating an isotropic mixture of Ag rich and Ag poor/Ge rich regions [43], [19], and [44]. The Ag rich regions are typically in the order of 2 nm in diameter with less than 1 nm of Ag-poor interstitial glass between them [43]. These Ag rich regions may act as reduction sites for mobile Ag^+ ions that obtain excess electrons, though on average these sites will be neutral [19]. The formation of the conductive filament should then be thought of as a joining of multiple nanoscale filaments forming a continuous path between the cathode and anode.

When the device is in the HRS, the majority of the mobile Ag ions have returned to the anode contact and enough breaks in the conductive path have occurred to greatly limit conduction. Displacement damage may in some way reduce the ion mobility

through the electrolyte. The Ag-$Ge_{30}Se_{70}$ material system is a disordered glass with a variety of evolving bond formations at room temperature [44], [45], [46]. The localized variation in material structure creates potential barriers of different heights and thicknesses that the Ag^+ ions must hop over to migrate through the electrolyte [47], [48]. The inability to erase or further program the device to a lower resistance state suggests that displacement damage effects have greatly inhibited the mobility of Ag^+ ions. Material changes may have occurred that resulted in an increase in potential barrier heights, deterring the cations from hopping to the next site. Localized Ag_2Se formation or a redistribution of the glassy structure may result in a deepening of the potential wells occupied by the Ag^+, restricting the mobility of the ions [43], [44].

5.3 100 keV Li-ion Bombardment

5.3.1 Experiment Setup

Heavy ion tests were performed to evaluate how the CBRAM devices behave in combined TID and DD environment. These tests were performed using 5 μm crossbars with devices along the diagonal of the contact array. The device stack is the same as described in Chapter 2 and Chapter 4, where the 350 nm thick Al anode contact bar sits over top of the CBRAM cell. The following tests were performed on the same die as the retention tests presented in Chapter 4 but on different devices in the array. 100 keV Li-ion exposures were performed using the NI at Sandia National Laboratories. The ion bombardment was performed in the same way as described in Chapter 4, where the ion beam was raster scanned across the area of the device. Two devices were used to examine the response of the HRS/LRS programming window. Prior to exposure, each device was DC cycled and erased to the HRS. A 30 mV DC read sweep was used prior to exposure and after each fluence step. Between each

irradiation the device was DC cycled followed by another DC read prior to the next irradiation. A 10^{12} ions/cm^2 fluence step was used for each irradiation up to a total fluence of 3×10^{13} ions/cm^2 or until the device failed to switch. The HRS and LRS were extracted from the I-V curve at the 30 mV point.

5.3.2 Observed Effects

Each device was DC cycled once after each fluence step. During exposure the device was left in the HRS. Fig. 5.9 shows how the HRS/LRS programming window collapsed after a fluence of 10^{13} ions/cm^2. Fig. 5.10 shows the measured HRS and LRS for both devices for each I-V sweep performed. Though both devices were located on the same die, device 1 was capable of switching with an HRS/LRS ratio $10\times$ that of device 2. Since the LRS for a given compliance can be consistently set in room temperature lab condition, as shown by the control devices, the variation in the programming window is typically a result of variance in the HRS [32], [49]. The $10\times$ HRS difference between device 1 and 2 is shown in Fig. 5.10. This HRS variation is typically observed in research quality CBRAM devices.

The gray region of Fig. 5.10 highlights an interesting trend where the HRS and LRS of both devices increased prior to the HRS collapsing to the LRS value (shorted). Fig. 5.11 displays the programming sweeps of both devices during the exposures marked by the gray area. In this region, the ohmic LRS response are shown to become less linear with increasing fluence. The ragged profile of the LRS curve suggests that ion migration is occurring around the filament structure. When a device is programmed with a DC sweep, the applied positive bias initiates the REDOX reaction while the electric field drives the Ag^+ through the electrolyte. In a room temperature lab environment, enough Ag^+ is supplied to allow a stable, near ohmic, filament to form. The non-ohmic response of the curves in Fig. 5.11 suggest that

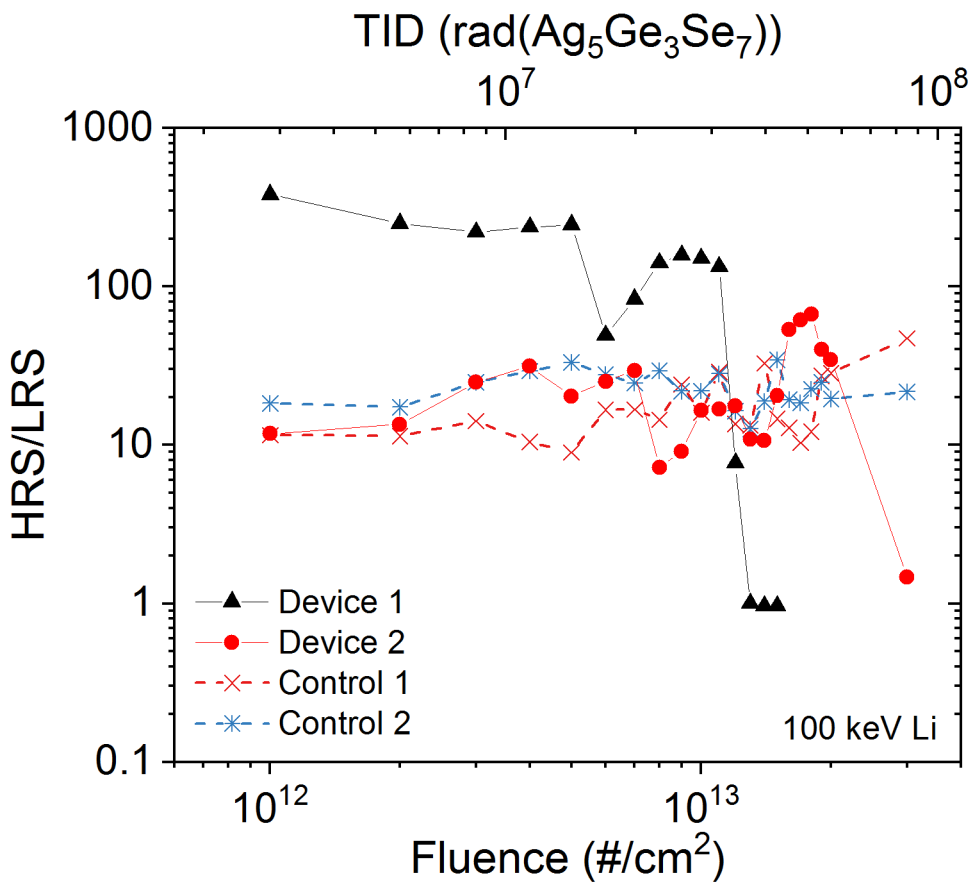

Figure 5.9: HRS/LRS programming ratio for the I-V sweep performed after each 100 keV Li-ion fluence step. Non-irradiated control devices marked by dotted line.

not enough Ag is being supplied to create a robust filament, resulting in a partially dissolved filament [50]. Fig. 5.12 shows the I-V curves for the erase operations corresponding to the programming curves of Fig. 5.11. During the reversed bias, the ohmic response of the LRS can be resolved. The current response has more fluctuation than the linear response of the stronger (lower) LRS recorded prior to the observed radiation effects, though on average it still exhibits a linear trend as marked in Fig. 5.12. The spikes of conductivity are most likely from nucleated Ag that has come into contact with the filament but is then repelled or migrates away from the filament. An insufficient supply of Ag^+ toward a developing filament will result in a concentration gradient, causing the filament to be partially dissolved. An illustration

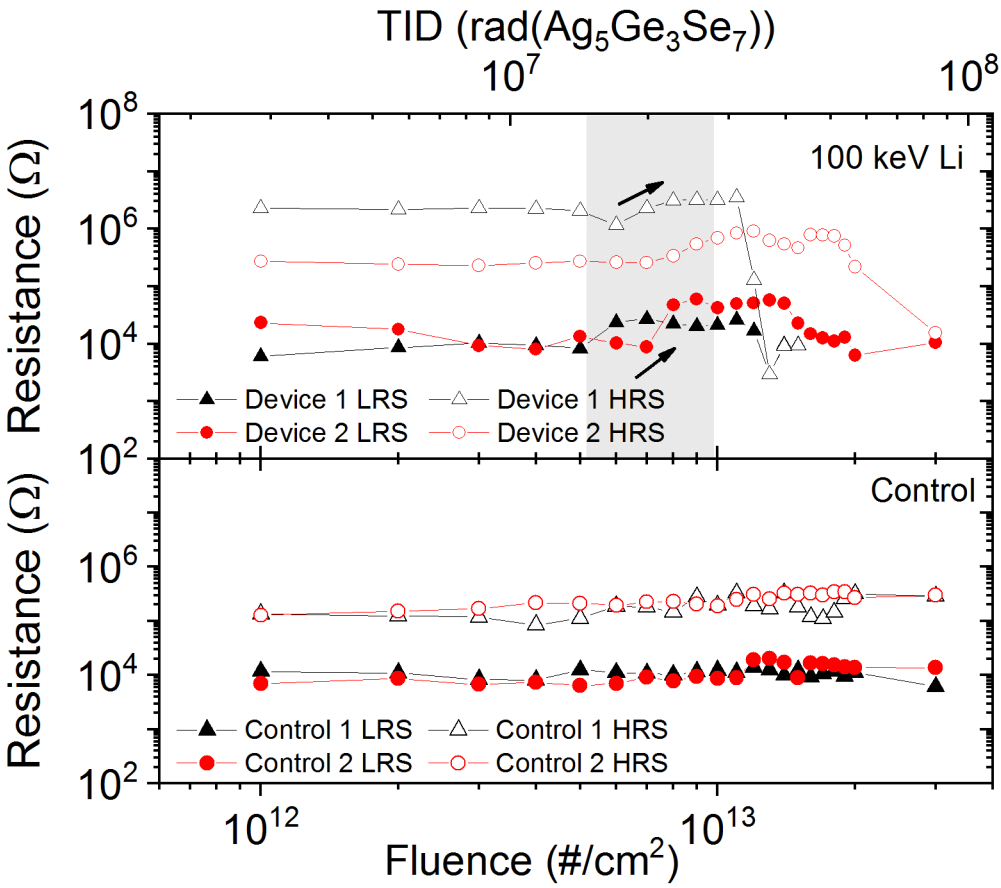

Figure 5.10: Measured HRS and LRS values for each device at each fluence step. Gray region highlights a trend where the resistance of both the HRS and LRS increased prior to shorting. Bottom portion of plot shows the response of two control devices cycled in the same manner as the bombarded devices.

of the filament dissolution is shown in Fig. 5.13. The nonlinear response, in addition to the increase in HRS, provides evidence that the electrolyte region of the device has changed in such a way to diminish Ag migration. This behavior is further discussed in the next chapter.

The programming window of the two devices collapsed after 1.2×10^{13} ions/cm^2 and 3×10^{13} ions/cm^2. The dose at the fluence of failure was added to Fig. 4.9 and is marked in Fig. 5.14. Fig. 5.14 shows that the dose received at failure is within the same magnitude at failure for retention testing, suggesting that the failure mechanism may be the same.

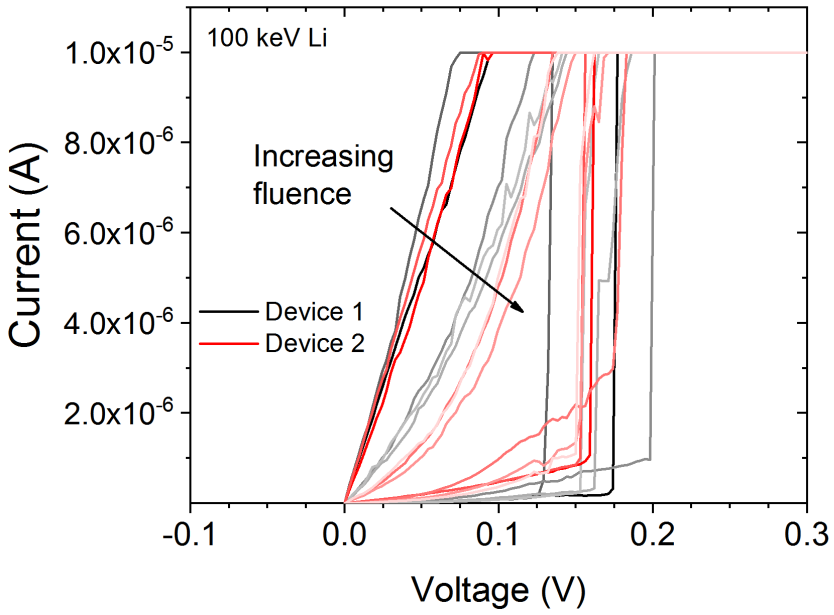

Figure 5.11: Programming I-V sweeps of both irradiated devices at the fluence steps where the resistance was observed to increase. The LRS response of the I-V characteristic is shown to become less linear with increasing fluence.

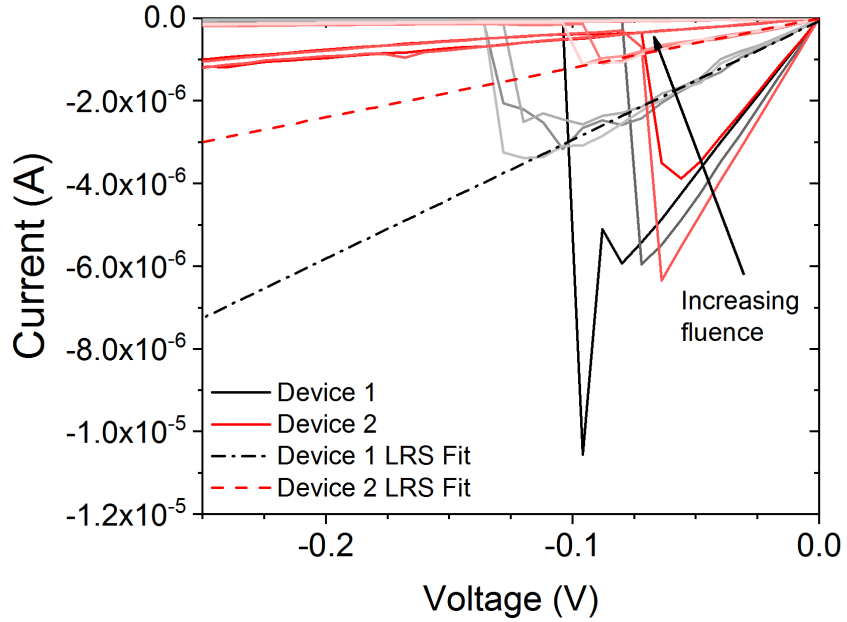

Figure 5.12: Erase I-V sweeps of both irradiated devices at the fluence steps where the resistance was observed to increase. The LRS curve under negative bias is shown to be linear indicating a stable but partially dissolved filament.

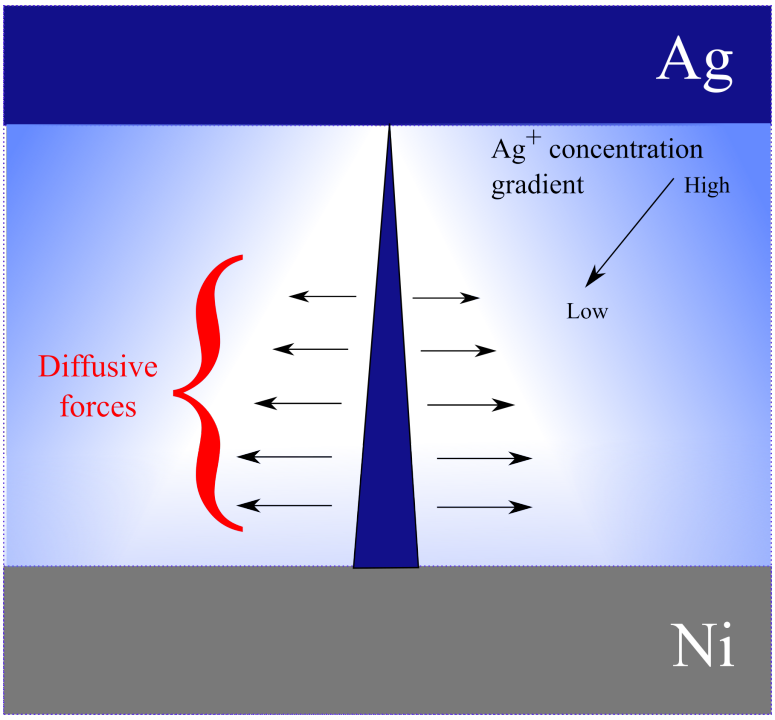

Figure 5.13: As the filament forms, the Ag^+ concentration around the filament decreases. Reduction in ion conductivity makes it difficult to resupply the cation population within a certain period of time, resulting in a concentration gradient with a depletion of Ag in the vicinity of the filament. Diffusive forces, generated by the dense concentration of Ag in the filament, become dominant once the opposing electric field decreases in strength.

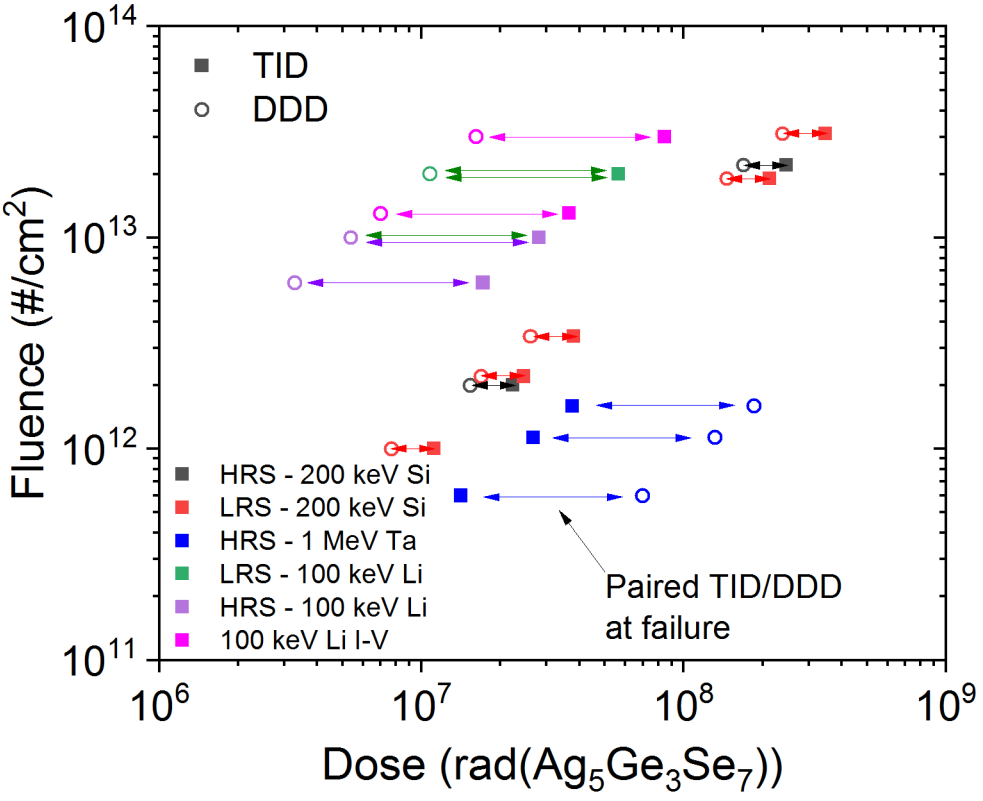

Figure 5.14: Updated TID and DDD distribution with DC cycling failure points added.

Chapter 6

EFFECTS OF RADIATION ON PULSE PROGRAMMING

6.1 Introduction

Pulse programming is a standard method for programming solid-state memory, so it is necessary to evaluate the response to radiation effects. A prior study evaluated the binary pulsed cycling capability of Ag-$Ge_{30}Se_{70}$ CBRAM during ^{60}Co γ-ray irradiation [40]. In that experiment, the devices were exposed in dose steps up to a TID of 4.62 Mrad($Ge_{30}Se_{70}$) and cycled 10000 times after each dose. No effects were observed due to ionizing radiation. Further testing needs to be performed to evaluate any effects due to displacement damage while performing pulsed programming.

In the recent past, neuromorphic programming has become a hot topic with the development of neural network computing and machine learning. In the context of space applications, these new computing methods can be used for processing sensor information quickly on the satellite's computer without the need to send the raw information back to Earth for reduction. Several research groups have offered up resistive memory as an alternative solution to transistor-based neuromorphic circuits [31], [51], [52]. Two types of CBRAM, a CMOS compatible Cu-SiO_2 device and a Ag-$Ge_{30}Se_{70}$ device were shown in previous studies [31],[53], and [54] to have conductance states that could be incrementally increased or decreased to mimic the potentiation and depression of a synapse. The following experiment was first presented in [55] and looks to see how neuromorphic programming of CBRAM is affected while in a ^{60}Co γ-ray TID environment.

6.2 Total Ionizing Dose

6.2.1 Experiment Setup

CBRAM tiles for both device types were diced from the wafers and packaged in a CDIP. Each device was cycled several times with a DC sweep using an Agilent 4156C parameter analyzer to verify the functionality of each device. Prior to testing, the Cu-SiO_2 devices are subjected to a forming sweep to drive Cu into the SiO_2 layer. The DC forming sweep used a double staircase sweep with a 20 mV voltage step from 0 V to 3 V for filament formation and from 0 V to -1 V for filament dissolution. After formation, each device was cycled several times between -1 V to 2 V. The Ag-$Ge_{30}Se_{70}$ devices do not require a formation step, as the Ag is photo-doped throughout the $Ge_{30}Se_{70}$. The Ag-$Ge_{30}Se_{70}$ devices were swept from 0 V to 0.5 V in 10 mV steps for programming and from 0 V to -0.7 to erase the cell. The I-V characteristics of the representative CBRAM cells tested prior to irradiation are shown in Fig. 6.1 and Fig. 6.2 for the Cu-SiO_2 and Ag-$Ge_{30}Se_{70}$ devices, respectively.

Each package was placed into a DIP socket inside a Gammacell 220 chamber, which provided electrical access via ribbon cable to a switch board outside of the irradiation chamber. All device contacts were biased to ground while the test board was lowered into the irradiation chamber. The dose rate inside the chamber was 353 rad(SiO_2)/min (308 rad($Ge_{30}Se_{70}$)/min). Devices were exposed and tested at room temperature. Once inside the chamber, a single device was periodically tested in the following manner: A single pulse was applied to the anode of the device using an Agilent 81160A arbitrary waveform generator. The cathode contact was connected in series to a 2.3 kΩ resistor that helped to regulate the current through the resistive memory cell. Neuromorphic pulsed programming was performed as described in Chapter 3. Pulse and read operations were alternated until the device transitioned

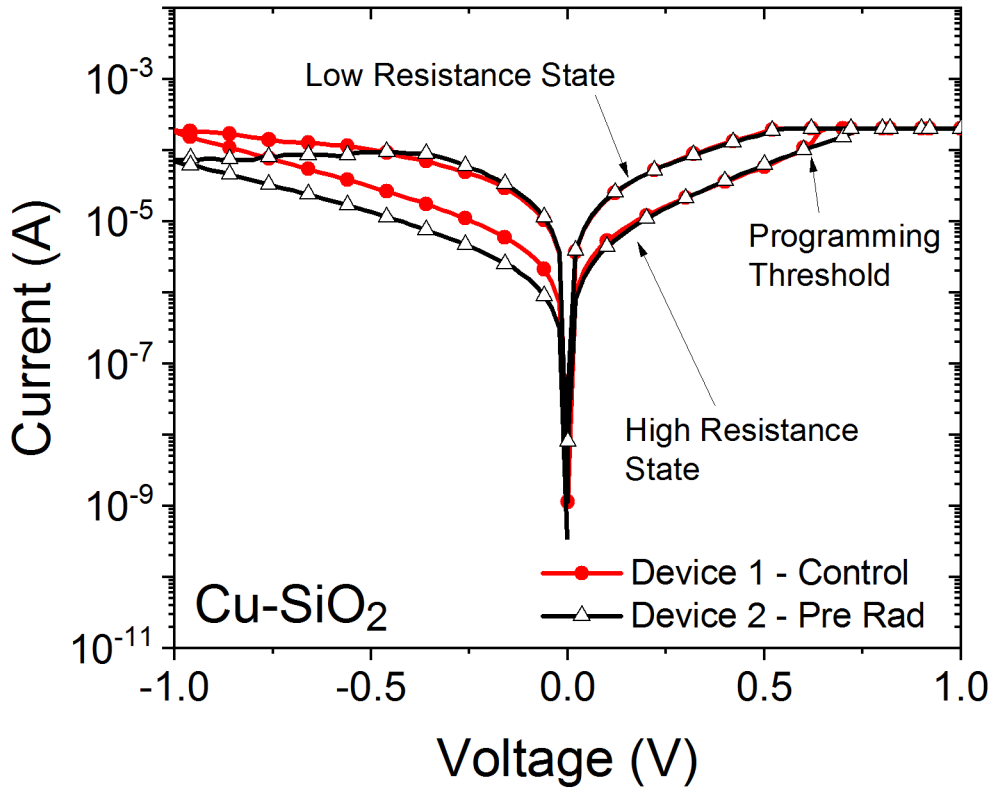

Figure 6.1: I-V characteristics of the Cu-SiO_2 devices prior to irradiation using a 100 μA compliance current.

from a high (low) conductance state to a low (high) conductance state. I-V sweeps were performed prior to irradiation and periodically during the exposure to verify the DC functionality of the device as well as observe the *in situ* behavior during the DC programming. Between measurements, both terminals of the device under test were biased to ground using an Agilent 4156C. Two Ag-$Ge_{30}Se_{70}$ devices were tested, both in the same array. Device 1 was tested to a TID of 40 krad before switching to device 2. Device 2 was tested starting from a TID of 1.3 Mrad($Ge_{30}Se_{70}$) to 1.37 Mrad($Ge_{30}Se_{70}$). Two different packages of Cu-SiO_2 devices were irradiated. In each package, only one device was accessible for testing. Device 1 was irradiated to a TID of 70 krad(SiO_2) and the second device to a TID of 1.05 Mrad(SiO_2). Two control

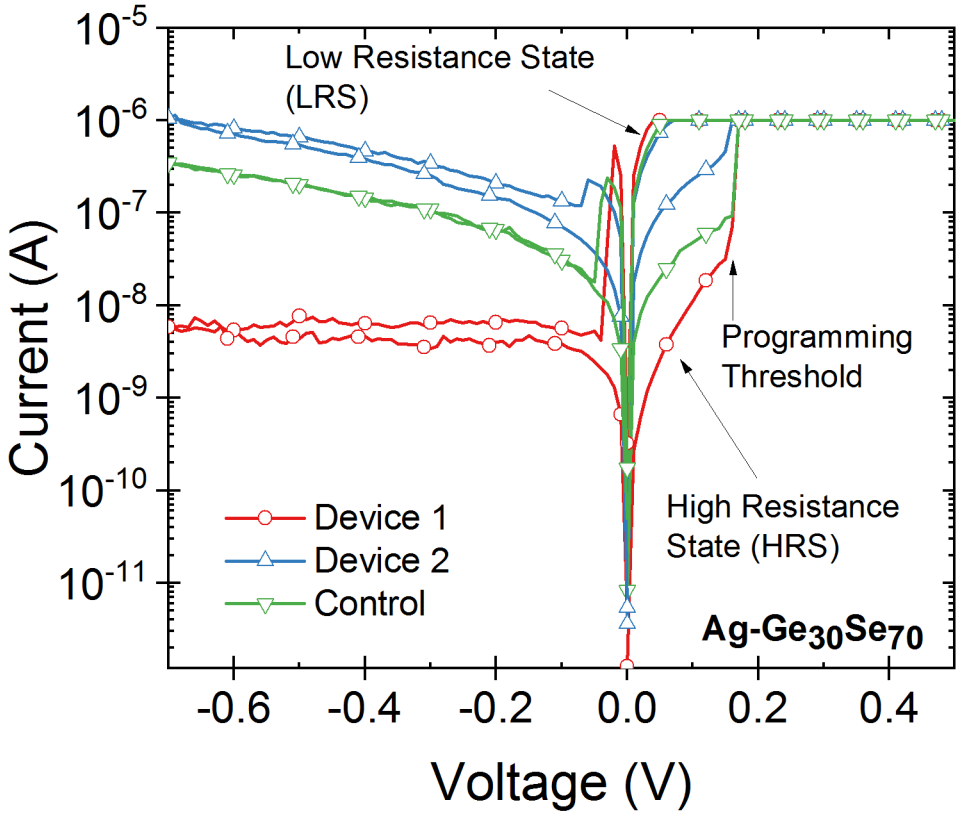

Figure 6.2: I-V characteristics of the Ag-$Ge_{30}Se_{70}$ devices prior to irradiation using a 1 μA compliance current.

devices of each material type were tested at room temperature.

6.2.2 Observed Effects

Ag-$Ge_{30}Se_{70}$ Devices

The results in Fig. 6.3 and Fig. 6.4 show that no significant effects due to ionizing radiation were observed in the DC I-V response. Some distortion to the HRS was observed though it is inconclusive as to whether this variation is due to the repeated operation of the device or due to a TID effect. Based on these results as well as prior TID studies [32]-[34], and [40], the response is most likely due to repeated cycling as well as the addition of Ag into the $Ge_{30}Se_{70}$ film during neuromorphic

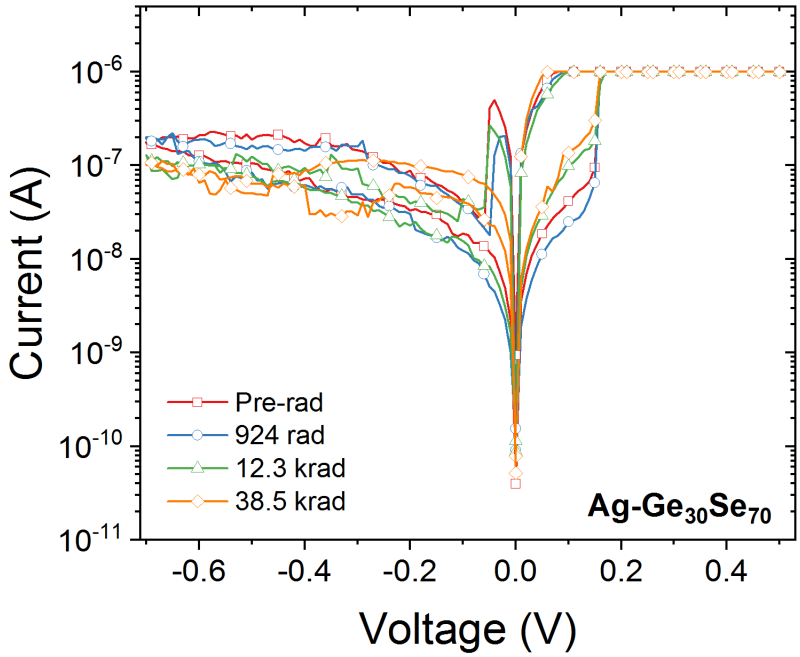

Figure 6.3: I-V characteristics of Ag-$Ge_{30}Se_{70}$ device 1 measured *in situ* during radiation exposure.

testing. During DC testing, the bias is applied over several seconds with increasing or decreasing voltage whereas in neuromorphic testing, the bias is applied briefly for a few microseconds at a fixed voltage.

The Ag-$Ge_{30}Se_{70}$ devices were tested at 5 different exposure points: 16 krad, 24 krad, 60 krad, 1.33 Mrad, and 1.37 Mrad. The neuromorphic programming response at each of these points, as well as the room temperature control, are shown in Fig. 6.5–6.10. During testing, it was observed that filament modulation became more unstable with increasing TID. Potentiation programming (to lower resistance) became erratic, with high variability between each pulse. An increase in potentiation variability is first noticeable at 24 krad ($Ge_{30}Se_{70}$), with a degradation in the ability to program potentiation as the TID increases. Voltage sweeps made between each set of pulse measurements show that the CBRAM cells are functioning correctly for DC, as

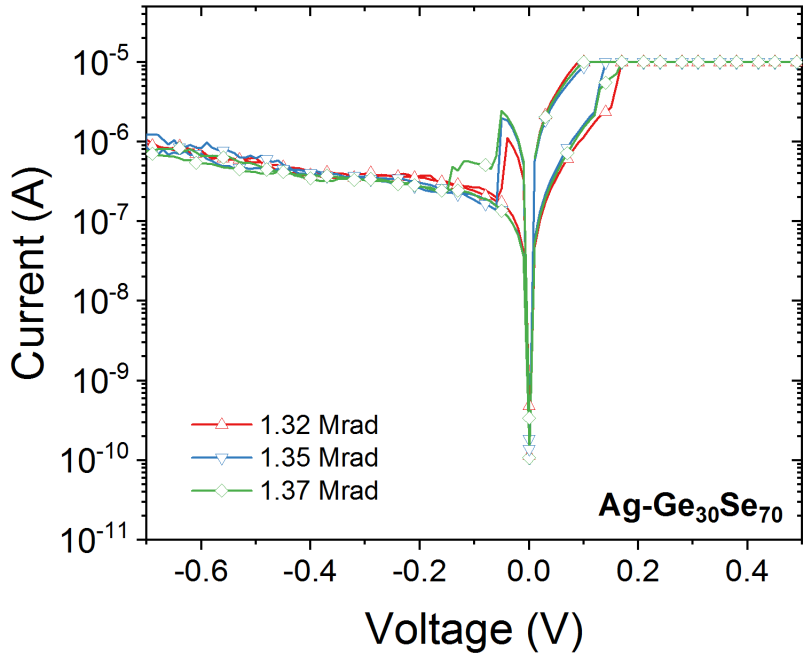

Figure 6.4: I-V characteristics of Ag-$Ge_{30}Se_{70}$ device 2 measured *in situ* during radiation exposure.

depicted in Fig. 6.3 and Fig. 6.4. The increasing variation in pulse programming as well as the stability of the DC response, suggests that the variation in potentiation may be due to the ionizing radiation environment. The depression (thinning of the filament) programming does not experience the same jitter seen during potentiation, but the minimum conductance reached each cycle is observed to fluctuate with increasing dose. In these tests, potentiation and depression pulses were identical but reversed in polarity. The depression programming was observed to experience a large initial conductance change followed by small conductance changes as compared to the conductance change observed during potentiation. Prior studies used variable pulse amplitudes to maintain a relatively uniform change in conductance with each pulse [31], [53].

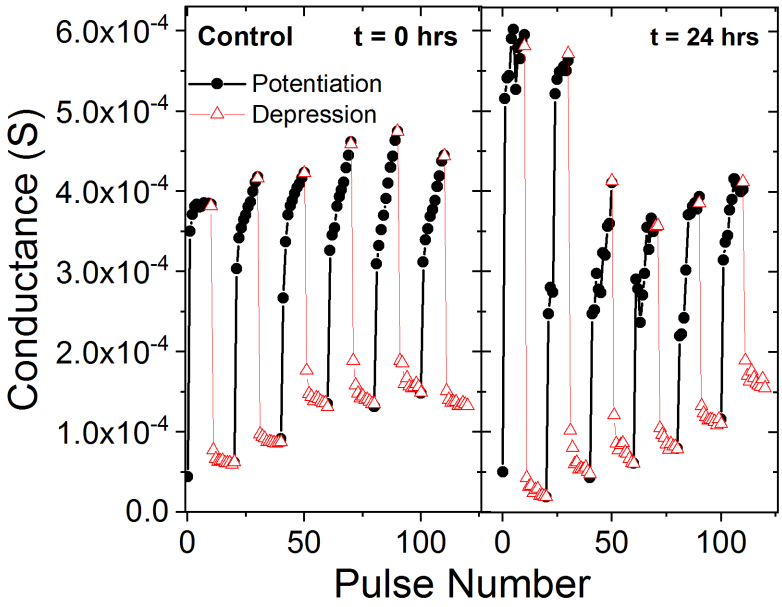

Figure 6.5: Ag-$Ge_{30}Se_{70}$ control at room temperature for incremental conductance changes programmed with 0.5 V amplitude and 1 μs width for potentiation and -0.5 V amplitude for depression. Left-side of figure illustrates initial behavior and the right-side shows the pulse programming response after 24 hours.

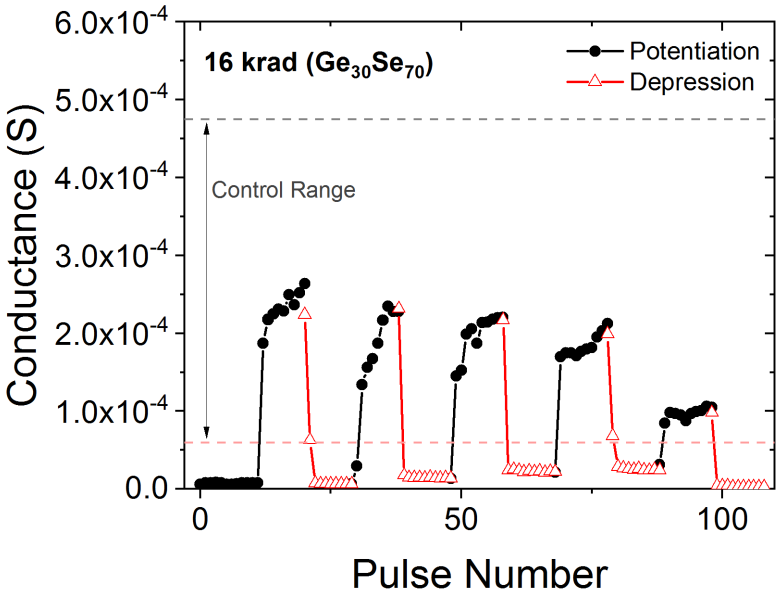

Figure 6.6: Neuromorphic programming of Ag-$Ge_{30}Se_{70}$ devices programmed during irradiation with a pulse of 0.5 V amplitude and 10 μs width for potentiation and -0.5 V amplitude for depression at a TID step of 16 krad. Potentiation and depression range of control marked by the dotted lines.

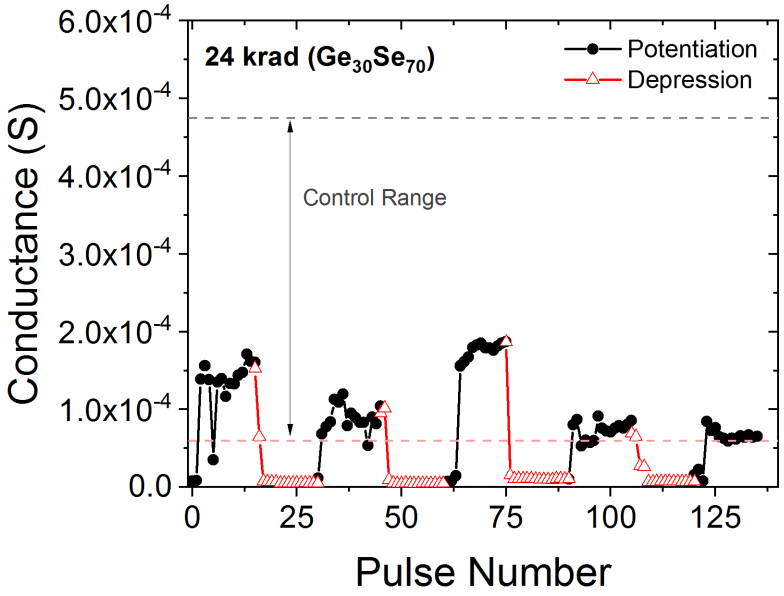

Figure 6.7: Neuromorphic programming of Ag-$Ge_{30}Se_{70}$ devices programmed during irradiation with a pulse of 0.5 V amplitude and 10 μs width for potentiation and -0.5 V amplitude for depression at a TID step of 24 krad.

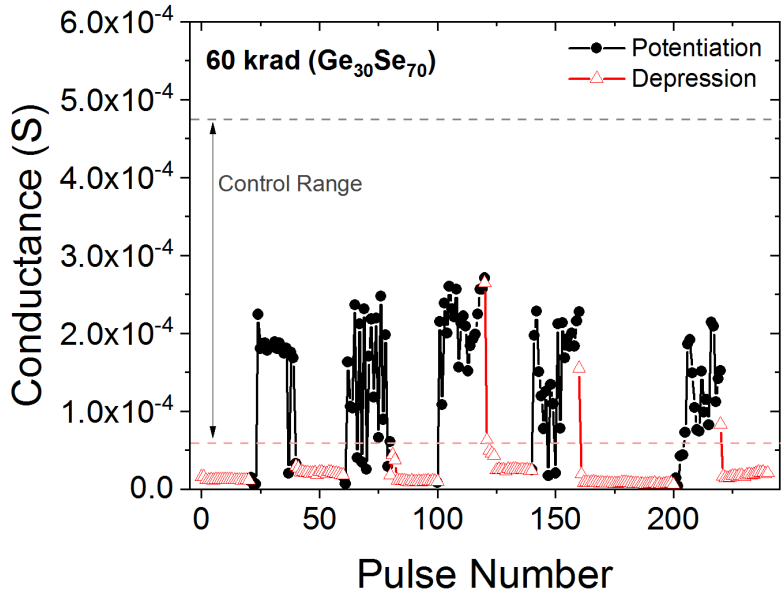

Figure 6.8: Neuromorphic programming of Ag-$Ge_{30}Se_{70}$ devices programmed during irradiation with a pulse of 0.5 V amplitude and 10 μs width for potentiation and -0.5 V amplitude for depression at a TID step of 60 krad.

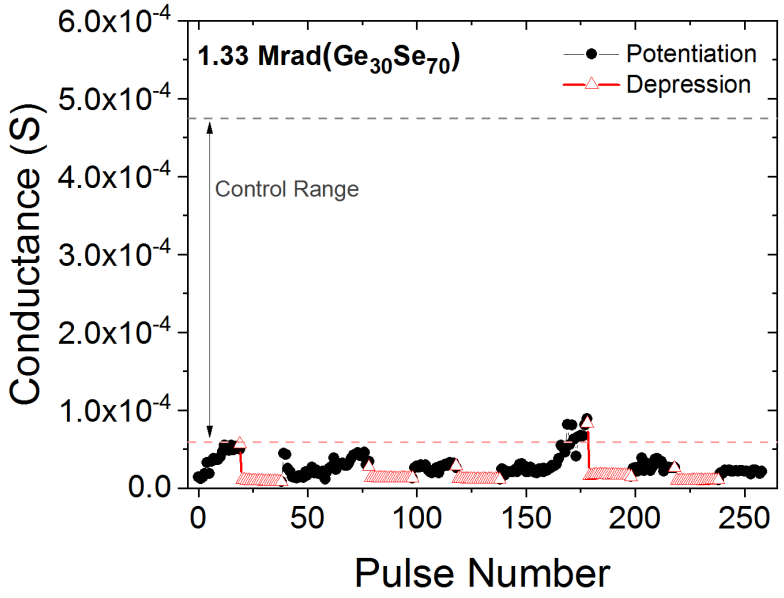

Figure 6.9: Neuromorphic programming of Ag-$Ge_{30}Se_{70}$ devices programmed during irradiation with a pulse of 0.5 V amplitude and 10 μs width for potentiation and -0.5 V amplitude for depression at a TID step of 1.33 Mrad.

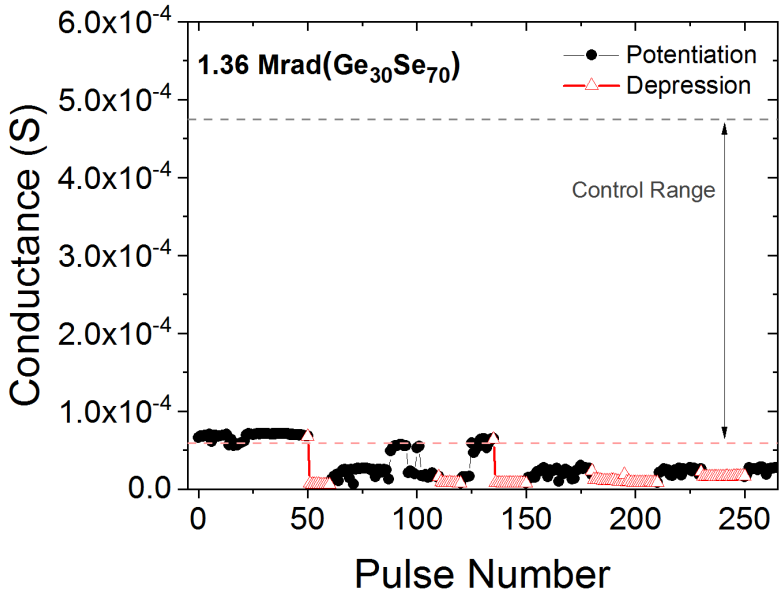

Figure 6.10: Neuromorphic programming of Ag-$Ge_{30}Se_{70}$ devices programmed during irradiation with a pulse of 0.5 V amplitude and 10 μs widths for potentiation and -0.5 V amplitude for depression at a TID step of 1.36 Mrad.

Cu-SiO_2 Devices

The *in situ* I-V characteristics are shown in Fig. 6.11. The high resistance (low conductance) state is shown to remain within the same current range throughout the exposure. The programming voltage threshold is also shown to be extremely consistent in Fig. 6.11. This is the first time that the I-V *in situ* response of Cu-SiO_2 CBRAM has been observed. Previous studies performed step stresses where the sample was irradiated to a desired TID, with contacts left floating, before being removed from the radiation chamber and tested in a lab setting [34]. The study in [34] demonstrated that Cu-SiO_2 cells had no observable shift in DC characteristics for a stress exposure up to 1.5 Mrad(SiO_2). The DC staircase sweep takes several seconds to complete. The small variance of the in situ response and the pre-irradiation sweep displays that there are no significant effects caused by the ionizing radiation on the DC I-V behavior.

The transient pulse response of a non-irradiated Cu-SiO_2 CBRAM cell at room temperature in shown in Fig. 6.12. The pulse width and amplitude were chosen to allow incremental changes toward a low or high conductance state. At room temperature, a pulse amplitude of 1.1 V was used for potentiation and an amplitude of -1.1 V was used for depression. The pulse amplitude was chosen such that it was 200 mV to 300 mV beyond the programming threshold of the device. Fig. 6.11 shows a relatively large increase in conductance during the first few pulses. After the initial jump, the conductance change occurs more gradual. For these devices, the conductance transitioned 3.4×10^{-4} S which corresponds to a resistance change of approximately 20 kΩ.

The pulsed response of irradiated devices is shown in Fig. 6.13 and Fig. 6.14. The transitions shown demonstrate that neuromorphic programming can be per-

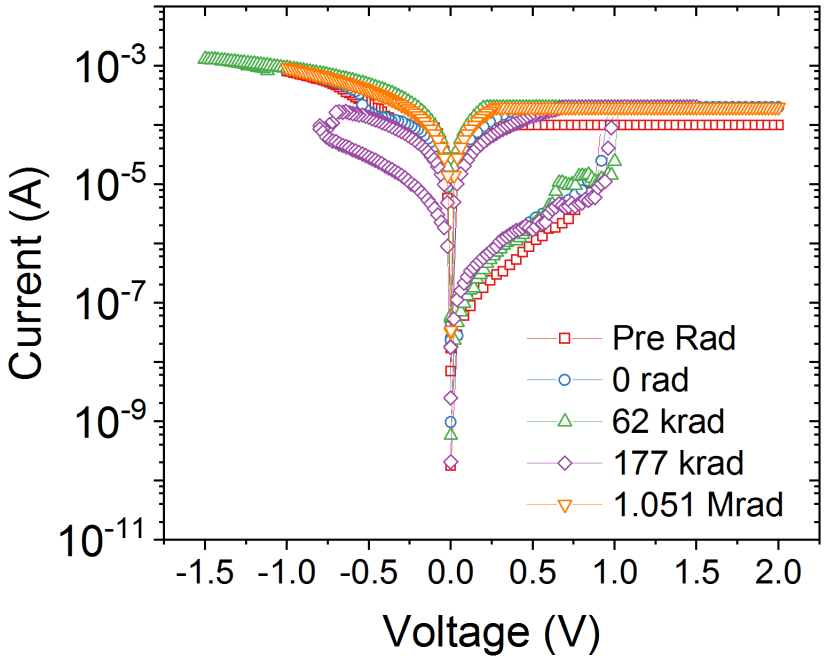

Figure 6.11: I-V characteristics of the Cu-SiO_2 CBRAM cell tested *in situ* during irradiation at several dose steps.

formed during gamma-ray irradiation though the observed conductance response varies greatly from the behavior observed for the unexposed control device tested at room temperature. The devices used during irradiation required a larger programming voltage pulse than the control. The Cu-SiO_2 device shown in Fig. 10 required an increase in pulse amplitude to 1.5 V and a width of 5 μs to induce a conductance change. A pulse amplitude of 1.5 V was used to maintain a 300mV difference above the programming threshold of 1.2 V. The first device was tested at a TID level of 70 krad(SiO_2). The irradiated device shown in Fig. 6.14 required a potentiation pulse of 1.1 V amplitude and 10 μs width. The depression pulse was identical to the potentiation pulse but with a reversed polarity (1.1 V). The second irradiated device was exposed up to 200 krad then pulses were continuously applied until the device was programmed to its pre-irradiated conductance range. The tuning of the

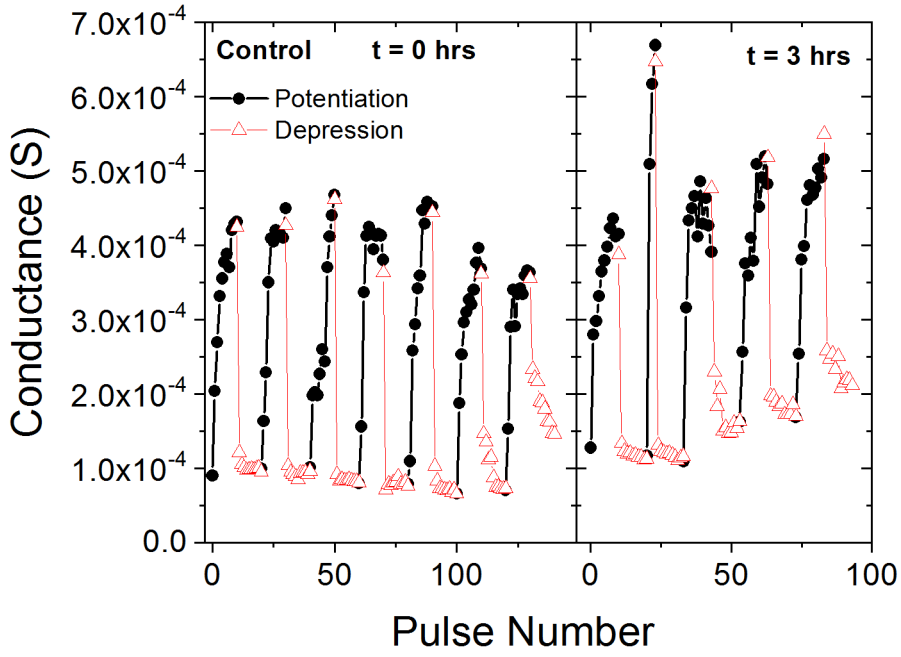

Figure 6.12: Neuromorphic conductance changes programmed with 1.1 V amplitude and 1 μs width for potentiation and -1.1 V amplitude for depression for a non-irradiated device. The left-side of the figure shows the initial programming while the right-side shows the pulse programming behavior three hours later.

conductance was found to transition slower than on non-irradiated devices. Only 10 pulses were needed to complete a full transition for non-irradiated devices while irradiated devices required up to 500 pulses and requiring an enhanced pulse width of 10 μs. The programmable conductance range of the irradiated device was observed to occur over 7.4×10^{-4} S, which was a wider range than the non-irradiated device. With each cycle of potentiation and depression, the maximum potentiation state decreased, eventually decreasing to the off-state conductance. The filament could be reformed by performing a DC sweep.

The Cu-SiO_2 device selected for irradiation had similar DC characteristics to the device used for the control, as shown in Fig. 6.1. All devices were from the same wafer but located on separate die. Deviations in electrical response suggest that the

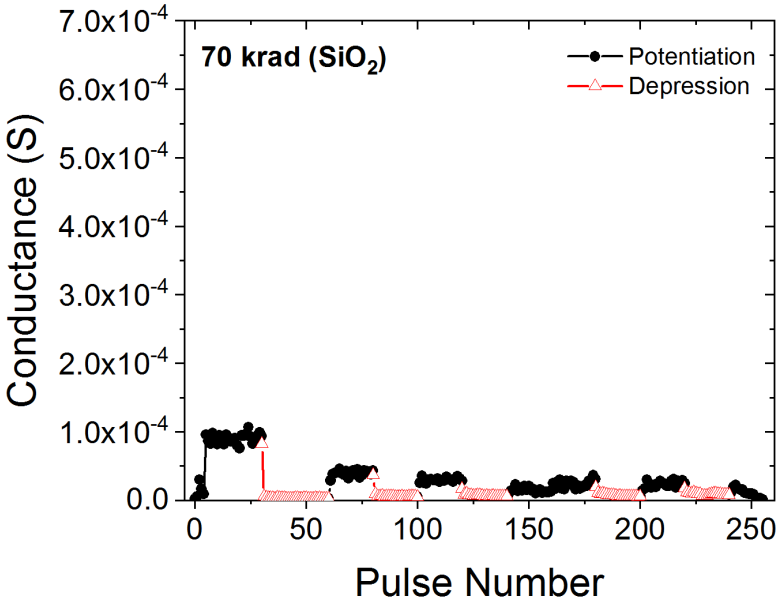

Figure 6.13: Neuromorphic programmed Cu-SiO_2 devices with pulses of 1.5 V amplitude and 5 μs width for potentiation and -1.5 V amplitude for depression.

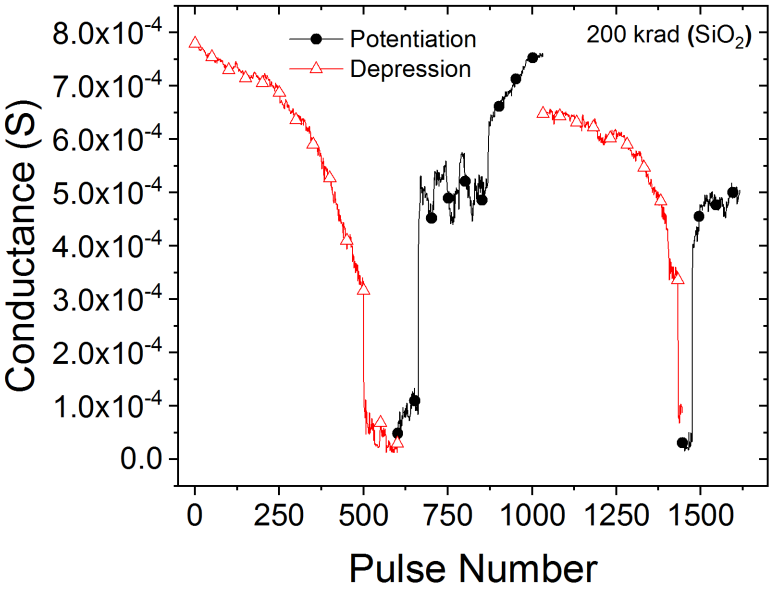

Figure 6.14: Incremental conductance changes at 200 krad(SiO_2) with 1.1 V amplitude and 10 μs width for potentiation and -1.1 V amplitude for depression.

distorted synaptic programming shown in Fig. 6.13 and Fig. 6.14 may be a response to ionizing radiation. Ionic Cu migration through the oxide is a slow process compared to other forms of ECM memory [25], [56]. During the migration, Cu can easily be reduced by a tunneling electron before the ion reaches the cathode. The increase of trap assisted tunneling due to irradiation could increase the number of available electrons that would reduce the mobile Cu ions [57]. Once a metal ion is reduced, it is no longer susceptible to the applied electric field and will cease migration toward the cathode. Filament formation would be slowed by the decrease of mobile Cu ions, as seen in Fig. 6.13 with the decrease in potentiation programming. The result shown in Fig. 6.14 also exhibits fluctuations during potentiation, as well as slow incremental programming, suggesting that ionizing radiation effects with trap assisted tunneling become significant with increasing TID.

The Ag-$Ge_{30}Se_{70}$ devices experienced a similar observable effect with a degradation in the ability to reliably program a high conductance. Previous analysis performed in [58], of the Ag-Ge_xSe_{1-x} material systems, showed that during ionizing irradiation in atmosphere, Ge can become oxidized to create GeO_2. The presence of the insulator would cause the conductance of the film to decrease. The mean of the conductance change caused by a single pulse is illustrated in Fig. 6.15. The effective conductance change per pulse is shown to decrease for both the potentiation and depression pulses with increasing TID. The largest conductance change, for both programming directions, is observed to occur within the first two pulses followed by smaller changes, as depicted in Fig. 6.6–6.10. The maximum conductance step is also observed to decrease with TID, which is most likely due to the decrease in the maximum obtainable conductance state during potentiation. The data population of the control is representative of the conductance changes from two devices and the distribution of TID steps is from the data shown in Fig. 6.6–6.10. The pulse used for the control

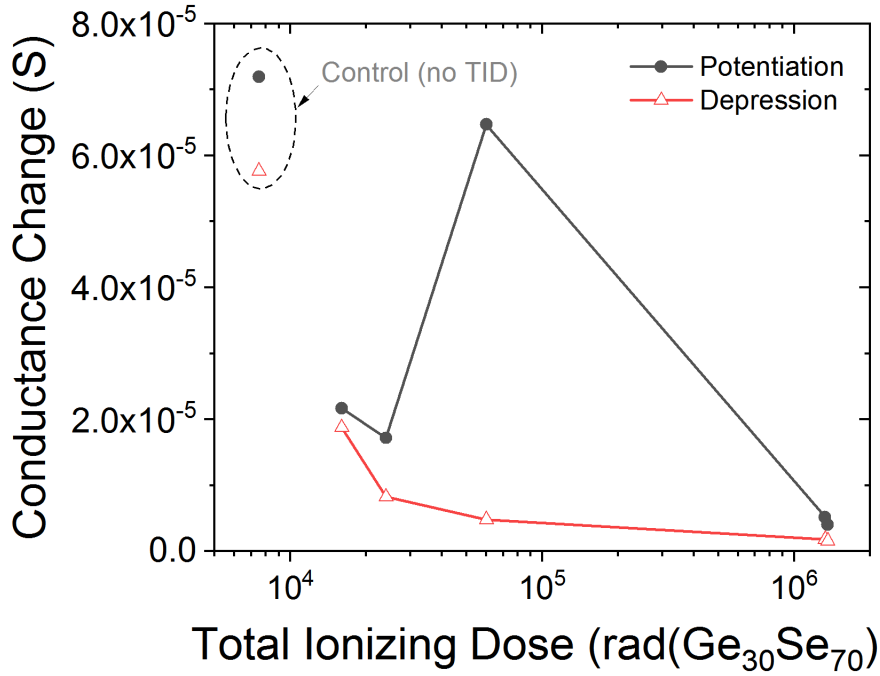

Figure 6.15: Mean conductance change per pulse for Ag-$Ge_{30}Se_{70}$ devices versus TID. The mean conductance change of the control (no radiation) devices is shown in the top left corner. Conductance change produced by a pulse decreased with increasing TID.

devices was 0.5 V / 1 μs while the irradiated devices used a 0.5 V/ 10 μs pulse.

While a TID effect was observed during pulsed programming, no significant effects due to ionizing radiation were observed during DC I-V tests. During DC testing, the bias is applied over several seconds, allowing ample time for the metal ions to migrate between the anode and filament. For the Cu-SiO_2 system, though a certain percentage of the ionic Cu will be reduced due to trap assisted tunneling, as long as a significant population of Cu ions are able to bridge the gap between the anode and the filament, no change in behavior will be observed during DC I-V testing. The same consideration applies to the Ag-$Ge_{30}Se_{70}$ devices. The generation of GeO_2 may decrease the conductance of the electrolyte film but ion migration is still possible and any decrease to drift velocity will not be significantly observable during DC I-V

testing. Slight variations from sweep to sweep in the high resistance is not uncommon in these devices, as shown in Fig. 6.2 and Fig. 6.3, making it difficult to extract or observe minor changes in film conductance due to ionizing radiation. Prior TID studies in [32] and [34] found no distinguishable effects in the HRS due to ionizing radiation during DC testing.

Chapter 7

MECHANISMS OF RADIATION EFFECTS IN $Ag - Ge_{30}Se_{70}$ CBRAM

7.1 Introduction

The work presented in this dissertation has examined the response of CBRAM to TID and DD environments. Each of the electrical tests performed (retention, DC cycling, pulsed programming) were selected to evaluate different transport mechanisms that function in CBRAM devices. Retention tests evaluate the stability of a programmed resistive state and any change of state observed during irradiation provides clues as to how a filament can be formed or dissolved due to radiation. DC cycling is a slow and energy intensive process that provides sufficient time for cation migration to occur. Radiation effects that affect ion migration would be apparent during an I-V sweep; as the under supply or over supply (ion current density) would distort the I-V curve. Uniform pulse programming is a low energy method for programming the CBRAM devices. Changes in ionic conductance can be resolved by examining how effective each applied pulse is in modulating the existing filament. A summary of the tests performed and their purpose, is listed in Table 7.1. This chapter takes into consideration the radiation effects captured during testing and examines what those responses may mean in terms of material changes.

7.2 Discussion of Material Effects

For Se-rich glasses (x $<$ 0.33 in Ge_xSe_{1-x}) the introduction of Ag behaves as a network modifier, forming Ag_2Se crystalline phases throughout the chalcogenide glass network [46], [59]. The Ag_2Se nanocrystals are fast ion conductors, facilitating the

Table 7.1: Electrical and Radiation Tests Performed and Their Purpose for Evaluating Radiation Effects

Test	Purpose
Retention of state	Evaluates how a programmed filament is effected by TID and DD effects. For the case of an erased device (HRS), retention testing is useful for evaluating the susceptibility of a device to become programmed due to radiation effects.
DC current-voltage cycling	Evaluates how ion migration is effected by either TID or DD. During a DC programming sweep, the stability of filament formation can also be evaluated. DC cycling also helps for separating accumulative effects from dose step effects.
Pulsed programming	Evaluates how radiation affects the ionic and electrical conductivity of the switching layer.
^{60}Co γ-ray irradiation	Ionizing dose environment only.
14-MeV Neutron bombardment	Displacement damage environment with minimal TID.
Heavy ion bombardment	Combined TID and DD environment with a significant dose of each radiation type.

hopping of Ag^+ cations through the chalcogenide glass [46], [59]. The nanocrystals act as nucleation sites for filament growth with the dominate filament path dictated by local fields and a sufficient ion supply. A completed bridging filament, from cathode to anode, will be a connect-the-dots structure between the smaller filaments forming from the nanocrystals [19]. Two crystalline phases exist for Ag_2Se. The α-Ag_2Se phase is a body centered cubic with high ion conductivity and the β phase is orthorhombic with a lower ionic conductivity [1], [59], [60]. The unit cell lattice dimensions of the α and β phases are plotted in Fig. 7.1 and the bonding structure is shown in Fig. 7.2. In bulk Ag_2Se, the superionic conductor α phase only exists

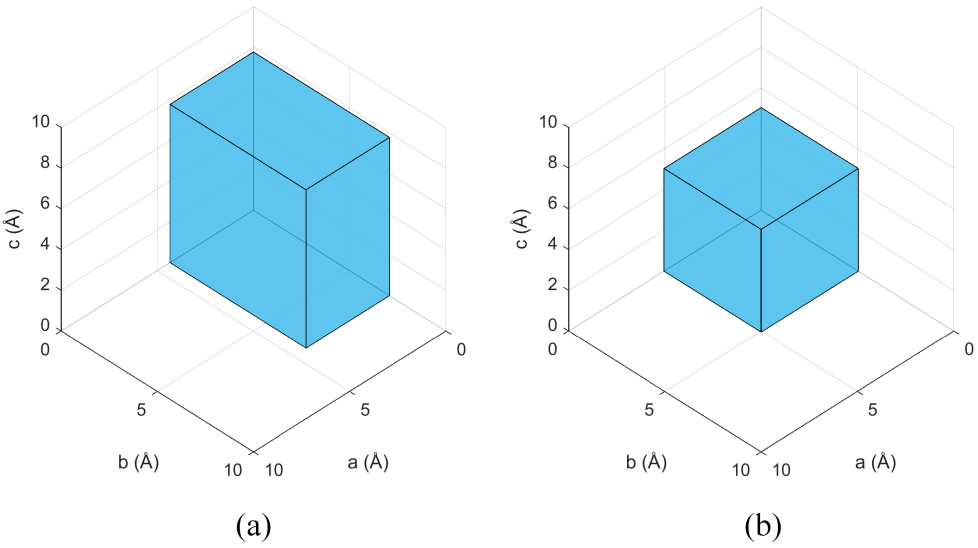

Figure 7.1: Unit cell lattice dimensions of the (a) orthorhombic β-Ag_2Se phase and (b) body-centered cubic α-Ag_2Se phase.

at temperatures above 350°C [59]. One study by Sahu, et. al in [61] shows that the temperature dependence of the α-phase depends on the size of the crystal structure, with nanocrystals capable of existing at as low as 101°C. When Ag is photo-doped into the $Ge_{30}Se_{70}$ glass, Ag is able to fill the voids in the glass and react with Se [1]. As the glass contracts due to UV interactions, the stress placed on the Ag_2Se crystal allows it to exist as α-Ag_2Se [1], [46], [62]. For device temperatures below 100°C, it can be inferred that any damage caused to the Ge-Se backbone would result in the release of the pressure applied to α-Ag_2Se, resulting in the immediate decay to β-Ag_2Se. The creation of β-Ag_2Se during ^{60}Co irradiations has been demonstrated at TID up to 4.5 Mrad [1]. For reference, the X-ray diffraction (XRD) data measured in [1] is shown in Fig. 7.3. The reduction in ion conductivity due to an increasing percentage of β-Ag_2Se could affect the supply of Ag^+ ions needed to properly form the filaments.

The transition from a super ionic conductor to a semiconductor would change the

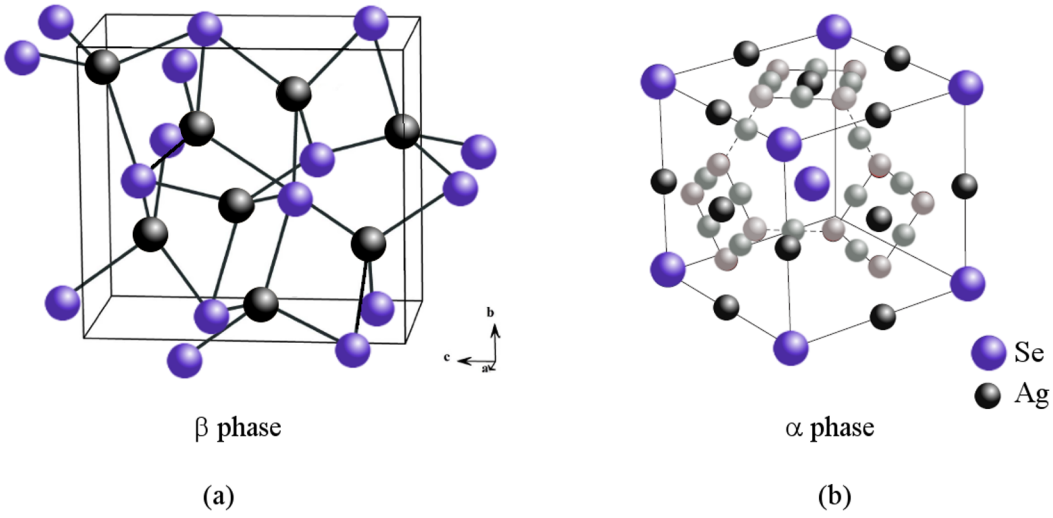

Figure 7.2: Unit cell structure of the (a) orthorhombic β-Ag_2Se phase and [63] (b) body-centered cubic α-Ag_2Se phase [64]. The α-phase has Selenium atoms at the lattice sites with various interstitial locations available for Ag^+ hopping (gray-scale balls).

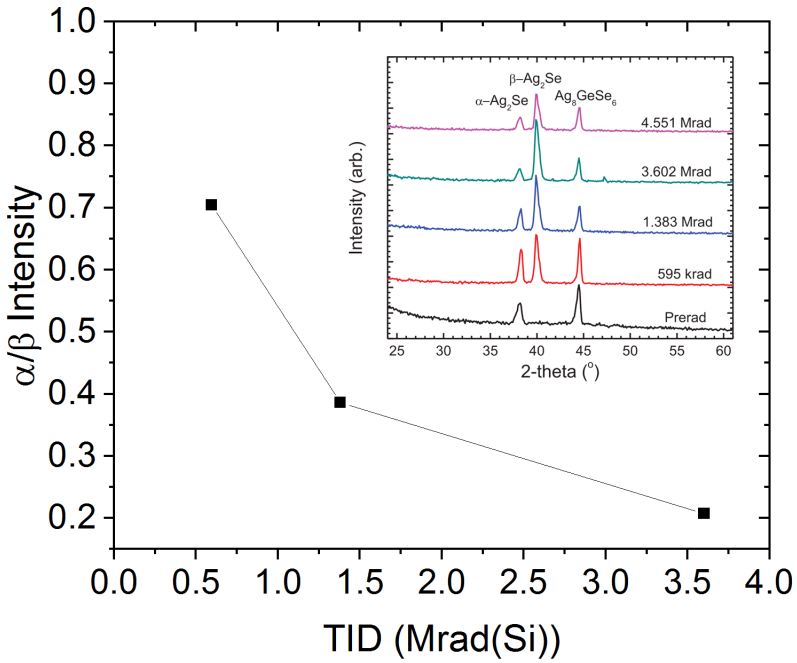

Figure 7.3: XRD results from [1] (inset), showing the formation of β-Ag_2Se after a TID of 595 krad with the $\alpha : \beta$ ratio decreasing with dose.

mechanism of Ag migration, greatly affecting the mobility of the ions. In its α-phase, Fig. 7.2b shows the body-centered cubic Selenide configuration with interstitial sites marked by gray and black balls. The interstitial locations are the sites that facilitate rapid Ag^+ hopping through the electrolyte [64]. Once the electrolyte layer transitions to a more β-phase dominant, a portion of the Ag becomes covalently bonded to the Se, tying up a portion of the Ag available or migration [65]. The ion migration mechanism would become something similar to a metal-insulator devices, like Cu-SiO_2, where the metal ions migrate through voids in the insulator.

The following equation 7.1 from [22], demonstrates how the material change can affect ion migration.

$$J_d = zqN_i u_{th} \exp\left(-\frac{E_o}{kT}\right) \sinh\left(\frac{azq\varepsilon}{2kT}\right) \tag{7.1}$$

J_d is the ion drift current density, zq is the charge of the ion ($z = 1$ for Ag), N_i is the cation concentration, $E_o = 0.2$ eV is the barrier hight for hopping, $u_{th} = (2KT/m_i)^{1/2} \approxeq av$, m_i is the ion mass, a is the hopping distance, v is the hopping frequency, ε is the applied electric field, and kT is the thermal energy. Assuming no external change to the system, ε and T would remain about the same. E_o may increase slightly but density functional theory calculations have shown that it should remain about 0.2 eV [65]. The hopping distance would increase but would remain within the same magnitude (<5Å) and because of the relation between a and v, v should scale accordingly. The only term in Eqn. 7.1 that should have a significant affect on the ion current density J_d is N_i. The relation could then simplify to,

$$J_d \propto N_i. \tag{7.2}$$

For example, if $N_i = 10^{22}$ cm^{-3} for Ag^+ in a non-irradiated electrolyte, a change by one magnitude, to $N_i = 10^{21}$ cm^{-3} (comparable to Cu^{2+} in SiO_2) would diminish the

ion drift current density by the same amount. As discussed in Chapter 5 and 6, a decrease in the ion current would create a lag in the ion supply around the forming filament, allowing diffusive forces to take hold once the electric field is removed. The evidence of reduced ion current due to TID effects has been made evident by the response of CBRAM while performing pulse programming. Looking back at Fig. 6.15, there is a predictable trend in the conductance change with increasing dose. The erratic behavior of the potentiation during the 24 krad and 60 krad dose steps, could also be explained by the ion supply. The application of the electric field is controlled by the width of the voltage pulse. During the time the field is applied, the ions only have a limited amount of time to reach the filament and reduce. If the Ag concentration gradient becomes prevalent with increasing TID, the filament would partially dissolve and settle in a higher resistance state. Due to the time lag between applying the pulse and reading the state, the resistive state measured may be captured during or after the filament dissolution. Once the electrolyte is damaged to the point where the applied pulse is greatly ineffective in transporting ions, the potentiation response smooths out.

For the DC cycling tests during 100 keV Li-ion exposure, failures occurred within the same fluence range as retention testing, as shown in Fig. 5.14. The similar fluence threshold indicates that the failure mechanism may be the same for both tests. Based on DC sampling taken pre and post each fluence step, at failure, the devices were observed to short prior to the I-V sweep being performed. After shorting, many devices could be partially erased after several erase sweeps, indicating that the short was due to an introduction of Ag and not due to a material change resulting in a permanent conductive path. It is not yet clear what mechanism is responsible for the introduction of excess Ag. At high TID, Ag may be introduced via local fields created from carrier generation. The creation of the β-Ag_2Se phase may reduce the

recombination rate of carriers, allowing a buildup of charge. Further material analysis, such as XRD and Raman spectroscopy, is necessary to determine how the switching layer is evolving at these higher doses of radiation.

Chapter 8

CONCLUSION

The work presented in this document investigated the effects of ionizing radiation and displacement damage on the retention of state, DC programming, and neuromorphic pulsed programming of Ag-$Ge_{30}Se_{70}$ CBRAM devices. The main contribution of this dissertation was showing that CBRAM devices are susceptible to both environments. Material changes in the electrolyte layer due to TID has previously been documented in [1] using bulk material films though no electrical effects have been observed, until now. Neuromorphic pulsed programming was shown to be inhibited by a TID environment. This dissertation demonstrated an observable electrical response to an *in situ* TID environment in CBRAM at a dose below 60 krad($Ge_{30}Se_{70}$). Prior TID tests have only looked at the DC response and pulsed cycling using long pulses [40]. DC cycling in a 14 MeV neutron environment (majority DD) showed a collapse of the HRS and LRS programming window after a fluence of 4.9×10^{12} n/cm^2, demonstrating the CBRAM can fail in a DD environment. Heavy ion exposure during retention testing and DC cycling, showed that failures to programming occurred at approximately the same threshold, indicating that the failure mechanism, for the two types of tests, may be the same. By separating the dose received from LET and NIEL of each ion type at the fluence of failure, TID values appear to be the most correlated, indicating that TID effects may be the dominate failure mechanism in a combined environment. It is currently unclear as to how the displacement damage also contributes to the response. To better understand the full mechanism of failure, material measurements on bulk electrolyte material would need to be performed at several dose steps, with different forms or radiation, to separate TID and DD effects.

The doses and particle fluences evaluated in this dissertation are beyond what a device would be exposed to in an Earth radiation environment. The majority of results presented, though academically interesting, would only be relevant in a high dose radiation environment, such as the Jovian environment. Prior TID testing, in addition to the results presented in this work, show that CBRAM can be used in a high dose Jovian environment, however, operation of CBRAM would be limited to slow pulsing to program and erase the memory, as high speed pulsing was shown to be susceptible to TID below 60 krad($Ge_{30}Se_{70}$).

REFERENCES

[1] M. S. Ailavajhala, Y. Gonzalez-Velo, C. Poweleit, H. Barnaby, M. N. Kozicki, K. Holbert, D. P. Butt, and M. Mitkova, "Gamma radiation induced effects in floppy and rigid Ge-containing chalcogenide thin films," *J. Appl. Phys.*, vol. 115, no. 4, p. 043502, Jan. 2014.

[2] "Sputnik," *Science*, vol. 126, no. 3277, pp. 739–740, Oct. 1957.

[3] J. A. Van Allen, *Origins Of Magnetospheric Physics: An Expanded Edition.* University of Iowa Press, 2004. [Online]. Available: https://ebookcentral-proquest-com/lib/asulib-ebooks/detail.action?docID=843261

[4] J. A. Van Allen, "The earth and near space," *Bull. At. Sci.*, vol. 17, no. 5/6, pp. 218–222, 1961.

[5] N. F. Ness and J. M. Wilcox, "Solar origin of the interplanetary magnetic field," *Phys. Rev. Lett.*, vol. 13, no. 15, pp. 461–464, 1964.

[6] J. A. V. Allen, D. N. Baker, B. A. Randall, and D. D. Sentman, "The magnetosphere of jupiter as observed with pioneer 10: 1. instrument and principal findings," *J. of Geophysical Res.*, vol. 79, no. 25, pp. 3559–3577, 9 1974.

[7] S. Bourdarie and M. Xapsos, "The near-Earth space radiation environment," *IEEE Trans. Nucl. Sci.*, vol. 55, no. 4, pp. 1810–1832, Aug. 2008.

[8] W. Shockley, "Problems related to p-n junctions in silicon," *Solid-State Elec.*, vol. 2, no. 1, pp. 35–67, 1961.

[9] S. Messenger, E. Burke, G. Summers, M. Xapsos, R. Walters, E. Jackson, and B. Weaver, "Nonionizing energy loss (NIEL) for heavy ions," *IEEE Trans. Nucl. Sci.*, vol. 46, no. 6, pp. 1595–1602, 1999.

[10] F. B. McLean and T. R. Oldharn, "Basic mechanisms of radiation effects in electronic materials and devices," *Harry Diamond Laboratories Technical Report*, no. HDL-TR-2 129, Sep. 1987.

[11] G. H. Kinchin and R. S. Pease, "The displacement of atoms in solids by radiation," *Reports on Progress in Phys.*, vol. 18, no. 1, pp. 1–52, 1955.

[12] M. Cherng, I. Jun, and T. Jordan, "Optimum shielding in Jovian radiation environment," *Nuclear Instruments and Methods in Physics Research Section A: Accelerators, Spectrometers, Detectors and Associated Equipment*, vol. 580, no. 1, pp. 633–636, 2007.

[13] K. Strauss and T. Daud, "Overview of radiation tolerant unlimited write cycle non-volatile memory," *in the proc. of Aero. Conf., Big Sky, MT*, Mar. 2002.

[14] (2013) International technology roadmap for semiconductors 2013. [Online]. Available: http://www.itrs.net/

[15] I. Valov, R. Waser, J. R. Jameson, and M. N. Kozicki, "Electrochemical metallization memories-fundamentals, applications, prospects," *Nanotechnology*, vol. 22, no. 25, p. 254003, Jun. 2011, 2011.

[16] F. Irom, D. N. Nguyen, R. Harboe-Sørensen, and A. Virtanen, "Evaluation of mechanisms in TID degradation and SEE susceptibility of single and multi-level high density NAND flash memories," *IEEE Trans. Nucl. Sci.*, vol. 58, no. 5, pp. 2477–2482, Oct. 2011.

[17] F. Irom, G. R. Allen, "Radiation Tests of Highly Scaled, High-Density, Commercial, Nonvolatile NAND Flash Memories-Update 2012," NASA JPL Publication 12-19 12/12. [Online]. Available: http://ntrs.nasa.gov/archive/nasa/casi.ntrs.nasa.gov/20140000667.pdf

[18] M. N. Kozicki, M. Park, and M. Mitkova, "Nanoscale memory elements based on solid-state electrolytes," *IEEE Trans. Nanotechnol*, vol. 4, pp. 331–338, May 2005.

[19] M. N. Kozicki and M. Mitkova, "Mass transport in chalcogenide electrolyte films materials and applications," *J. Non-Cryst. Solids*, vol. 352, pp. 567–577, Mar. 2006.

[20] I. Valov and M. N. Kozicki, "Cation-based resistance change memory," *J. Phys. D, Appl. Phys.*, vol. 46, no. 7, p. 074005, Feb. 2013.

[21] X. Guo, C. Schindler, S. Menzel, and R. Waser, "Understanding the switching-off mechanism in Ag+ migration based resistively switching model systems," *Appl. Phys. Lett.*, vol. 91, p. 133513, 2007.

[22] M. N. Kozicki and H. J. Barnaby, "Conductive bridging random access memory - materials, devices and applications," *Semicond. Sci. Technol.*, vol. 31, p. 113001, Oct. 2016.

[23] U. Russo, D. Kamalanathan, D. Ielmini, A. L. Lacaita, and M. N. Kozicki, "Study of multilevel programming in programmable metallization cell (PMC) memory," *IEEE Trans. Electron Devices*, vol. 56, no. 5, pp. 1040–1047, May 2009.

[24] J. R. Jameson, N. Gilbert, F. Koushan, J. Saenz, and J. Wang, "Effects of cooperative ionic motions on programming kinetics of conductive-bride memory cells," *Appl. Phys. Lett.*, vol. 100, p. 23505, 2012.

[25] M. N. Kozicki, M. Balakrishnan, C. Gopalan, C. Ratnakumar, and M. Mitkova, "Programmable metallization cell memory based on Ag-Ge-S and Cu-Ge-S solid electrolytes," *Proc. NVMTS*, pp. 83–89, 2005.

[26] A. V. Kolobov and S. R. Elliott, "Photodoping of amorphous chalcogenides by metals," *Advances in Physics*, vol. 40, no. 5, pp. 625–684, 1991.

[27] M. Mitkova and M. N. Kozicki, "Silver incorporation in GeSe glasses used in programmable metallization cell devices," *J. Non-Cryst. Solids*, vol. 299-302, no. 2, pp. 1023–1027, Apr. 2002.

[28] M. Mitkova, M. N. Kozicki, H. C. Kim, and T. L. Alford, "Local structure resulting from photo and thermal diffusion of Ag in GeSe thin films," *J. Non-Cryst. Solids*, vol. 338-340, pp. 552–556, 2004.

[29] S. Rajabi, M. Saremi, H. J. Barnaby, A. Edwards, M. N. Kozicki, Y. Gonzalez-Velo, M. Mitkova, D. Mahalanabis, and A. Mahmud, "Static impedance behavior of programmable metallization cells," *Solid-State Elec.*, vol. 106, pp. 27–33, Apr. 2015.

[30] S. Hyun Jo, T. Chang, I. Ebong, B. B. Bhadviya, P. Mazumder, and W. Lu, "Nanoscale memristor device as synapse in neuromorphic systems," *Nano Lett.*, vol. 10, pp. 1297–1301, 2010.

[31] W. Chen, R. Fang, M. B. Balaban, W. Yu, Y. Gonzalez-Velo, H. J. Barnaby, and M. N. Kozicki, "A CMOS-compatible electronic synapse device based on cu/sio$_2$/w programmable metallization cells," *Nanotechnology*, vol. 27, p. 255202, 2016.

[32] Y. Gonzalez-Velo, H. J. Barnaby, M. N. Kozicki, P. Dandamudi, A. Chandran, K. E. Holbert, M. Mitkova, and M. Ailavajhala, "Total-ionizing dose effects on the resistance switching characteristics of chalcogenide programmable metallization cells," *IEEE Trans. Nucl. Sci.*, vol. 60, no. 6, pp. 4563–4569, Dec. 2013.

[33] Y. Gonzalez-Velo, A. Mahmud, W. Chen, J. L. Taggart, H. J. Barnaby, M. N. Kozicki, K. E. Holbert, M. Ailavajhala, and M. Mitkovai, "Radiation hardening by process of cbram resistance switching cells," *IEEE Trans. Nucl. Sci.*, vol. 63, no. 4, pp. 2145–2151, Aug. 2016.

[34] W. Chen, H. J. Barnaby, M. N. Kozicki, A. H. Edwards, Y. Gonzalez-Velo, R. Fang, K. E. Holbert, S. Yu, and W. Yu, "A study of gamma-ray exposure of Cu-SiO2 programmable metallization cells," *IEEE Trans. Nucl. Sci.*, vol. 62, no. 6, pp. 2404–2411, Nov. 2015.

[35] J. L. Taggart, R. Fang, Y. Gonzalez-Velo, H. J. Barnaby, M. N. Kozicki, J. L. Pacheco, E. S. Bielejec, M. L. McLain, N. Chamele, A. Mahmud, and M. Mitkova, "Resistance state locking in CBRAM cells due to displacement damage effects," *IEEE Trans. Nucl. Sci.*, vol. 64, no. 8, pp. 2300–2306, Aug. 2017.

[36] D. R. Hughart, J. L. Pacheco, A. J. Lohn, P. R. Mickel, E. Bielejec, G. Vizkelethy, B. L. Doyle, S. L. Wolfley, P. E. Dodd, M. R. Shaneyfelt, M. L. McLain, and M. J. Marinella, "Mapping of radiation-induced resistance changes and multiple conduction channels in TaOx memristors." *IEEE Trans. Nucl. Sci.*, vol. 61, no. 6, pp. 2965–2971, Dec. 2014.

[37] D. R. Hughart, A. J. Lohn, P. R. Mickel, S. M. Dalton, P. E. Dodd, M. R. Shaneyfelt, A. I. Silva, E. Bielejec, G. Vizkelethy, M. T. Marshall, M. L. Mclain, and M. J. Marinella, "A comparison of the radiation response of TaOx and TiO2 memristors," *IEEE Trans. Nucl. Sci.*, vol. 60, no. 6, pp. 4512–4519, Dec. 2013.

[38] D. R. Hughart, S. M. Dalton, P. R. Mickel, P. E. Dodd, M. R. Shaneyfelt, E. Bielejec, G. Vizkelethy, and M. J. Marinella, "Total ionizing dose and displacement damage effects on TaOx memristive memories," in *2013 IEEE Aerosp. Conf.*, Big Sky, MT, Mar 2013, pp. 1–10.

[39] J. F. Ziegler, M. D. Ziegler, and J. P. Biersack, "SRIM—the stopping and range of ions in matter (2010)," *Nucl. Instr. Meth. Phys. Res. B*, vol. 268, pp. 1818–1823, 2010.

[40] J. L. Taggart, Y. Gonzalez-Velo, D. Mahalanabis, A. Mahmud, H. J. Barnaby, M. N. Kozicki, K. E. Holbert, M. Mitkova, K. W. an E. Deionno, and A. L. White, "Ionizing radiation effects on non-volatile memory properties of programmable metallization cells," *IEEE Trans. Nucl. Sci.*, vol. 61, no. 6, pp. 2985–2990, Dec. 2014.

[41] J. L. Taggart, R. Fang, Y. Gonzalez-Velo, H. J. Barnaby, M. N. Kozicki, N. Chamele, A. Mahmud, and M. Mitkova, "Effects of 14 MeV neutron irradiation on the DC characteristics of CBRAM cells," in *Proc. IEEE RADECS*, Bremen, Germany, Sep. 2016, pp. 1–4.

[42] M. N. Kozicki, C. Gopalan, M. Balakrishnan, M. Park, and M. Mitkova, "Non-volatile memory based on solid electrolytes," *Proc. Non-Volatile Memory Technol. Symp.*, pp. 10–17, 2004.

[43] M. Kozicki, M. Mitkova, M. Park, M. Balakrishnan, and C. Gopalan, "Information storage using nanoscale electro deposition of metal in solid electrolytes," *Superlattices and Microstructures*, vol. 34, pp. 459–465, Dec. 2003.

[44] M. Mitkova, M. Kozicki, H. Kim, and T. Alford, "Crystallization effects in annealed thin ge?se films photodiffused with ag," *J. Non-Cryst. Solids*, vol. 325, pp. 1986–1990, 2006.

[45] T. Kawaguchi, S. Maruno, and S. R. Elliott, "Optical, electrical, and structural properties of amorphous AgGeS and AgGeSe films and comparison of photoinduced and thermally induced phenomena of both systems," *J. Appl. Phys.*, vol. 79, pp. 9096–9104, Jun. 1996.

[46] M. Mitkova, Y. Wang, and P. Boolchand, "Dual chemical role of ag as an additive in chalcogenide glassess," *Phys. Rev. Lett.*, vol. 83, no. 19, pp. 3848–3851, 1999.

[47] M. N. Kozicki and H. J. Barnaby, "Conductive bridging random access memory–materials, devices, and applications," *Semicond. Sci. Technol.*, vol. 31, no. 11, p. 113001, Oct. 2016.

[48] A. Belmonte, R. Degraeve, A. Fantini, W. Kim, M. Houssa, M. Jurczak, and L. Goux, "Origin of the current discretization in deep reset states of an al2o3/cu-based conductive-bridging memory, and impact on state level and variability," *Appl. Phys. Lett.*, vol. 104, p. 233508, 2014.

[49] D. Kamalanathan, A. Akhavan, and M. N. Kozicki, "Low voltage cycling of programmable metallization cell memory devices," *Nanotechnology*, vol. 22, no. 25, p. 254017, Jun. 2011.

[50] W. Chen, R. Fang, H. J. Barnaby, M. B. Balaban, Y. Gonzalez-Velo, J. L. Taggart, A. Mahmud, K. Holbert, A. H. Edwards, and M. N. Kozicki, "Total-ionizing-dose effects on resistance stability of programmable metallization cell based memory and selectors," *IEEE Trans. Nucl. Sci.*, vol. 64, no. 1, pp. 269–276, Jan. 2017.

[51] S. H. Jo, T. Chang, I. Ebong, B. B. Bhadviya, P. Mazumder, and W. Lu, "Nanoscale memristor device as synapse in neuromorphic systems," *Nano Lett.*, vol. 10, no. 4, pp. 1297–1301, 2010.

[52] S. Yu, Y. Wu, R. Jeyasingh, D. Kuzum, and H.-S. P. Wong, "An electronic synapse device based on metal oxide resistive switching memory for neuromorphic computation," *Nano Lett.*, vol. 58, no. 8, pp. 2729–2737, Aug. 2011.

[53] D. Mahalanabis, H. J. Barnaby, Y. Gonzalez-Velo, M. Kozicki, S. Vrudhula, and P. Dandamudi, "Incremental resistance programming of programmable metallization cells for use as electronic synapses," *Solid-State Elec.*, vol. 100, pp. 39–44, Oct. 2014.

[54] D. Mahalanabis, M. Sivaraj, W. Chen, S. Shah, H. Barnaby, M. Kozicki, J. B. Christen, and S. Vrudhula, "Demonstration of spike timing dependent plasticity in CBRAM devices with silicon neurons," *in IEEE Intl. Symp. on Circuits and Systems (ISCAS), Montreal, Canada*, pp. 2314–2317, May 2017.

[55] J. L. Taggart, W. Chen, Y. Gonzalez-Velo, H. J. Barnaby, K. Holbert, and M. N. Kozicki, "In situ synaptic programming of CBRAM in an ionizing radiation environment," *IEEE Trans. Nucl. Sci.*, vol. 65, no. 1, pp. 192–199, Jan. 2018.

[56] Y. Yang, P. Gao, L. Li, X. Pan, S. Tappertzhofen, S. Choi, R. Waser, I. Valov, and W. D. Lu, "Electrochemical dynamics of nanoscale metallic inclusions in dielectrics," *Nat. Commun.*, vol. 5, p. 4232, Jun. 2014.

[57] M. Ceschia, A. Paccagnella, A. Cester, A. Scarpa, and G. Ghidini, "Radiation induced leakage current and stress induced leakage current in ultra-thin gate oxides," *IEEE Trans. Nucl. Sci.*, vol. 45, no. 6, pp. 2375–2382, Dec. 1998.

[58] M. Ailavajhalaa, Y. Gonzalez-Velo, C. Poweleit, H. Barnaby, M. Kozicki, D. Butt, and M. Mitkova, "New functionality of chalcogenide glasses for radiation sensing of nuclear wastes," *J. of Hazardous Materials*, vol. 269, pp. 68–73, 2014.

[59] S.-y. Miyatani, "Ionic conductivity in silver chalcogenides," *J. Phys. Soc. of Japan*, vol. 50, no. 10, pp. 3415–3418, Oct. 1981.

[60] F. Kirchhoff, J. M. Holender, and M. J. Gillan, "Structure, dynamics and electronic structure of liquid Ag-Se alloys investigated by ab initio simulation," *Phys. Rev. B*, vol. 54, no. 1, p. 14, Feb. 1996.

[61] A. Sahu, D. Braga, O. Waser, M. S. Kang, D. Deng, and D. J. Norris, "Solid-Phase flexibility in Ag2Se semiconductor nanocrystals," *Nano Letters*, vol. 14, no. 1, pp. 115–121, Jan. 2014.

[62] R. Zhang, J. Ren, H. Jain, Y. Liu, Z. Xing, and G. Chen, "In-situ raman spectroscopy study of photoinduced structural changes in Ge-rich chalcogenide films," *J. American Ceramic Soc.*, vol. 97, no. 5, pp. 1421–1424, May 2014.

[63] J. Yu and H. Yun, "Reinvestigation of the low-temperature form of Ag2Se (naumannite) based on single-crystal data," *Acta Crystallographica Section E: Structure*, vol. 67, no. 9, pp. 1–6, 2011.

[64] P. Boolchand and W. J. Bresser, "Mobile silver ions and glass formation in solid electrolytes." *Nature*, vol. 410, no. 6832, pp. 1070–1073, Apr. 2001.

[65] C. Fang, R. de Groot, and G. Wiegers, "Ab initio band structure calculations of the low-temperature phases of Ag2Se, Ag2Te and Ag3AuSe2," *J. of Phys. and Chem. of Solids*, vol. 63, no. 3, pp. 457–464, Mar. 2002.